Cancerous and Non-Cancerous Lung Extracellular Matrix: from a microstructure-mechanical property study to the development of a 3D Platform to unravel Cell-ECM interaction

Dissertation submitted in partial fulfilment of the requirements for the degree of Doctor of Philosophy

Mikel Santiago Behobide

Donostia - San Sebastián, July 2020

ABSTRACT

ABSTRACT

Lung cancer is the leading cause of cancer death among both women and men. It causes more deaths than colon, breast and prostate cancers combined. It is also the second most common cancer in both men and women, about 13% of all new cancers are lung cancer. Approximately 228,150 new cases are expected for the year 2020, which will cause about 142,670 deaths in the United States as the American Cancer Society expects.

The mechanical properties of the Extracellular matrix (ECM) of many tissues, and specifically the lung, have been proven to affect cell and tissue functions. Moreover, it is well known that there is a dynamic reciprocity between cells and ECM mechanics, and this communication is affected during pathologies. However, the mechanisms by which cells stiffen the matrix remain understudied. The aim of this thesis is to characterize the mechanical behavior at local scale of healthy and pathological lung ECM and correlate it to its local microstructure. To achieve this goal, an Atomic Force Microscopy head has been mounted on top of an epifluorescence microscope to measure at the same locations the mechanical properties of the ECM and the microstructure of the three main fibrillar proteins of the lung ECM: collagen I, collagen III and elastin.

Cancerous and non-cancerous lung ECM samples from 7 patients were obtained. The samples were sliced in 7 µm thick samples and the

collagen I, collagen III and elastin were immunostained following a primary/secondary antibody protocol. Then 400 AFM indentations of 500 nm were performed in a 100*100µm area while each protein map was imaged using the epifluorescence microscope. Considering all the patients, the mean value of the effective elastic modulus measured by AFM was of 6.33 ±1.13 kPa for non-cancerous lung ECM and of 15.65±4.04 kPa. Therefore, there is a 2.5 fold increase of stiffness in cancerous lung ECM compared to non-cancerous lung ECM.

For all the samples, the Young's modulus showed a Gaussian stiffness distribution. When all the indentation tests performed for each patient were plotted together, that is tests performed on the cancerous and non-cancerous regions of the same slice, the distribution obtained was a bimodal for all the patients. The first peak of the distribution was related to the non-cancerous ECM and the second peak to the cancerous ECM. The mean values obtained from the peaks of the bimodal distribution overestimated the measured mean of both cancerous and non-cancerous ECM.

Then, the correlation between the composition and the stiffness of the ECM was studied. First, the volume fraction of the fibrillary proteins in the samples was calculated using two different references, one relative to the maximum intensity of all the samples and the other one relative to the maximum intensity of each sample. Both showed an increment of the collagen I between the non-cancerous and cancerous samples with a mean increase of 1.7 folds and 1.5 folds, respectively. A positive correlation between the Collagen I volume fraction and measured stiffness was found for each sample. When the comparison was made

between samples, a higher correlation was found for the second volume fraction, with an R^2=0.60.

Then, a microstructure-mechanical property relationship was studied. For that, a model based on Eshelby´s inclusion problem was used to predict the mechanical behavior of the lung cancerous and non-cancerous ECM. This model can estimate the elastic modulus of a matrix with ellipsoidal inclusions inside, that would resemble the ECM with the Collagen I fibers as the inclusions. Two different fiber distributions were considered.

The first one assumes that the Collagen I fibers are oriented in 3D. Using an elastic modulus for the collagen I of 100 MPa, in the range reported in literature, the values of the elastic modulus of the ECM were overestimated by two orders of magnitude. A new value of the elastic modulus of collagen I fibers was calculated using the model and the measures obtained at the 10 points with the highest volume fraction of collagen I in all the samples. This calculation was done separately for non-cancerous and cancerous samples obtaining an elastic modulus of the collagen I fibers of 390 kPa for non-cancerous samples and of 1050 kPa for cancerous samples, well below the values reported in literature. The model predicted the E of the non-cancerous and cancerous lung ECM with a mean absolute error of 25.08% and 32.74% respectively, and an R^2=0.6155 was obtained when a linear regression was fitted for the predicted versus measured values.

The second approach assumes that Collagen I fibers are oriented in 2D. In this case, the elastic modulus of collagen I fibers is assumed to be of 100 MPa, in the range reported in literature. The elastic modulus of the

matrix was tuned in order to minimize the absolute average error between the measured and predicted elastic modulus of the ECM. This was done separately for the non-cancerous and cancerous samples, mainly because cross-linking was not measured in this work. The best results were obtained for an elastic modulus of the matrix of 0.12 kPa for the cancerous ECM and of 0.05 kPa for the non-cancerous ECM, and calculating the Collagen I volume fraction with the maximum intensity value of each sample as reference. The prediction showed a mean absolute error of 14.48% for the non-cancerous lung ECM and of 11.15% for the cancerous ECM, with a correlation of R^2=0.944 when a linear regression is fitted for the predicted versus measured stiffness.

Finally, a functional platform with tunable stiffness for the study of 3D single cell-ECM interactions based on Methacrylate Hyaluronic Acid hydrogels was developed. First, Hyaluronic Acid Methacrylate was synthesized, which when crosslinked with dithiothreitol gave a range of stiffnesses ranging from 0.2 to 19 kPa. This range comprehends both the mean values of the cancerous and non-cancerous ECM. Then, proof of concept 3D cell migration assays were performed for A549 and H1299 cells inside of three hydrogel with different stiffnesses.

RESUMEN

El cáncer de pulmón es la segunda causa más común de cáncer en mujeres y hombres, alrededor del 13% de todos los nuevos cánceres diagnosticados. Es la causa primaria de muerte por cáncer en mujeres y hombres. Causa más muertes al año que el cáncer de colon, mama y próstata combinados. Alrededor de 228,150 nuevos casos se esperan para el año 2020 que causaran un total de 142,670 muertes en los Estados Unidos tal y como anuncia La Sociedad Americana del Cáncer.

Las propiedades mecánicas de la Matriz Extracelular (ECM) de muchos tejidos, y específicamente del pulmón, han demostrado afectar las funciones tanto celular como a nivel tisular. De hecho, se sabe que existe una reciprocidad dinámica entre las células y la mecánica de la ECM, y esta comunicación se ve afectada durante estados patológicos. El objetivo de esta tesis es caracterizar el comportamiento mecánico a escala local de la ECM de pulmón y correlacionarlo con su microestructura. Para realizar este estudio, se ha montado una cabeza de un Microscopio de Fuerza Atómica (AFM) sobre la base de un Microscopio de epifluorescencia, de tal forma que se pueda obtener información de la microestructura de las principales proteínas fibrilares de la ECM (Colágeno I, Colágeno III y Elastina) y de las propiedades mecánicas de la ECM de forma simultánea en la misma posición.

Se obtuvieron 7 muestras de paciente de cáncer de pulmón, se hicieron cortes de 7 µm, se identificaron regiones cancerosas y no cancerosas en cada muestra, se descelularizaron y se realizaron tinciones de inmunofluorescencia siguiendo un protocolo de anticuerpo primario/secundario para las principales proteínas fibrilares de la ECM:

colágeno I, colágeno III y elastina. Después, se realizaron 400 indentaciones de 500 nm de profundidad en un área de 100 µm *100 µm mientras se obtenían mapas de proteínas de la zona indentada. Considerando las muestras de los 7 pacientes, se midió un módulo elástico efectivo medio para las regiones no cancerosas de la ECM de pulmón de 6.33 ±1.13 kPa, mientras que el módulo elástico medio en las regiones cancerosas fue de 15.65±4.04 kPa. Es decir, la rigidez es 2,5 veces superior en las zonas cancerosas.

Para todas las muestras, el modulo de Young mostró una distribución Gaussiana de rigideces. Cuando todos los ensayos de indentación fueron graficados de forma conjunta para una misma muestra, se obtuvo una distribución bimodal para todos los pacientes. El primer pico de la distribución correspondía a la ECM no cancerosa y el segundo pico de la distribución a la ECM cancerosa. Los valores medios obtenidos de la distribución bimodal sobreestimaban los valores medios medidos de la ECM cancerosa y no cancerosa.

Después se calculó la correlación entre las medidas de fracción volumétrica de proteína obtenidas en las muestras y el módulo elástico medido. La fracción volumétrica se calculó de dos maneras, una de ellas relativa a la intensidad máxima de todas las muestras y la otra relativa a la intensidad máxima de cada muestra. Ambas mostraron un incremento en la fracción volumétrica del colágeno I de 1.7 y .1.5 veces mayor respectivamente para la ECM cancerosa frente a la no cancerosa. Ambas mostraron una correlación positiva entre la fracción volumétrica obtenida y el módulo elástico medido para todos los puntos de cada muestra. Entre muestras, la segunda mostró una correlación entre la

fracción volumétrica media y el módulo elástico medio de cada muestra con R^2=0.60.

Se implementó el modelo de Eshelby para predecir el comportamiento mecánico de la matriz extracelular del pulmón canceroso y sano. El modelo puede estimar el módulo elástico de una matriz con inclusiones elipsoidales, que representarían a las fibras de colágeno dentro de la ECM. Se consideraron dos posibles distribuciones para la orientación de las fibras.

La primera asume que las fibras de colágeno I están orientadas en 3D. Utilizando un módulo elástico para el colágeno I de 100 MPa, dentro del rango reportado en literatura, los valores del módulo elástico de la ECM se sobreestimaban por dos ordenes de magnitud. Se calculó un nuevo valor del módulo elástico de las fibras de colágeno I utilizando el modelo y las medidas obtenidas de los 10 puntos con mayor fracción volumétrica de colágeno I en todas las muestras. Este cálculo se hizo de manera separada para las muestras no cancerosas y cancerosas obteniendo un módulo elástico para las fibras de colágeno I de 390 kPa para las muestras no cancerosas y 1050 kPa para las muestras cancerosas, muy por debajo de los valores reportados en literatura. El modelo fue capaz de predecir el módulo elástico de la ECM no cancerosa y cancerosa con un error medio del 25.08% y 32.74% respectivamente con un ajuste a una regresión lineal de R^2=0.6155 frente a los valores medidos en AFM.

La segunda aproximación supone que las fibras de colágeno I están orientadas en el plano 2D. En este caso, se asume que el módulo elástico de las fibras de colágeno es de 100 Mapa, dentro del rango reportado en literatura. El módulo elástico de la matriz fue ajustado para minimizar el

error absoluto entre el valor medido y el módulo elástico predicho de la ECM. Esto se hizo de manera separada para las muestras cancerosas y no cancerosas, sobre todo por que el efecto del crosslinking no se midió en este trabajo. Los mejores resultados se obtuvieron para E_{matrix} = 0.12 kPa para las muestras cancerosas y E_{matrix} = 0.05 kPa para las no cancerosas y calculando la fracción volumétrica del colágeno I usando como referencia el máximo de intensidad medido en cada muestra.

La segunda aproximación del modelo suponía las fibras de colágeno I orientadas en el plano 2D, lo cual permitía el uso de valores encontrados en bibliografía para la rigidez de las fibras de colágeno I. Hubo que ajustar los valores de la matriz del modelo para la ECM cancerosa y no cancerosa, de tal forma que reflejaran el efecto del cross-linking y por tanto el incremento en la rigidez. Los mejores resultados se obtuvieron para Ematrix = 0.12 kPa para las muestras cancerosas y E_{matrix} = 0.05 kPa para las no cancerosas. El modelo fue capaz de predecir el módulo elástico de la ECM con un error de 14.48% para las muestras no cancerosas y un error de 11.15% para las muestras cancerosas con un ajuste a una regresión lineal de R^2=0.94 frente a los valores medidos en AFM.

Finalmente, se desarrolló una plataforma para el estudio de las interacciones célula-ECM en tres dimensiones basada en hidrogeles de Ácido Hialurónico. Se sintetizó Ácido hialurónico con grupos metacrilato que permitían el crosslinking mediante dithiothreithiol, esto permitía a los hidrogeles alcanzar rigideces en un rango entre 0,2 y 19 kPa, rango que incluye las medias de los módulos de Young efectivos de la matriz cancerosa y no cancerosa. Resumidamente, la gelificación de los

hidrogeles se realizaba con las células embebidas en ellos mediante el uso de un motor rotatorio que mantenía las células suspendidas en el espacio tridimensional en todo momento, a 37°C dentro de una incubadora. El protocolo no sólo permitía una distribución homogénea de las células en los hidrogeles, sino que además permite evitar los efectos de durotaxis que puedan ser provocados por la plataforma. Se realizaron ensayos de migración en 3D dentro de la plataforma para las líneas celulares A549 y H1299 a diferentes niveles de rigidez, las cuales mostraron para la línea H1299 una mayor capacidad invasiva y migratoria.

Contents

1 INTRODUCTION AND OBJECTIVE

Since the beginning of tissue engineering 'stiffness' was already mentioned in the literature [1]. The evolution of tissue engineering started from a simple premise which said: a tissue substitute must be biomechanically able to fulfil the functions of the tissue it replaces, thus, have similar mechanics of those of the native tissue. However, this premise evolved with the understanding that the stiffness of these materials could be felt by cells, and cells would act in response [2].

The extracellular matrix (ECM) was first considered as a structural element for tissues. Starting from the finding on 1966 that the interstitial collagen promotes the conversion of myoblasts to myotubes [3] up to the moment where Bissell et al. made a major contribution proposing the model of dynamic reciprocity [4]. In this approach, the molecules in the ECM interact with receptors on the surface of the cells, these receptors then transmit signals across the cell membrane to molecules in the cytoplasm. This triggers a cascade of events, which will end bringing the information obtained to the nucleus. Finally, this information will generate a specific gene transcription, whose expression will, in turn, affect the ECM.

Now we know that the ECM is not just the non-cellular component of the tissue that provides biochemical and structural support for its cellular constituents. It is also a physiologically active component of the living tissue, responsible for cell-cell communication, cell adhesion and cell

proliferation [5]. For different tissues, the components of the ECM are secreted, arranged, degraded and modified by nearby cells in accordance with the needs of the tissue and constantly undergoing a remodeling process [6]. The balance between degradation and secretion of ECM, is responsible for mechanical homeostasis and the properties of each organ, such as elasticity and compressive or tensile strength.

A human organism comprises tissues that cover a remarkable window of stiffnesses; from the 11 Pa of the intestinal mucus [7] to the 20 GPa of cortical bone [8], ranging in between tissues such as fat (0.02 kPa) , brain (0.2-1 kPa) or liver (0.64kPa), to stiffer tissues such as cardiac muscle (20-150 kPa), articular cartilage (950 kPa)[9] or compact bone (11,5 GPa)[10].

Since cells can feel and respond to external stimuli happening in the order of magnitude of few µm or nm [11], it is interesting to study the microstructure of their surrounding ECM on that scale length. When the mechanics of a tissue are measured, the length of the scale must be considered due to the heterogeneity of biological tissues [12]. In contrast with classic macroscopic tensile or compression measurements, Atomic Force Microscopy (AFM) nanoindentation give the chance to study the local mechanical properties of the tissue. The volume tested, and hence the scale length of the measure, will depend on the geometry of the tip used and can go from tens of nanometers to tens of microns.

It has been previously proved that the cancerous tissue is stiffer than its non-cancerous counterpart [13]–[16]. It also has been observed that a combined increase in collagen deposition and crosslinking increases ECM stiffness [17]. Thus, changes in the ECM microstructure lead to

changes in the ECM stiffness. However, few papers show how microstructure explains mechanical behavior. The aim of this thesis is to study microstructure-mechanical property relation in human lung ECM and how this relation is altered in cancer

For this aim, an Atomic Force Microscopy head on top of an epifluorescence microscope was used to obtain in situ the mechanical properties and microstructure of the same ECM spot. Both samples of cancerous and non-cancerous lung ECM from 7 patients were decellularized and stained for the three main fibrillar proteins in lung (Collagen I, Collagen III and Elastin)..

The next couple of chapters will show an overview of the context in which this thesis is created. First the overall composition of the ECM was reviewed and, in particular, the composition of the lung ECM. Also, the changes that the ECM suffers in lung disease. and how the ECM affects the hallmarks of cancer is reviewed in a separate chapter.

In chapter 4, the elastic modulus and local composition of the cancerous and non-cancerous lung ECM will be compared. Also both of them will be correlated to observe if there is any correlation between the grade of deposition of the different ECM components (collagen I, Collagen III and elastin) and the changes measured in the ECM stiffness.

Chapter 5 presents two different approaches based on Eshelby's inclusions model to try to predict the mechanical behavior of the cancerous and non-cancerous lung ECM using as inputs the data obtained from the immunofluorescence images of chapter 4. The ECM is treated as a composite material with a matrix in which collagen I fibers are embedded as inclusions.

Finally, in chapter 6, a platform based on Hyaluronic Acid hydrogels with tunable stiffness is developed to study cell-ECM interactions in a 3D environment. The idea is to obtain a scaffold that can mimic the lung ECM stiffness and study different cell behaviors such as motility or viability.

These three chapters include an introduction and a discussion of the results and conclusions for each one of them. Finally, the conclusions for this whole research are presented.

BIBLIOGRAPHY

[1] R. Langer and J. P. Vacanti, "Tissue Engineering," *Science (80-.).*, vol. 260, no. 1, pp. 920–926, 1993.

[2] D. E. Discher, P. Janmey, and Y. L. Wang, "Tissue cells feel and respond to the stiffness of their substrate," *Science (80-.).*, vol. 310, no. 5751, pp. 1139–1143, 2005.

[3] S. D. Hauschka and I. R. Konigsberg, "The influence of collagen on the development of muscle clones.," *Proc. Natl. Acad. Sci. U. S. A.*, vol. 55, no. 1, pp. 119–126, 1966.

[4] M. J. Bissell, H. G. Hall, and G. Parry, "How does the extracellular matrix direct gene expression?," *J. Theor. Biol.*, vol. 99, no. 1, pp. 31–68, 1982.

[5] C. Frantz, K. M. Stewart, and V. M. Weaver, "The extracellular matrix at a glance," *J. Cell Sci.*, vol. 123, no. 24, pp. 4195–4200, 2010.

[6] P. Lu, K. Takai, V. M. Weaver, and Z. Werb, "Extracellular Matrix degradation and remodeling in development and disease," *Cold Spring Harb. Perspect. Biol.*, vol. 3, no. 12, pp. 1–24, 2011.

[7] J. Sotres, S. Jankovskaja, K. Wannerberger, and T. Arnebrant, "Ex-Vivo Force Spectroscopy of Intestinal Mucosa Reveals the Mechanical Properties of Mucus Blankets," *Sci. Rep.*, vol. 7, no. 1, pp. 1–14, 2017.

[8] J. Y. Rho, R. B. Ashman, and C. H. Turner, "Young's modulus of trabecular and cortical bone material: Ultrasonic and microtensile measurements," *J. Biomech.*, vol. 26, no. 2, pp. 111–119, 1993.

[9] I. Levental, P. C. Georges, and P. A. Janmey, "Soft biological materials and their impact on cell function," *Soft Matter*, vol. 3, no. 3, pp. 299–306, 2007.

[10] H. Follet, G. Boivin, C. Rumelhart, and P. J. Meunier, "The degree of mineralization is a determinant of bone strength: A study on human calcanei," *Bone*, vol. 34, no. 5, pp. 783–789, 2004.

[11] S. Sen, A. J. Engler, and D. E. Discher, "Matrix strains induced by cells: Computing how far cells can feel," *Cell. Mol. Bioeng.*, vol. 2, no. 1, pp. 39–48, 2009.

[12] C. T. McKee, J. A. Last, P. Russell, and C. J. Murphy, "Indentation versus tensile measurements of young's modulus for soft biological tissues," *Tissue Eng. - Part B Rev.*, vol. 17, no. 3, pp. 155–164, 2011.

[13] J. M. Chang *et al.*, "Clinical application of shear wave elastography (SWE) in the diagnosis of benign and malignant breast diseases," *Breast Cancer Res. Treat.*, vol. 129, no. 1, pp. 89–97, 2011.

[14] J. H. Youk, E. J. Son, H. M. Gweon, H. Kim, Y. J. Park, and J. A. Kim, "Comparison of strain and shear wave elastography for the differentiation of benign from malignant breast lesions, combined with b-mode ultrasonography: Qualitative and quantitative assessments," *Ultrasound Med. Biol.*, vol. 40, no. 10, pp. 2336–2344, 2014.

[15] M. Plodinec *et al.*, "The nanomechanical signature of breast cancer," vol. 7, no. October, 2012.

[16] M. Lekka *et al.*, "Cancer cell detection in tissue sections using AFM," *Arch. Biochem. Biophys.*, vol. 518, no. 2, pp. 151–156, 2012.

[17] T. R. Cox *et al.*, "LOX-mediated collagen crosslinking is responsible for fibrosis-enhanced metastasis," *Cancer Res.*, vol. 73, no. 6, pp. 1721–1732, 2013.

[18] rican Cancer Society, "American Cancer Society. Cancer Treatment & Survivorship Facts & Figures 2019-2021. Atlanta, Ga: American Cancer Society; 2019."

2 THE EXTRACELLULAR MATRIX (ECM)

2.1 WHAT IS THE ECM?

The ExtraCellular Matrix (ECM) is a structural scaffold that directs cell adhesion and migration, as well as regulating cellular growth, metabolism and differentiation signals [1]. It is a dynamic three-dimensional structure that anchors and surrounds cellular compartments in tissues and organs.

A model of 'dynamic reciprocity' was proposed by Bissell in 1982 [2], in which ECM molecules and receptors on the surface of cells interact and then, transmit signals across the cell membrane to molecules in the cytoplasm. These signals initiate a cascade of events through the cytoskeleton until they reach the nucleus, resulting in the expression of specific genes, whose products affect the ECM in various ways. It is clear now that cell-ECM interactions, biochemically or biomechanically, can directly regulate aspects like: cell adhesion[3], migration[4], growth[5], differentiation[6] and apoptosis[7]. Also, modulate the activities of cytokines and growth factors, and directly or indirectly activate intracellular signaling.

There are four principal structural components of the extracellular matrix: collagens, elastin, glycoproteins, and proteoglycans. Collagens and elastin form insoluble structures that resist tensile forces and

confer elastic properties to tissues, respectively. Within these structures, embedded, we can find proteoglycans and glycosaminoglycans that hydrate the matrix and regulate the diffusion of nutrients, metabolites and hormones. Glycoproteins such as fibronectin and laminins provide connections between cells and the ECM as they interact with other structures, growth factors, cytokines and other cell surface receptors[8].

The cell-ECM interaction is reciprocal and a key modulator of developmental patterning and tissue homeostasis. Cells secrete and control the temporal and hierarchical assembly of ECM proteins into supramolecular assemblies. In turn, the four ECM components mentioned before and water determine the porosity, topology and stiffness of tissues, which can range from stiff mineralized tissue of the bone to a transparent soft gel that forms the vitreous body of the eye[9].

2.2 PROTEINS OF THE ECM

There are over 300 proteins that bioinformaticians define as the "core matrisome". Composed by different ECM proteins, such as collagens, glycoproteins and proteoglycans. These proteins are synthesized by different mesenchymal cells (fibroblasts, osteoblasts, chondroblasts…)[10].

2.2.1 Collagens

Collagens are the most important structural component of the connective tissue and the most abundant protein family in animals: they form the 30% of the total protein mass [11]. The structure of the collagen

(COL) is a repetition of three amino acids, generally Glycine–Proline–Hydroxyproline (GPP). Collagen is composed by a triple helix of α-chains. Depending on the repeat length and integrity of the GPP, collagens may contain substantial amounts of uninterrupted triple helix, which is common in fibrillar collagens. These constituent polypeptide chains are called α-chains. Alternatively, α-chains may contain a variable number of non-collagenous domains that introduce helical interruptions. Collagens self-assemble into structurally and functionally diverse assemblies such as parallel bundles of fibrils in the tendon, orthogonal lattices in the cornea, and a concentric interlocking weave in bone and skin.

All these different structures provide tissues with tensile strength and a scaffold that protects them from mechanical stress [12]. Collagens and cells can mediate cell adhesion and motility during tissue morphogenesis, growth, and wound healing[13]. There are up to 28 collagen types, which are numbered (I-XXVIII), based on their order of discovery. The collagen family is divided into different subfamilies based on structural homology between the collagens and the type of structures they form Table 1

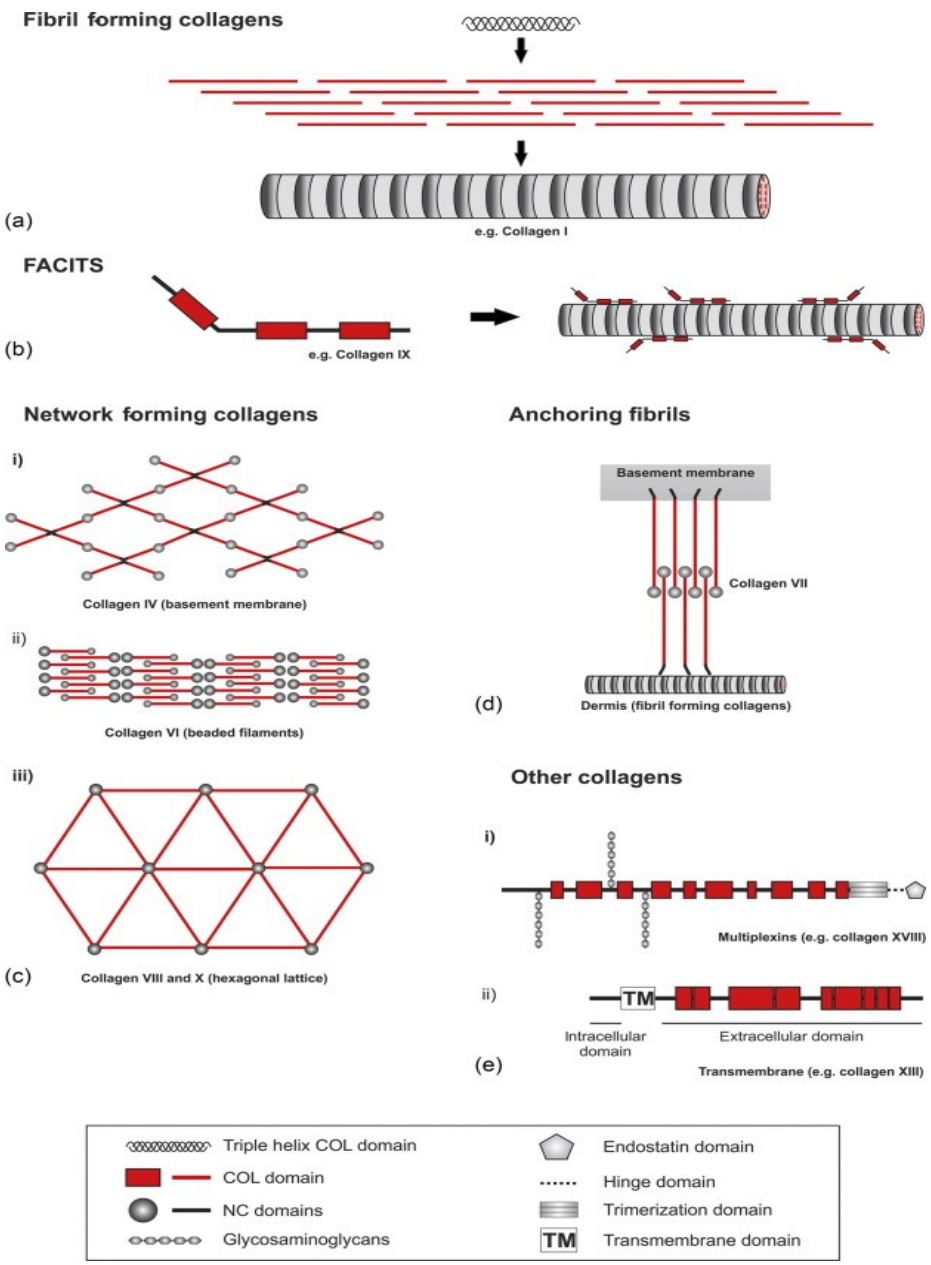

Figure 2.1 The collagen superfamily. [8] (a) Fibril-forming collagens. (b) FACITs consist of tandem repeats of COL domains (red box) interrupted by NC domains (black line). (c) Network-forming collagens. (i) Collagen type IV , (ii) Collagen type VI , (iii) collagens type VIII and X ,hexagonal lattices. (d) Anchoring fibrils. (e) Other collagens, (i) Multiplexins (ii) Transmembrane collagens

2.2.1.1 *Fibril forming collagens*

These types of collagens are characterized by a long uninterrupted COL domain, which is flanked by small globular (non-collagen) NC domains (Figure 2.1 a). Collagen types, I, II, III, V, XI, XXIV, and XXVII belong to this collagen family. Collagens I, II and III are the most abundant proteins and are the major components of the fibrillary collagen assemblies[11]. Fibril-forming collagens are made of heterotypic fibers, and the gene dosage of major and minor fibril collagens types dictates the composition and thus the biomechanical properties of the matrix. Skin dermis, cornea, tendons, blood vessels, bone are non-cartilaginous connective tissues composed of heterotypic fibrils containing collagen I, II and V[14].

2.2.1.2 *Fibril-Associated Collagens (FACITs)*

This collagen family includes type IX, XII, XIV, and XX, and is characterized by a tandem repeat of short COL domains interrupted by NC domains; they modulate the surface properties of the fibrillar collagens by adding in the interfibrillar space in staggered fibrils (Figure 2.1 b).

2.2.1.3 *Network forming collagens*

Collagen type IV, VI, VIII, and X are classified as network- forming collagens and can be found in basement membranes (Figure 2.1 c).

2.2.1.4 *Anchoring fibrils*

Anchoring fibrils are mostly composed of collagen VII, which connects and stabilizes the basement membrane to the dermis[15] by interacting

with collagen type IV networks in the basement membrane, and collagen fibrils in the underlying dermis (Figure 2.1 d).

2.2.2 Glycoproteins

There are around 200 different proteins known as glycoproteins in the vertebrates ECM. They are modular proteins that are involved in the interactions with other ECM proteins and growth factors, which help with the structural and functional properties of the ECM. The formation of the ECM network is a cell-dependent process that needs integrins and non-integrin cell surface receptors.

2.2.2.1 *Integrins*

Integrins are transmembrane heterodimeric receptors that mediate cell adhesion and motility. The extracellular domains of integrins bind to plenty of ECM proteins, while the part that belongs to the cytoplasm, drives cytoskeletal rearrangements and anchors intracellular signaling molecules. 24 functional proteins have been found; many recognize the tripeptide sequence arginine-glycine-aspartic acid (RGD) on certain collagens and many glycoproteins [16].

2.2.2.2 *Fibronectin*

It is a well-known cell adhesion protein as a master organizer of the matrix because the deposition and assembly of most of its proteins is dependent of a pre-assembled network of fibronectin[12]. The interaction between fibronectin and cell surface receptors such as integrins and syndecans promotes cell adhesion, changes in cell-shape, migration, and differentiation.

2.2.3 Elastin

The main function of the elastic fibers is to provide elastic properties to tissues and organs, which are subjected to tension and relaxation through their life. The ability of blood vessels, lung, and skin to expand is mainly due to the biophysical properties of elastin. Elastin is an insoluble core composed of amorphous elastin (~90%) surrounded by a mantle of fibrilin containing microfibrils, which compose these type of elastic fibers[17]. Desmosine and isodesmosine are elastin-specific mature crosslinks. The crosslinking renders elastin insoluble and endows elastic fibers with the ability to withstand repeated distension and recoil. The microfibrils contained in the fibrillin provide a scaffold for the deposition, alignment, and crosslinking of tropoelastin [18].

2.2.4 Proteoglycans and glycosaminoglycans

Proteoglycans are composed of a core made of a modular protein which is covalently linked to one or more glycosaminoglycan (GAG) chains[19]. Proteoglycans and their GAG chains compose the “base” of the ECM and are distributed through the interstices of the crosslinked fibrillar assemblies, but also present in the ECM surface. They not only actuate filling the gaps between fibers but also mediate cell-matrix interactions and organize the matrix by binding to other matrix components. The GAG chains are osmotically active components and can absorb water to hydrate the extracellular environment, due to this property they provide lubrication and give shock-absorbing ability to organs.

2.2.4.1 *Glycosaminoglycans*

GAGs are unbranched, hydrophilic, highly charged chains constituted by repetitions of disaccharide units, where one of the sugars is a hexosamine and the other can be uronic acid or a hexose. There are six groups of GAGs: chondroitin sulfate, dermatan sulfate, heparan sulfate, keratan sulfate, heparin, and hyaluronan or hyaluronic acid (HA). The difference between these groups resides on their disaccharide composition, linkage between the disaccharides, uronate epimerization and sulfation patterns. The combination of these factors provide GAGs with unique structural and functional properties that change with pathological conditions and over the course of life. All the GAG are covalently bound to the core protein except for the heparin and HA. HA is also an exception in a way that is unsulfated and its synthesis happens on the cell surface [20].

2.2.4.2 *Proteoglycans*

There are over 30 proteoglycans expressed in vertebrates which are divided in three different categories: (1) cell surface proteoglycans, (2) modular proteoglycans and (3) small leucine rich proteoglycans (SLRPs)[21]. The functional complexity of proteoglycans is dictated by: (1) the length of the glycosaminoglycan chain, (2) the number of GAG attached to the core and (3) the nature of the core protein, which can exist without any GAG attachment[22].

Table 1 Overview of collagen families

Class	Type	Localization
Fibril-forming collagens	I	Non-cartilaginous tissue
	II	Cartilage, vitreous humour of the eye, nucleus pulposus
	III	Embryonic expression, soft tissue, co-assemblies with collagen type I fibrils
	V	Co-assemblies with collagen type I fibrils
	XI	Co-assemblies with collagen type II fibrils
	XXIV	Cornea, developing bone
	XXVII	Cartilage, epithelial cells
FACITS	IX	Co-assemblies with collagen type II fibrils
	XII	Collagen type I fibrils
	XIV	Collagen type I fibrils
	XVI	Collagen and fibrillin fibrils
	XIX	Ubiquitous expression during development
	XX	Corneal epithelium
	XXIV	Widespread tissue distribution
	XXII	Tissue junctions
Network-forming collagens	IV	Ubiquitous component of basement membranes
	VI	Widespread tissue distribution
	VIII	Basement membranes
	X	Hypertrophic cartilage
	XXVIII	Basement membranes in peripheral nervous system
Anchoring fibrils	VIII	Anchoring fibrils
Transmembrane collagens	XIII	Skin, neuromuscular junctions
	XVII	Dermal-epidermal junction
	XXIII	Corneal epithelium, endothelial cells
	XXV	neuronal tissue
Multiplexins	XV	Basement membranes
	XVIII	Basement membranes

2.3 LUNG ECM

The lung ECM is unique as it provides structural support for the cells but also regulates the developmental organogenesis, homeostasis and injury-repair responses. In the lung development, there are two main concepts regarding ECM: (1) Lung ECM is not just a physical support for resident lung cells and contributes to its mechanical properties but, also, is essential for biophysical and biochemical signaling of lung cells. (2) Reciprocally, lung cells are the ones to regulate the production and deposition of ECM over the course of lung development[23]. The processes by which lung cells produce or break down ECM and, at the same time, are regulated by the ECM are crucial to normal lung development. Alterations on these processes may lead to abnormalities or disorders such as lung cancer, with its corresponding alterations in the ECM[24].

The composition of lung ECM changes over the course of lung development and can be very heterogeneous depending on its location and the developmental stage of the individual. For example, the lung ECM in fetal, neonatal and adult tissues is different, and temporally regulates the fate, migration, and differentiation of the resident cells[25].

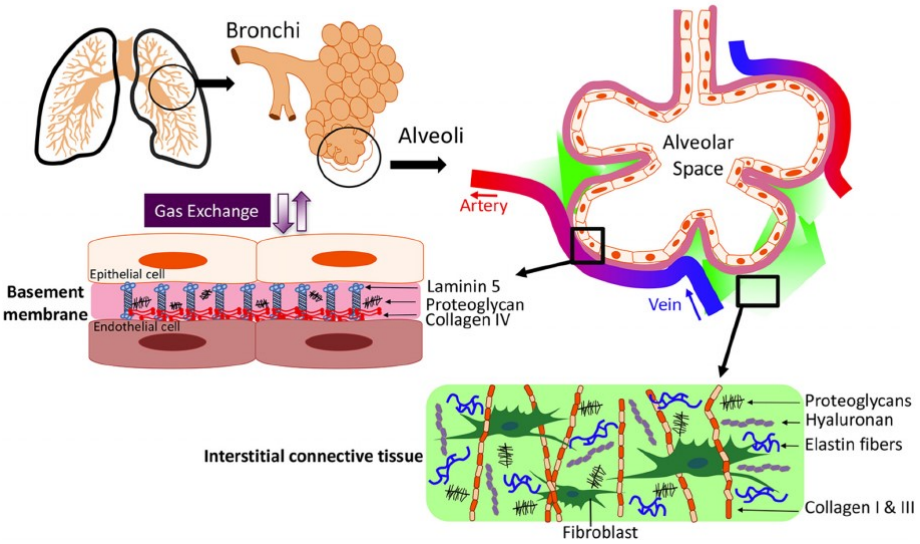

Figure 2.2 Schematic view of the lung structure, from bronchiole and bronchi branching to the differences in composition of the basement *membrane and the interstitial connective tissue. The basement membrane is rich in Laminin, proteoglycans and collagen IV and the interstitial connective tissue in the alveoli, rich in Hyaluronan, elastin fibers and collagen I and III* [26]

Table 2 Main structural components of the lung ECM.

Type	Name
Structural Proteins	Collagen Elastin
Adhesion Proteins	Fibronectin Fibrillin Laminin Tenascin Vitronectin Osteonectin
Glycosaminoglycans and proteoglycans PG= Protein core + Glycosaminoglycan	Agrican Versican Neurocan Heparan ✚ Heparan sulphate Kondroitin 4-sulphate Kondroitin 6-sulphate Deparan sulphate Hyaluronan

2.3.1 Structural proteins on the lung ECM

Most of the structural proteins that make up the lung ECM are collagens and elastin. The elastic modulus of collagen fibers is greater than the elastic modulus of elastin fibers, 100-360MPa[27] and 1.1 MPa[28] respectively according to bibliography. Collagen and elastin fibrils intertwine in order to create a functional extracellular network in the lung that is able to withstand the force of the passive response during breathing. Shortness of breath can be caused by an increased proportion

of collagen relative to elastin, changing the mechanical properties of the tissue such as elasticity, during pulmonary fibrosis [29].

2.3.1.1 *Collagen in lung*

Multiple isoforms of collagen add structural stability and tensile strength in lung tissue [30]. The triple helical structure of collagens I and III form a tight fibrous network through the conducting airways, bronchi, and bronchioles, providing strength and stability to the proper function of the tissue[31], [32]. Non-fibrillar collagens such as IV and V can be found in the lung basement membrane. These type of collagens are essential molecular scaffolds for physiological processes such as fibroblast proliferation, migration and adhesion [33].

2.3.1.2 *Elastin in lung*

Elastin fibers, one of the most critical components of lung ECM are in charge of controlling the respiratory compliance since they have the ability to stretch up to 140% in contrast to collagen, which provides more tensile strength but can just stretch by 2% [34]. Lung elastin fibers are composed 90% from the elastin precursor, tropoelastin. The rest 10% of the elastin is composed by microfibril proteins, such as fibulin, fibrilin and microfibrin-associated glycoprotein [35]. After assembly, elastin fibers become highly insoluble due to the multiple highly repetitive hydrophilic lysine rich domains as well as hydrophobic aminoacids that can be found in tropoelastin, the soluble precursor of the elastin that is crosslinked by the lysyl oxisidase enzyme. These domains confer elastin's elasticity[36] .

2.3.1.3 *Adhesion proteins in the lung ECM*

Adhesion proteins are involved in cellular adhesion to the ECM. Fibronectin, laminin, firbrilin, tenascin, vitronectin or osteonectin belong to this protein family. Fibronectin is an adhesion protein which contains binding sites for the attachment of other molecules and bonds to collagen fibrils in the ECM[37]. Fibronectins are known for their contribution to cell adhesion, growth, differentiation and migration [38]. Laminin, which binds to cell surface receptors and other ECM components, is critical to tissue structure and cell function[39].

2.3.1.4 *Glycosaminoglycans and proteoglycans in the lung ECM*

The anionic and non-sulfated glycosaminoglycan hyaluronic acid (HA) plays an essential role on the lung extracellular matrix. HA is a high molecular weight polysaccharide, which consists of repeated disaccharide units, and is distinguished from the other GAGs due to its unsulfated nature. CD44 and RHAMM (Receptor for Hyaluronan-mediated motility) are the most common cell-surface receptors for HA. HA receptors are part of cellular signal transduction and contribute to cell proliferation and cell migration. They have been associated with metastasis[40], [41] and have been implicated in the progression of certain malignancies[42]. Significant amounts of HA have been found in lung, kidney, brain and muscle tissue and are reported in [43].

2.4 ECM IN LUNG DISEASE

2.4.1 Importance of understanding the contribution of the ECM in lung disease

The lungs drive two essential physiological functions: passive gas exchange through alveolar respiration and lung-specific immune defense against pathogenic organisms that protect the airway epithelial barrier. Lung ECM is often altered due to a variety of environmental microorganisms that can potentially damage the airway epithelia, such as chronic exposure to inhaled antigens, smoking, air pollution, different pathogens, and trauma [44]. Injured cells can promote specific ECM remodeling that affects their local cellular function, consequently cells close to the proximal conducting airway start to secret more collagens, laminins and proteoglycans [45].

The major components of the ECM are collagens and elastin molecules, which constitute the 60% [46] and 24% [47] of the dry lung weight, respectively. Dysregulation of these proteins in the ECM can lead to a multiple pathological lung conditions.

Many chronic lung diseases are associated with changes in the composition, content and structural disposition of the ECM components. Changes in the ECM, which are driven by multiple cell types in the lung, can affect lung function and cell biology, and overall, a dysregulation of the ECM seems to provide a positive feedback loop to drive the progression of fibrosis.

2.4.2 Homeostasis in lung extracellular matrix

Composition, architecture and mechanical properties of the lung ECM are not uniform across the whole tissue, but they are adapted to the biomechanical and physiological necessities that the matrix must serve within physiological compartments. For example, the alveolar compartment, includes bands of collagen and elastin in the alveolar ducts [48] which are likely to bear stresses and maintain the structural stability [49] but the alveolar walls in order to support efficient gas exchange, exhibit shared basement membranes showing the need of endothelial and epithelial barriers close to them [50]. The conducting airways[44] and vessels of the lung show more pronounced fibrous ECM structures of collagen and elastin in an organized disposition, in particular the vascular structures, which wall composition changes depending on the position in the vascular tree due to changes in pressure during the cardiac cycle [51]. A schematic view of these structures can be seen in Figure 2.2.

These differences in ECM architecture provoke a variation in mechanical properties across the whole tissue of the lung. The airways and vessels as the stiffest zones showing the highest elastic moduli, 23.1 ± 14 kPa for the airways [52], followed by the pleura, 15.76 ± 13.70 kPa [53], and being the alveolar parenchyma the most compliant one, 5.59 ± 3.39 kPa [53].

Lungs with pulmonary fibrosis suffer changes in its mechanics, specifically, highly heterogeneous increases in the Young modulus of the ECM. A median of ~1.6 kPa is found in normal lungs, against a median of ~16kPa in fibrotic tissues, with localized increases up to 50 or 100 kPa [54].

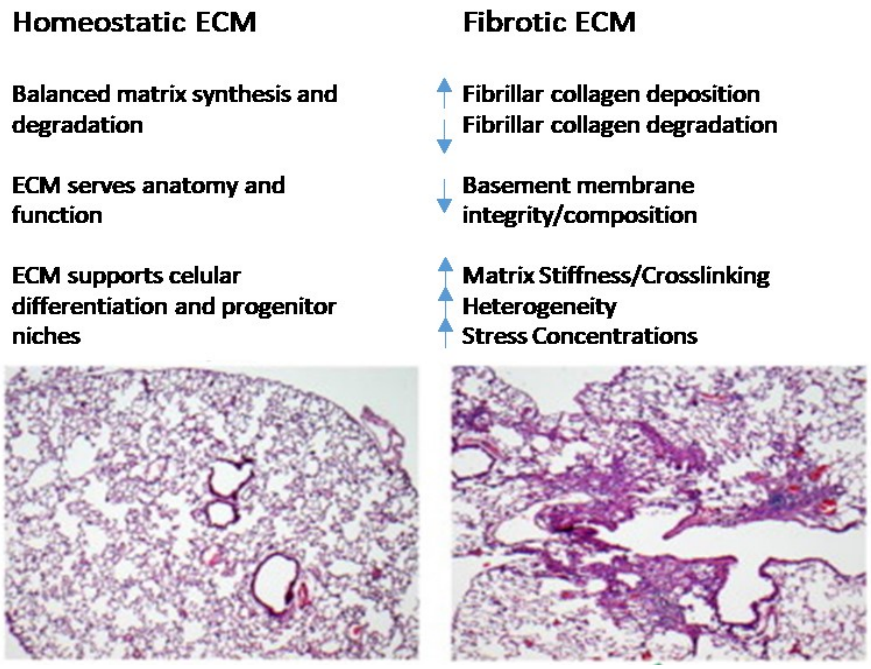

Figure 2.3 Structural components in Homestatic ECM and fibrotic ECM [55]

2.4.3 Asthma

Asthma is an allergic airway disease that is defined by the presence of intermittent airway obstruction that narrows the bronchi and manifests as wheezing and dyspnea [56]. The main structural alteration that can be seen in asthma disease against the healthy lung tissue is the thickening of the airway basement membrane[57]. The subepithelial lamina reticularis that lies beneath the basal lamina of the bronchial epithelium thickens involving the accumulation of collagens I, III, IV and fibronectin[58]. The thickness of this lamina can change from 5-6 μm in healthy lung to up to 9μm in the asthmatic lung [59]. In severe asthma,

there is an increased deposition of collagen I and II and an increased mass on the airway smooth muscle[60].

2.4.4 Idiopathic pulmonary fibrosis

One of the major characteristics of IPF is the massive deposition of heterogeneously distributed ECM components, mainly in the alveolar regions, but it can also be found on the terminal airways. One of the features of the scar-like lesions found in the lungs of patients with pulmonary fibrosis is collagen deposition [61]. These alterations can lead to lower the volumes on spirometry, causing a reduction on the gas transferred[62]. This type of fibrosis is characterized by the increase of the number of myofibroblasts that overproduce collagen I which expands the fibrotic foci in the lungs [63]. Immunohistochemical studies in the early 80s described depositions of type I and III collagens and fibronectin along alveolar septa in chronic fibrotic diseases, being collagen III the one that predominates at early stages of the disease and collagen I at late-stage disease. The content of elastic fibers was also found to increase in fibrotic areas in IPF patients. EFs are key to provide physiological elastic recoil in the lungs, but an excess of elastic fibers can affect the stiffness of the lung tissue and, as a consequence, becoming harder to inhale for the patients [64].

2.4.5 Chronic obstructive pulmonary disease

The apparition of elastolytic enzymes and its consequent destruction of the elastic fibers and the development of emphysema was the central cue in the pathogenesis of COPD [35]. Abnormal elastogenesis, finely

disrupted fibers make an abnormal ECM structure in the COPD [65]. This abnormal distribution of the elastic fibers ends in an elastic reduction, which causes the lung tissue to collapse, that affects the lung parenchyma, but also can be found in the small and large airways of COPD patients [66].

As can be seen, the lung ECM structural proteins such as collagen I and III and elastin are key for maintaining the optimal mechanical properties such as stiffness in the lung. A stiffer lung ECM could cause a difficulty of breath inhaling as happens in asthma disease and a soft ECM could cause a collapse of the tissue blocking the lung airways.

2.4.6 How ECM affects cellular behavior

The ECM has the ability to regulate many cell behaviors that have a great impact on lung pathologies, such as migration or proliferation.

A huge amount of ECM proteins, such as collagen I or fibronectin have been reported to be able to influence cell proliferation. In fact, these two promote adult stem cell proliferation [67]. The ECM synthesized by cells from asthma patients showed that induced a greater proliferative capacity on smooth muscle cells. The ECM synthesized by cells from non-sick patients proliferative capacity was lower[68].

Cell migration is vastly dependent on the tissue environment and the interaction between the mechanical and chemical properties of this environment. Cell migration is influenced in a complex way by the confinement and disposition of the cells in the tissue, the density of adhesion ligands such as the integrins binding to collagens or other ECM proteins and the stiffness and topology of the matrix [69], [70]. The

migration of fibroblasts in damaged lung is commonly influenced by changes in the tissue ECM. Fibroblasts from the broncheo-alveolar lavage fluid of asthmatics seem to migrate twice as far as fibroblast form bronchial biopsies from the same patients, which had an increased production of migration relative proteins. These type of fibroblasts are not to be found in healthy controls [71].

2.5 BIBLIOGRPAHY

[1] T. Scott-Burden, "Extracellular Matrix: The Cellular Environment," *Physiology*, vol. 9, no. 3, pp. 110–115, Jun. 1994.

[2] M. J. Bissell, H. G. Hall, and G. Parry, "How does the extracellular matrix direct gene expression?," *J. Theor. Biol.*, vol. 99, no. 1, pp. 31–68, 1982.

[3] S. Schmidt and P. Friedl, "Interstitial cell migration: Integrin-dependent and alternative adhesion mechanisms," *Cell Tissue Res.*, vol. 339, no. 1, pp. 83–92, 2010.

[4] Y. Choi, H. Chung, H. Jung, J. R. Couchman, and E. S. Oh, "Syndecans as cell surface receptors: Unique structure equates with functional diversity," *Matrix Biol.*, vol. 30, no. 2, pp. 93–99, 2011.

[5] F. Koohestani, A. G. Braundmeier, A. Mahdian, J. Seo, J. J. Bi, and R. A. Nowak, "Extracellular matrix collagen alters cell proliferation and cell cycle progression of human uterine leiomyoma smooth muscle cells," *PLoS One*, vol. 8, no. 9, pp. 1–15, 2013.

[6] L. R. Smith, S. Cho, and D. E. Discher, "Stem Cell Differentiation is Regulated by Extracellular Matrix Mechanics," *Physiology*, vol. 33, no. 1, pp. 16–25, 2018.

[7] H. Makino, H. Sugiyama, and N. Kashihara, "Apoptosis and extracellular matrix–cell interactions in kidney disease," *Kidney Int.*, vol. 58, pp. S67–S75, 2000.

[8] J. Kaur and D. P. Reinhardt, *Extracellular Matrix (ECM) Molecules*.

Elsevier Inc., 2014.

[9] K. Y. Tsang, M. C. H. Cheung, D. Chan, and K. S. E. Cheah, "The developmental roles of the extracellular matrix: beyond structure to regulation," *Cell Tissue Res.*, vol. 339, no. 1, pp. 93–110, 2010.

[10] R. O. Hynes and A. Naba, "Overview of the matrisome-An inventory of extracellular matrix constituents and functions," *Cold Spring Harb. Perspect. Biol.*, vol. 4, no. 1, pp. 1–16, 2012.

[11] S. Ricard-Blum, "The Collagen Family," *Cold Spring Harb. Perspect. Biol.*, vol. 3, no. 1, pp. 1–19, 2011.

[12] H. M. Kagan, *Biology of Extracellular Matrix*, vol. 1. 1986.

[13] J. Myllyharju and K. I. Kivirikko, "Collagens, modifying enzymes and their mutations in humans, flies and worms," *Trends Genet.*, vol. 20, no. 1, pp. 33–43, 2004.

[14] P. Fratzl, *Collagen: Structure and mechanics, an introduction*. 2008.

[15] M. K. Gordon and R. A. Hahn, "Collagens," *Cell Tissue Res.*, vol. 339, no. 1, pp. 247–257, 2010.

[16] R. E. Pierschbacher MD, "Variants of the cell recognition site of fibronectin that retain attachment-promoting activity," *Proc. Natl. Acad. Sci.*, vol. 82, no. 1, pp. 258 LP – 258, Jan. 1985.

[17] O. F. Histochemistry, "THE ELASTIC A REVIEW " 2 the," *Russell J. Bertrand Russell Arch.*, 1973.

[18] R. P. Visconti, J. L. Barth, F. W. Keeley, and C. D. Little,

"Codistribution analysis of elastin and related fibrillar proteins in early vertebrate development," *Matrix Biol.*, vol. 22, no. 2, pp. 109–121, 2003.

[19] J. K. Mouw *et al.*, "HHS Public Access," vol. 15, no. 12, pp. 771–785, 2015.

[20] K. Von Der Mark, J. Park, S. Bauer, and P. Schmuki, "Nanoscale engineering of biomimetic surfaces: Cues from the extracellular matrix," *Cell Tissue Res.*, vol. 339, no. 1, pp. 131–153, 2010.

[21] L. Schaefer and R. M. Schaefer, "Proteoglycans: From structural compounds to signaling molecules," *Cell Tissue Res.*, vol. 339, no. 1, pp. 237–246, 2010.

[22] L. Zhang, *Glycosaminoglycan (GAG) biosynthesis and GAG-binding proteins*, 1st ed., vol. 93, no. C. Elsevier Inc., 2010.

[23] S. E McGowan, *Extracellular matrix and the regulation of lung development*, vol. 6. 1992.

[24] D. Chanda *et al.*, "Developmental Reprogramming in Mesenchymal Stromal Cells of Human Subjects with Idiopathic Pulmonary Fibrosis," *Sci. Rep.*, vol. 6, no. October, pp. 1–12, 2016.

[25] C. Coraux, G. Meneguzzi, P. Rousselle, E. Puchelle, and D. Gaillard, "Distribution of laminin 5, integrin receptors, and branching morphogenesis during human fetal lung development," *Dev. Dyn.*, vol. 225, no. 2, pp. 176–185, 2002.

[26] B. H. Gu, M. C. Madison, D. Corry, and F. Kheradmand, "Matrix remodeling in chronic lung diseases," *Matrix Biol.*, vol. 73, pp. 52–

63, 2018.

[27] P. Dutov, O. Antipova, S. Varma, J. P. R. O. Orgel, and J. D. Schieber, “Measurement of elastic modulus of collagen type i single fiber,” *PLoS One*, vol. 11, no. 1, pp. 1–13, 2016.

[28] R. Akhtar, “Nanoindentation of histological specimens,” *J. Mater.*, vol. 24, no. 3, pp. 638–646, 2010.

[29] P. R. Rocco *et al.*, “Lung tissue mechanics and extracellular matrix remodeling in acute lung injury,” *Am. J. Respir. Crit. Care Med.*, vol. 164, pp. 1067–1071, 2001.

[30] S. Ricard-Blum and F. Ruggiero, “The collagen superfamily: From the extracellular matrix to the cell membrane,” *Pathol. Biol.*, vol. 53, no. 7, pp. 430–442, 2005.

[31] J. Balestrini and L. E. Niklason, “Extracellular matrix as a driver for lung regeneration,” vol. 43, no. 3, pp. 568–576, 2015.

[32] A. J. Hance, K. Bradley, and R. G. Crystal, “Lung collagen heterogeneity. Synthesis of type I and type III collagen by rabbit and human lung cells in culture.,” *J. Clin. Invest.*, vol. 57, no. 1, pp. 102–11, 1976.

[33] H. Konomi, T. Hayashi, K. Nakayasu, and M. Arima, “Localization of type V collagen and type IV collagen in human cornea, lung, and skin. Immunohistochemical evidence by anti-collagen antibodies characterized by immunoelectroblotting,” *Am J Pathol*, vol. 116, no. 3, pp. 417–426, 1984.

[34] B. C. Starcher, “Elastin and the lung,” *Thorax*, vol. 41, no. 8, pp. 577–

585, 1986.

[35] A. Shifren, "The Stumbling Block in Lung Repair of Emphysema: Elastic Fiber Assembly," *Proc. Am. Thorac. Soc.*, vol. 3, no. 5, pp. 428–433, 2006.

[36] Z. Indik and H. Yeh, "Alternative splicing of human elastin mRNA indicated by sequence analysis of cloned genomic and complementary DNA," *Proc. Natl. Acad. Sci.*, vol. 84, no. 16, pp. 5680–4, 1987.

[37] K. Sekiguchi and S. Hakomori, "Domain Structure of Human Plasma Fibronectin," *J. Biol. Chem*, vol. 258, no. 5, pp. 3967–3973, 1983.

[38] R. Pankov, "Fibronectin at a glance," *J. Cell Sci.*, vol. 115, no. 20, pp. 3861–3863, 2002.

[39] R. Timpl and J. C. Brown, "The laminins.," *Matrix Biol.*, vol. 14, no. 4, pp. 275–281, 1994.

[40] T. Ahrens *et al.*, "CD44 is the principal mediator of hyaluronic-acid-induced melanoma cell proliferation," *J. Invest. Dermatol.*, vol. 116, no. 1, pp. 93–101, 2001.

[41] B. P. Toole, T. N. Wight, and M. I. Tammi, "Hyaluronan-cell interactions in cancer and vascular disease," *J. Biol. Chem.*, vol. 277, no. 7, pp. 4593–4596, 2002.

[42] B. Delpech, N. Girard, P. Bertrand, M.-N. N. Courel, C. Chauzy, and A. DELPECH, "Hyaluronan: fundamental principles and applications in cancer.," *J. Intern. Med.*, vol. 242, no. 1, pp. 41–48,

1997.

[43] J. Necas, L. Bartosikova, P. Brauner, and J. Kolar, "Hyaluronic acid (hyaluronan): A review," *Vet. Med. (Praha).*, vol. 53, no. 8, pp. 397–411, 2008.

[44] J. K. Burgess, T. Mauad, G. Tjin, J. C. Karlsson, and G. Westergren-Thorsson, "The extracellular matrix – the under-recognized element in lung disease?," *J. Pathol.*, vol. 240, no. 4, pp. 397–409, 2016.

[45] E. S. White, "Lung extracellular matrix and fibroblast function," *Ann. Am. Thorac. Soc.*, vol. 12, no. March, pp. S30–S33, 2015.

[46] M. R. Lang, G. W. Fiaux, M. Gillooly, J. A. Stewart, D. J. S. Hulmes, and D. Lamb, "Collagen content of alveolar wall tissue in emphysematous and non-emphysematous lungs," *Thorax*, vol. 49, no. 4, pp. 319–326, 1994.

[47] B. C. Starcher and M. J. Galione, "Purification and comparison of elastins from different animal species," *Anal. Biochem.*, vol. 74, no. 2, pp. 441–447, 1976.

[48] M. Matsuda, Y. C. Fung, and S. S. Sobin, "Collagen and elastin fibers in human pulmonary alveolar mouths and ducts.," *J. Appl. Physiol.*, vol. 63, no. 3, pp. 1185–1194, 1987.

[49] W. Wagner *et al.*, "Elastin Cables Define the Axial Connective Tissue System in the Murine Lung," *Anat. Rec.*, vol. 298, no. 11, pp. 1960–1968, 2015.

[50] C. A. Vaccaro and J. S. Brody, "Structural features of alveolar wall

basement membrane in the adult rat lung," *J. Cell Biol.*, vol. 91, no. 2 I, pp. 427–437, 1981.

[51] M. I. Townsley, "Structure and composition of pulmonary arteries, capillaries and veins," *Compr. Physiol.*, vol. 2, pp. 675–709, 2013.

[52] A. Shkumatov *et al.*, "Matrix stiffness-modulated proliferation and secretory function of the airway smooth muscle cells," *Am. J. Physiol. - Lung Cell. Mol. Physiol.*, vol. 308, no. 11, pp. L1125–L1135, 2015.

[53] T. Luque *et al.*, "Local micromechanical properties of decellularized lung scaffolds measured with atomic force microscopy," *Acta Biomater.*, vol. 9, no. 6, pp. 6852–6859, 2013.

[54] A. J. Booth *et al.*, "Acellular normal and fibrotic human lung matrices as a culture system for in vitro investigation," *Am. J. Respir. Crit. Care Med.*, vol. 186, no. 9, pp. 866–876, 2012.

[55] A. J. Haak, Q. Tan, and D. J. Tschumperlin, "Matrix biomechanics and dynamics in pulmonary fibrosis," *Matrix Biol.*, vol. 73, pp. 64–76, 2017.

[56] N. I. of H. NIH, "Asthma." .

[57] H. L. Huber, "The pathology of bronchial asthma," *Arch. Intern. Med.*, vol. 30, no. 4, 1922.

[58] W. R. Roche, J. H. Williams, R. Beasley, and S. T. Holgate, "Subepithelial Fibrosis in the Bronchi of Asthmatics," *Lancet*, vol. 333, no. 8637, pp. 520–524, 1989.

[59] P. K. Jeffery, A. J. Wardlaw, F. C. Nelson, J. V. Collins, and A. B. Kay,

"Bronchial Biopsies in Asthma," *Am. Rev. Respir. Dis.*, no. 140, pp. 1745–1753, 1989.

[60] M. Weitoft *et al.*, "Controlled and uncontrolled asthma display distinct alveolar tissue matrix compositions," *Respir. Res.*, vol. 15, no. 1, pp. 1–13, 2014.

[61] L. Richeldi, H. R. Collard, and M. G. Jones, "Idiopathic pulmonary fibrosis," *Lancet*, vol. 389, no. 10082, pp. 1941–1952, 2017.

[62] I. E. Fernandez and O. Eickelberg, "New cellular and molecular mechanisms of lung injury and fi brosis in idiopathic pulmonary fi brosis," *Lancet*, vol. 380, no. 9842, pp. 680–688, 2012.

[63] C. J. Scotton and R. C. Chambers, "Molecular targets in pulmonary fibrosis: The myofibroblast in focus," *Chest*, vol. 132, no. 4, pp. 1311–1321, 2007.

[64] N. Enomoto *et al.*, "Amount of elastic fibers predicts prognosis of idiopathic pulmonary fibrosis," *Respir. Med.*, vol. 107, no. 10, pp. 1608–1616, 2013.

[65] Y. Fukuda, Y. Masuda, M. Ishizaki, Y. Masugi, and V. J. Ferrans, "Morphogenesis of abnormal elastic fibers in lungs of patients with panacinar and centriacinar emphysema," *Hum. Pathol.*, vol. 20, no. 7, pp. 652–659, 1989.

[66] R. Annoni *et al.*, "Extracellular matrix composition in COPD," *Eur. Respir. J.*, vol. 40, no. 6, pp. 1362–1373, 2012.

[67] S. J. Hirst, C. H. Twort, and T. H. Lee, "Differential effects of extracellular matrix proteins on human airway smooth muscle

cell proliferation and phenotype," *Am J Respir Cell Mol Biol*, vol. 23, no. 3, pp. 335–344, 2000.

[68] P. R. A. Johnson *et al.*, "Extracellular matrix proteins modulate asthmatic airway smooth muscle cell proliferation via an autocrine mechanism," *J. Allergy Clin. Immunol.*, vol. 113, no. 4, pp. 690–696, 2004.

[69] G. Charras and E. Sahai, "Physical influences of the extracellular environment on cell migration," *Nat. Rev. Mol. Cell Biol.*, vol. 15, no. 12, pp. 813–824, 2014.

[70] J. R. Gershlak and L. D. Black, "Beta 1 integrin binding plays a role in the constant traction force generation in response to varying stiffness for cells grown on mature cardiac extracellular matrix," *Exp. Cell Res.*, vol. 330, no. 2, pp. 311–324, 2015.

[71] K. Larsen *et al.*, "Presence of activated mobile fibroblasts in bronchoalveolar lavage from patients with mild asthma," *Am. J. Respir. Crit. Care Med.*, vol. 170, no. 10, pp. 1049–1056, 2004.

3

THE ECM AFFECTS THE HALLMARKS OF CANCER

3.1 THE HALLMARKS OF CANCER

The hallmarks of cancer are composed of six biological capabilities which cancer acquires during the multistep development of human tumors. These are sustaining proliferative signaling, evading growth suppressors, resisting cell death, enabling replicative immortality, inducing angiogenesis and activating invasion and metastasis as listed by Hanahan and Weinberg in 2000 [1]. These six hallmarks of cancer still provide nowadays a solid foundation for understanding the biology of cancer. Although two more have been added as emerging hallmarks and other two as cancer enabling characteristics.

The two new hallmarks proposed by Hanahan and Weinberg in 2011 [2] were: (1) Reprogramming energy metabolism, which gathers not just the deregulated control of cell proliferation but also the corresponding adjustments of energy metabolism in order to fuel cell growth and division, and (2) Evading immune destruction which notes the capacity of the cancerous tissue or tumor to avoid detection by the immune system or the ability of it to limit the extent of immunological killing, evading eradication.

With these two new hallmarks, two enabling characteristics have been added too: (1) genome instability and mutation, which claims that certain mutant genotypes confer selective advantage on subclones of cells, enabling their outgrowth and eventual dominance in a local tissue environment and (2) tumor-promoting inflammation, which can be considered as an enabling characteristic due to its contributions to the acquisition of core hallmark capabilities by supplying bioactive molecules to the tumor microenvironment.

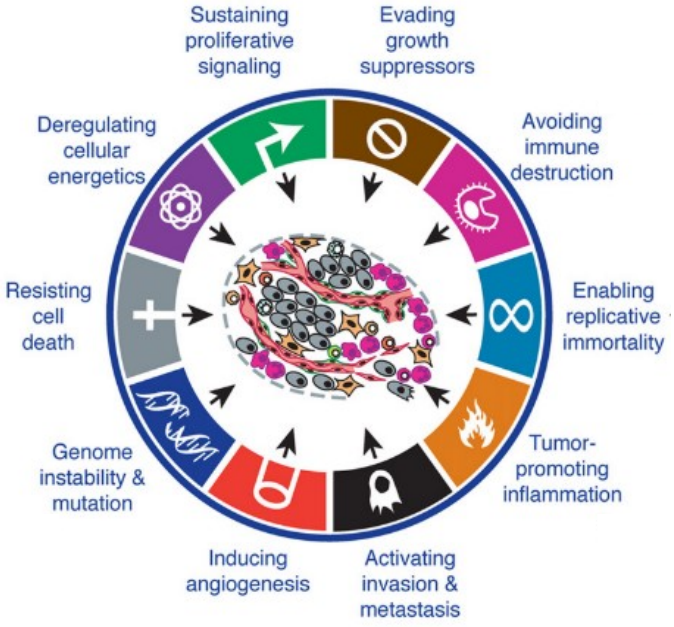

Figure 3.1 The hallmarks of cancer [2]

3.2 THE RELATIONSHIP BETWEEN THE ECM AND THE HALLMARKS OF CANCER

The extracellular matrix helps in the regulation of tissue development and homeostasis, and its dysregulation can contribute to neoplastic progression. As explained before, the ECM does not just act like a scaffold for the cells so tissues can be organized but provides essential biochemical and biomechanical factors than can direct cell growth, survival, migration and differentiation and can change the vascular development and immune function.

The ECM regulates tissue development and is responsible for the maintenance of tissue homeostasis [3]. The ECM is a complex network of macromolecules that form a three-dimensional assembly creating supramolecular structures with distinct biochemical and biomechanical properties that regulate cell behavior. Differentiation, survival, motility and cell growth are regulated by ligating specific receptors such as integrins, syndecans and discoidin receptors [4], [5]. It also provides mechanical structure and mechanical integrity for tissue function, regulates the availability of growth factors and cytokines, keeps the hydration, and maintains the pH of the surrounding microenvironment.

Tumors usually display desmoplasia, an increased deposition of connective tissue and an altered organization and post-translational modifications of the ECM proteins [6]. The stromal desmoplasia has been also shown in patients and has been related to tumor progression [7].Another example in breast cancer is the increased mammographic density, which is associated with an increased collagen deposition and

correlates with an elevated risk of developing breast cancer [8]. In fact, high mechanical stress is a predictive way of detecting tumor formation in breast cancer patients [9]. All these studies suggest that the biochemical and biophysical properties of the ECM should be considered when studying cancer behavior.

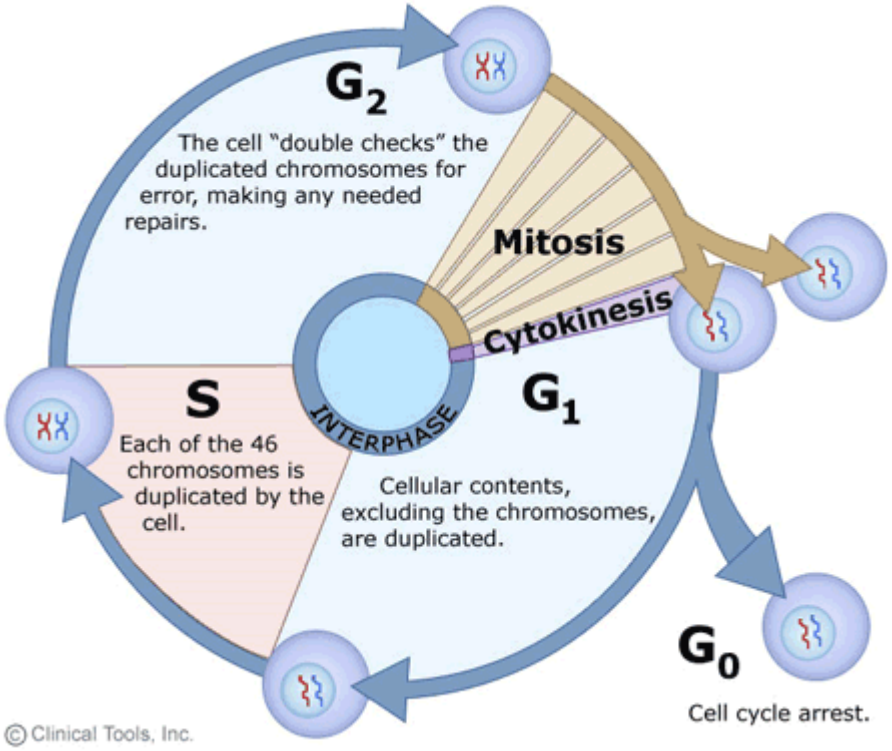

Figure 3.2 The cell cycle

3.2.1 Sustaining proliferative signaling.

Escaping from cell-cycle arrest is required so cells can transform and the tumors can progress. Proliferation starts with the ligation of growth

factor receptors whose activation promotes intracellular signaling that helps with cell cycle progression. This progression is controlled by the G1/S cycle checkpoint (Figure 3.2), which requires cellular adhesion to the ECM. Malignant cells have the ability to secrete their own ECM ligands so they are able to escape the proliferative suppression to grow [10]. These type of cells seem to be highly metastatic, indeed, transformation by some oncogenes (Ras) that promote anchorage independence for growth and survival, induce the expression of various ECM proteins such as fibronectin, tenascin C, or laminin [11]. A malignant tissue is usually stiffer than a normal tissue, this property is mediated by a highly cross-linked and oriented collagenous ECM [6]. A stiffened ECM associates with cancer and correlates with an increased propensity toward metastasis since cells interacting with a stiffer ECM proliferate more in response to growth factors end express genes that correlate with proliferation [12]. For example, hepatocytes, when cultured on thin and stiff films of monomeric collagen, spread, proliferate, and otherwise adopt a dedifferentiated phenotype, while on soft gels of fibrillar collagen, they remain differentiated and growth arrested [13]. As the rigidity of the gels increases, so does cycle progression and dedifferentiation [13], [14]. In summary, the ECM and the ECM receptors can regulate cell proliferation, while corruption of these interactions can modulate tumor progression.

Lung tumor metastasis is facilitated by ECM pre-conditioning, stiffening due to lysyl oxidase and enhanced fibronectin deposition may promote tumor cell growth and survival by overriding the activity of the tumor suppressors, in fact, a stiff ECM reduces the expression of genes that are expressed during cell cycle suppression [15], [16].

3.2.2 Resisting cell death

Once the cells suffer a malignant transformation, also gain the ability to overcome cell death. Oncogenic transformation is usually accompanied by the addition of anchorage-independent survival (anoikis suppression) [17]. ECM ligation can also enhance a cell's ability to resist apoptosis. For example, breast tumor stiffness, which is associated with elevated integrin signaling, associates with reduced adjuvant chemotherapeutic treatment responsiveness [18].

3.2.3 Enabling replicative immortality

Previously mentioned unrestrained growth of many tumors is associated with replicative immortality. Differentiated non-cancerous cells show limited replicative capabilities due to the shortening of telomeres after cell division. Telomeres are regions of the end of each chromosome with a noncoding nucleotide sequence. Cancer cells can overcome this limitation by expressing the enzyme telomerase, which can elongate the telomeres and overcome replicative senescence [19]. Patients with idiopathic pulmonary fibrosis, which is characterized by a tissue stiffening due to the increased deposition of ECM proteins, exhibit elevated levels of telomerase, which suggest that an increased adhesion to the ECM may influence cells during replication[20]. Also, epithelial cells expressing high levels of CD29 integrin showed high telomerase activity [21].

3.2.4 Inducing angiogenesis

Tumors have the ability to neo-vascularize the tissue to provide the oxygen and nutrients required for their growth [22]. Angiogenesis is

stimulated by growth factors and involves the migration and proliferation of endothelial cells into the regions adjacent to the tumor followed by their assembly into the blood vessels [23]. The ECM that surrounds the tumor acts as a reservoir and provides a conduit for the migration of endothelial cells, and promotes the growth and survival of newly recruited neighbor endothelial cells [24], [25]. The stiffened ECM of a tumor also favors angiogenesis by promoting endothelial cell migration, cell growth and survival[26], [27]. Regardless, stiff ECM can also compromise vascular integrity and activate MMPs (matrix metalloproteinase) that degrade the ECM releasing antiangiogenic factors. The ECM can both promote and inhibit angiogenesis [28].

3.2.5 Activating invasion and metastasis

Cells can acquire an invasive phenotype to invade the adjacent parenchyma [29]. Invadopodia, protrusions that are rich in actin [30], require integrin-mediated adhesion and focal adhesion formation and are able to guide tumor cell invasion by localized MMP-mediated matrix degradation [31]. Invadopodia formation can be promoted by ECM stiffness, enhancing tumor cell invasion by driving focal adhesion assembly [32]. Inside the parenchyma, metastasis depends on the successful intravasation into the circulatory/lymphatic system, where the cell can be transported to the secondary site, the target tissue to form a viable tumor colony [33]. The metastatic capability of a tumor cell is favored by an epithelial to mesenchymal transition (EMT), which happens promoted by TGF-β secreted by immune cells [34] or the localized degradation of the ECM [35], [36]. A stiff ECM can promote TGF-β induced EMT, inducing a basal-like cell phenotype to stimulate cancer

metastasis [37]. On the contrary, inhibiting collagen crosslinking, reducing matrix stiffening can prevent tumor metastasis [38]. To summarize, malignant transformation and metastasis is promoted by the ECM, regulating tumor plasticity and fostering integrin-dependent cell adhesion and migration.

3.2.6 Avoiding immune destruction

Immune survival by the adaptation of the immune response is a key physiological mechanism that prevents tumor formation. Relies in the ability of cytotoxic T-cells to recognize foreign or mutated antigens, which appear on transformed cells, so cell death can be induced through the T-cells. The ECM can help and thwart the adaptive tumor immune response. One of the proimmunogenic activities is generating migratory "highways" for helping the T cells invade the tissue [39], in response to chemoattractive ECM components released by MMPs [40]. T-cell activity can also be frustrated by the ECM through the impairment of antigen presentation by APCs (Antigen Presenting Cells) [41].

3.2.7 Deregulating cellular energetics

This hallmark is based in the metabolic reprogramming of tumor cells. The tumor cells shift from aerobic glycolysis toward anaerobic glycolysis producing only 2 ATP instead of 36 ATP. This switch permits the tumor to use glucose for other regulatory processes such as protein synthesis and cell division [42]. This affects the tumor cell division speed, making it as faster as proliferative tumor cells are. Even in the presence of high oxygen concentration, tumor cells exploit the anaerobic metabolic process to reinforce rapid cell division [43].

The ECM is essential for the uptake of extracellular nutrients and the production of ATP. Focal adhesion signaling mediates the transmission of ECM signals into the tumor cells which activates pathway which increases glycolysis [44]. Also, tumor cells interacting with a stiffened ECM show an upregulation of growth factor dependent signaling, increasing aerobic glycolysis, which suggests that tissue stiffness may directly regulate tumor cell metabolism [45].

Mechanical cues can regulate glycolysis via cytoskeleton architecture. The results in [46] show a mechanism by which glycolysis responds to architectural features of the actomyosin cytoskeleton, thus coupling cell metabolism to the mechanical properties of the surrounding tissue. These processes enable normal cells to tune energy production in variable microenvironments, whereas the resistance of the cytoskeleton in response to mechanical cues enables the persistence of high glycolytic rates in cancer cells.

3.3 BIBLIOGRAPHY

[1] D. Hanahan and R. A. Weinberg, "The hallmarks of cancer.," *Cell*, vol. 100, no. 1, pp. 57–70, 2000.

[2] D. Hanahan and Robert A. Weinberg, "Hallmarks of Cancer: The Next Generation," *Cell*, vol. 144, no. March 4, pp. 646–674, 2011.

[3] T. Mammoto and D. E. Ingber, "Mechanical control of tissue and organ development," *Development*, vol. 137, no. 9, pp. 1407–1420, 2010.

[4] B. Leitinger and E. Hohenester, "Mammalian collagen receptors," *Matrix Biol.*, vol. 26, no. 3, pp. 146–155, 2007.

[5] X. Xian, S. Gopal, and J. R. Couchman, "Syndecans as receptors and organizers of the extracellular matrix," *Cell Tissue Res.*, vol. 339, no. 1, pp. 31–46, 2010.

[6] P. Lu, V. M. Weaver, and Z. Werb, "The extracellular matrix: A dynamic niche in cancer progression," *J. Cell Biol.*, vol. 196, no. 4, pp. 395–406, 2012.

[7] Pandol Stephen, "Desmoplasia of Pancreatic Ductal Adenocarcinoma," *Clin Gastroenterol Hepatol*, vol. 7, no. 11 0, pp. 1–9, 2009.

[8] and M. J. Y. Norman F Boyd, Helen Guo, Lisa J.Martin, Limei Sun, Jennifer Stone, Eve Fishell, Roberta A Jong, Greg Hislop, Anna Chiarelli, Salomon Minkin, "Mammographic Breast Density and the Risk and Detection of Breast Cancer," *`New Engl. J. Med.*, vol. 356, pp. 227–236, 2007.

[9] E. Boghaert, J. P. Gleghorn, K. Lee, N. Gjorevski, D. C. Radisky, and C. M. Nelson, "Host epithelial geometry regulates breast cancer cell invasiveness," *Proc. Natl. Acad. Sci.*, vol. 109, no. 48, pp. 19632–19637, 2012.

[10] N. Zahir and V. M. Weaver, "Death in the third dimension: Apoptosis regulation and tissue architecture," *Curr. Opin. Genet. Dev.*, vol. 14, no. 1, pp. 71–80, 2004.

[11] P. P. Pattabiraman and P. V. Rao, "Mechanistic basis of Rho GTPase-induced extracellular matrix synthesis in trabecular meshwork cells," *Am. J. Physiol. Physiol.*, vol. 298, no. 3, pp. C749–C763, 2010.

[12] R. G. Wells, "The role of matrix stiffness in regulating cell behavior," *Hepatology*, vol. 47, no. 4, pp. 1394–1400, 2008.

[13] L. K. Hansen, J. Wilhelm, and J. T. Fassett, "Regulation of Hepatocyte Cell Cycle Progression and Differentiation by Type I Collagen Structure," *Curr. Top. Dev. Biol.*, vol. 72, no. 05, pp. 205–236, 2005.

[14] E. J. Semler, C. S. Ranucci, and P. V. Moghe, "Mechanochemical manipulation of hepatocyte aggregation can selectively induce or repress liver-specific function," *Biotechnol. Bioeng.*, vol. 69, no. 4, pp. 359–369, 2000.

[15] J. T. Erler *et al.*, "Hypoxia-induced lysyl oxidase is a critical mediator of bone marrow cell recruitment to form the pre-metastatic niche," *Cancer Cell*, vol. 15, no. 1, pp. 35–44, 2009.

[16] E. S. White, "Lung extracellular matrix and fibroblast function," *Ann. Am. Thorac. Soc.*, vol. 12, no. March, pp. S30–S33, 2015.

[17] M. J. Reginato *et al.*, "Integrins and EGFR coordinately regulate the pro-apoptotic protein Bim to prevent anoikis," *Nat. Cell Biol.*, vol. 5, no. 8, pp. 733–740, 2003.

[18] M. Hayashi *et al.*, "Evaluation of tumor stiffness by elastography is predictive for pathologic complete response to neoadjuvant chemotherapy in patients with breast cancer," *Ann. Surg. Oncol.*, vol. 19, no. 9, pp. 3042–3049, 2012.

[19] J. Erenpreisa and M. S. Cragg, "Three steps to the immortality of cancer cells: Senescence, polyploidy and self-renewal," *Cancer Cell Int.*, vol. 13, no. 1, pp. 1–12, 2013.

[20] T. Liu *et al.*, "Telomerase activity is required for bleomycin-induced pulmonary fibrosis in mice," *J. Clin. Invest.*, vol. 117, no. 12, pp. 3800–3809, 2007.

[21] C. Kunimura, K. Kikuchi, N. Ahmed, A. Shimizi, and S. Yasumoto, "Telomerase activity in a specific cell subset co-expressing integrin β1/EGFR but not p75(NGFR)/bcl2/integrin β4 in normal human epithelial cells," *Oncogene*, vol. 17, no. 2, pp. 187–197, 1998.

[22] J. Zhou, T. Schmid, S. Schnitzer, and B. Brüne, "Tumor hypoxia and cancer progression," *Cancer Lett.*, vol. 237, no. 1, pp. 10–21, 2006.

[23] G. Bergers and L. E. Benjamin, "Tumorigenesis and the angiogenic switch," *Nat. Rev. Cancer*, vol. 3, no. 6, pp. 401–410, 2003.

[24] C. J. Avraamides, B. Garmy-susini, and J. A. Varner, "Integrins in

angiogenesis and lymphangiogenesis Christie," *Nat Rev Cancer.*, vol. 8, no. 8, pp. 604–617, 2008.

[25] R. O. Hynes, "Cell – matrix adhesion in vascular development," vol. 5, pp. 32–40, 2007.

[26] J. Liu and S. Agarwal, "Mechanical Signals Activate Vascular Endothelial Growth Factor Receptor-2 To Upregulate Endothelial Cell Proliferation during Inflammation," *J. Immunol.*, vol. 185, no. 2, pp. 1215–1221, 2010.

[27] A. Mammoto *et al.*, "A mechanosensitive transcriptional mechanism that controls angiogenesis," vol. 457, no. 7233, pp. 1103–1108, 2009.

[28] R. A. Jones *et al.*, "Matrix changes induced by transglutaminase 2 lead to inhibition of angiogenesis and tumor growth," *Cell Death Differ.*, vol. 13, no. 9, pp. 1442–1453, 2006.

[29] D. X. Nguyen, P. D. Bos, and J. Massagué, "Metastasis: From dissemination to organ-specific colonization," *Nat. Rev. Cancer*, vol. 9, no. 4, pp. 274–284, 2009.

[30] B. T. Beaty and J. Condeelis, "Digging a little deeper: The stages of invadopodium formation and maturation," *Eur. J. Cell Biol.*, vol. 93, no. 10–12, pp. 438–444, 2014.

[31] Y. Wang and M. A. McNiven, "Invasive matrix degradation at focal adhesions occurs via protease recruitment by a FAK-p130Cas complex," *J. Cell Biol.*, vol. 196, no. 3, pp. 375–385, 2012.

[32] A. Parekh *et al.*, "Sensing and modulation of invadopodia across a

wide range of rigidities," *Biophys. J.*, vol. 100, no. 3, pp. 573–582, 2011.

[33] Q. N. Usbotjujpo *et al.*, "Epithelial-mesenchymal transition can suppress major attributes of human epithelial tumor-initiating cells," *J. Clin. Invest.*, vol. 122, no. 5, 2012.

[34] A. V. Bakin, A. K. Tomlinson, N. A. Bhowmick, H. L. Moses, and C. L. Arteaga, "Phosphatidylinositol 3-kinase function is required for transforming growth factor ??-mediated epithelial to mesenchymal transition and cell migration," *J. Biol. Chem.*, vol. 275, no. 47, pp. 36803–36810, 2000.

[35] A. Pathak and S. Kumar, "Independent regulation of tumor cell migration by matrix stiffness and confinement," vol. 109, no. 26, pp. 10334–10339, Jun. 2012.

[36] S. Menon and K. A. Beningo, "Cancer cell invasion is enhanced by applied mechanical stimulation," *PLoS One*, vol. 6, no. 2, 2011.

[37] J. L. Leight, M. A. Wozniak, S. Chen, M. L. Lynch, and C. S. Chen, "Matrix rigidity regulates a switch between TGF- 1-induced apoptosis and epithelial-mesenchymal transition," *Mol. Biol. Cell*, vol. 23, no. 5, pp. 781–791, 2012.

[38] M. Barton Laws *et al.*, "Stromally Derived Lysyl Oxidase Promotes Metastasis of Transforming Growth Factor-β Deficient Mouse Mammary Carcinomas," *NIH Public access*, vol. 17, no. 1, pp. 148–159, 2013.

[39] L. Sorokin, "The impact of the extracellular matrix on

inflammation," *Nat. Rev. Immunol.*, vol. 10, no. 10, pp. 712–723, 2010.

[40] L. Meyaard, "The inhibitory collagen receptor LAIR-1 (CD305)," *J. Leukoc. Biol.*, vol. 83, no. 4, pp. 799–803, 2008.

[41] M. D. Vesely, M. H. Kershaw, R. D. Schreiber, and M. J. Smyth, "Natural Innate and Adaptive Immunity to Cancer," *Annu. Rev. Immunol.*, vol. 29, no. 1, pp. 235–271, 2011.

[42] M. Israël and L. Schwartz, "The metabolic advantage of tumor cells," *Mol. Cancer*, vol. 10, no. 1, p. 70, 2011.

[43] R. J. Gillies, I. Robey, and R. A. Gatenby, "Causes and Consequences of Increased Glucose Metabolism of Cancers," *J. Nucl. Med.*, vol. 49, no. Suppl_2, pp. 24S-42S, 2008.

[44] Matthew G. Vander Heiden, Lewis C. Cantley, and Craig B. Thompson, "Understanding the Warburg Effect: The Metabolic Requirements of Cell Proliferation," *Science (80-.).*, vol. 324, no. may, pp. 1029–1033, 2009.

[45] R. L. Elstrom *et al.*, "Akt stimulates aerobic glycolysis in cancer cells," *Cancer Res.*, vol. 64, no. 11, pp. 3892–3899, 2004.

[46] J. S. Park *et al.*, "Mechanical regulation of glycolysis via cytoskeleton architecture," *Nature*, vol. 578, no. 7796, pp. 621–626, 2020.

4

UNDERSTANDING THE COMPOSITION AND MECHANICAL PROPERTY CORRELATION IN NORMAL AND CANCEROUS HUMAN LUNG ECM

In this chapter, the mechanical properties of cancerous and non-cancerous ECM were investigated and correlated to the ECM composition. For this purpose, lung cancer patient samples have been studied. The Young´s moduli of cancerous and non-cancerous ECM were measured at the microscopic level, to study the correlation between ECM stiffness and the fibrillar proteins responsible for the structure and the mechanical properties of the tissue. This was achieved using a correlative microscopy setup where an Atomic Force Microscopy (AFM) and an Epifluorescence Microscopy were combined to observe the microstructure of the tissue at the AFM probing location, obtaining mechanical information as well as spatially resolved protein localization.

4.1 STATE OF THE ART

As mentioned before, one of the many critical functions of the ECM is to provide structural and mechanical integrity to the tissues, and many of the proteins that can be found in the ECM play these roles. The

composition of the ECM is variable between different tissues, depending on the functional needs of each. In solid tumors, the ECM changes and becomes more complex, influencing disease progression. Cancer cells can change the matrix composition and structure, changing at the same time the mechanical properties of the tumor microenvironment.

Tissues are comprised of ECM, cells, a vascular system and an amount of proteins, which are used by the cells for signaling. This composition can change depending on the location of the tissue and is dynamic in time. Tissues such as the heart or pancreas are dominated by their cellular content in term of function and mechanical stiffness. Some of the ECM proteins crosslink to form longer filaments that bundle into fibers and serve a large structural role: Collagen and Elastin are one of these proteins [1]. Elastin shows an entropic elastic behavior and can sustain high levels of strain without fracture [2]. However, collagen shows a non–linear mechanical behavior, is stiffer than elastin and is not able to bear high strains [3]. In collagen rich tissues, an increasing fraction of the filaments is associated generally with an increase in the stiffness.

One of the main differences between biological tissues and abiotic ones is the fact that biological tissues can remodel themselves in response to different factors. Cells can remodel the ECM by synthesizing new ECM proteins, altering the crosslinking grade or secreting enzymes such as metalloproteases which can break down matrix elements [1]. For the particular case of tumors, imaging of the ECM in cancer specimens demonstrate distinctive features from preclinical, clinical and in vitro samples, such as an increased collagen density and matrix alignment in the vicinity of tumors [4], [5].

Mechanics-based measurements are a form of measuring ECM physical properties in cancer tissues. Except from ultrasound elastography techniques which can measure in vivo [6], usually, these assays are performed ex vivo or in vitro due to the need of the contact between a mechanical probe and a sample to apply forces. Compression and shear tests have been applied to quantify the stiffness of ex vivo tumors. However, the measurements on the work of Madnes et al. [7] are in bulk, so they are not sensitive enough to measure the local heterogeneous mechanical properties of tissues. Indentation is a robust mechanical characterization method of compliant materials. By tuning the size of the indenter and the cantilever stiffness, indentation assays can offer high resolution micro and nanoscale quantification. Indentation and topography imaging tests by means of Atomic Force Microscopy have been key in the field of cancer biomechanics and have revealed lots of mechanical information about the microenvironment of the tumor at molecular, cellular and tissue level [8]–[12]. For example, the discrimination between normal an cancerous cells by M. Lekka et al. [11] where thyroid, breast, prostate, bladder and kidney cells were indented showing that the normal cells are stiffer than their cancerous analogous. Also, nanomechanical indentation tests performed via AFM on tissue slices, showed a high degree of heterogeneity in the stiffness [13], [14]. Recent AFM measurements suggested that the collagen remodeling of the cancerous ECM can lead to tumor stiffening which can trigger the ability of the cells to change from epithelial to mesenchymal (epithelial to mesenchymal transition), enhancing invasion of the tumor cells and metastasis [15].

The ECM mechanics significantly contributes to cancer progression and metastasis. However, the fundamentals of how cells change the microstructure affecting mechanical properties in understudied. Thus, there is a need to implement new techniques that can measure and resolve the changes in cancerous ECM mechanics and biological structure. Previously, AFM measurements were performed in decellularized mice lungs, giving, as a result, stiffness differences between the alveolar segments, junctions and pleura [16]. After that, the heterogeneity of the micromechanical properties of the extracellular matrix in healthy and infarcted decellularized mice hearts were measured and showed a 3 fold stiffness increment between the collagen rich infarcted and healthy zones [8].

This chapter aims to fill the gap in the literature of the study in situ of the micromechanical properties and microstructure of the cancerous and non-cancerous human lung ECM.

4.2 Materials and Methods

4.2.1 Samples

Lung ECM cuts were obtained from the biopsies of 7 lung cancer patients. Two consecutive cuts of approximately 7 µm of thickness were obtained, one to perform the AFM combined to immunofluorescence assays and the other one to make an Eosin and Hematoxylin staining. The slices were immobilized onto positively charged glass slides. Fixation was avoided

to maintain the mechanical properties of the tissue. For each patient, a pathologist identified the tumoral and non-tumoral zones on the eosin-hematoxylin stained cuts, as can be seen in Figure 4.1.

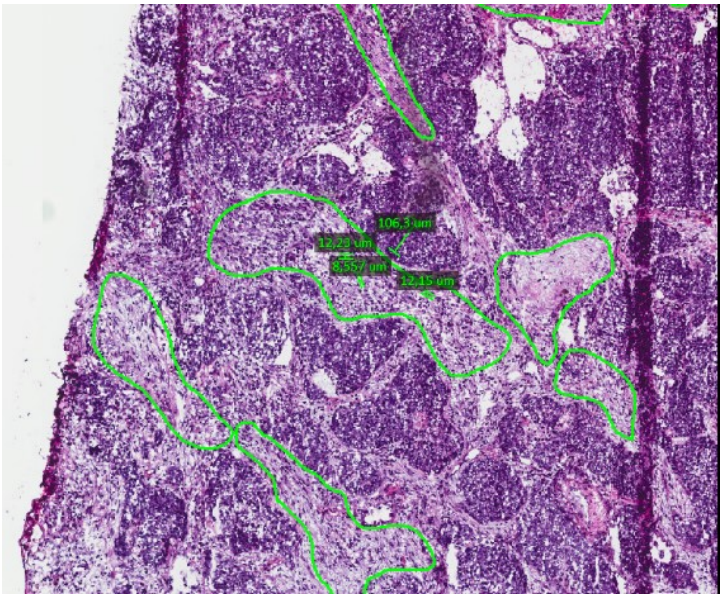

Figure 4.1 Eosin and hematoxylin staining for a cut of a lung cancer biopsy. The tumoral zones are marked in green.

4.2.2 Decellularization

Samples were decellularized in order to specifically address the mechanical behavior of the ECM. The slices with a 7 µm thickness were attached to glass slides previously treated with a glutaraldehyde solution. The samples were rinsed in PBS for 5 minutes, then the decellularization process was made in 1% of sodium dodecyl sulphate (SDS) for 10 minutes. After that, they were rinsed 2 times for 5 minutes in PBS.

4.2.3 Immunofluorescence staining

As mentioned in chapter 2, the most relevant fibers to describe lung ECM behavior are Collagen I, Collagen III and Elastin [17]. These three proteins were chosen for an immunofluorescence staining, using the next primary, Mouse anti Collagen I, Guinea pig anti Elastin and Rabbit anti Collagen III (Abcam®) and secondary antibodies Alexa488 Rabbit anti Mouse, 405 Donkey anti guinea Pig and Cy3 Goat anti Rabbit (Jackson Immunoresearch®) as shown in . The immunofluorescence staining for the primary antibodies was performed overnight at 4°C to ensure a correct coupling in each staining phase.

The samples were rinsed several times with a 10% PBS. A blocking Buffer (PBS1x +0.5% Triton + 1% BSA +6% FBS) was then added to block unspecific bindings of the antibodies and incubated for 45 minutes at room temperature. Then washed again for 5 minutes.

Then 50 µl of the primary antibodies' solution 1:200 in Dilution Buffer (PBS1x+0.1% Triton +0.1% BSA +6% FBS) and incubated overnight at 4°C. Samples where then washed three times for 5 minutes each wash.

Then 50 µl of the secondary antibodies' solution 1:200 in Dilution Buffer (PBS1x+0.1% Triton +0.1% BSA +6% FBS) and incubated for 60 minutes at room temperature covered from the light.

The samples where then washed three times for 5 minutes each wash and frozen at -20°C protected from the light until used.

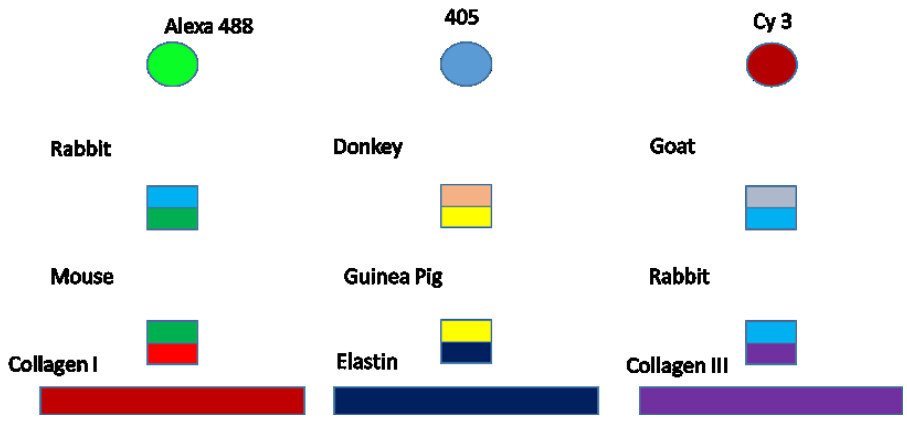

Figure 4.2 Simple scheme of the primary and secondary antibodies used during the immunofluorescence-staining assay.

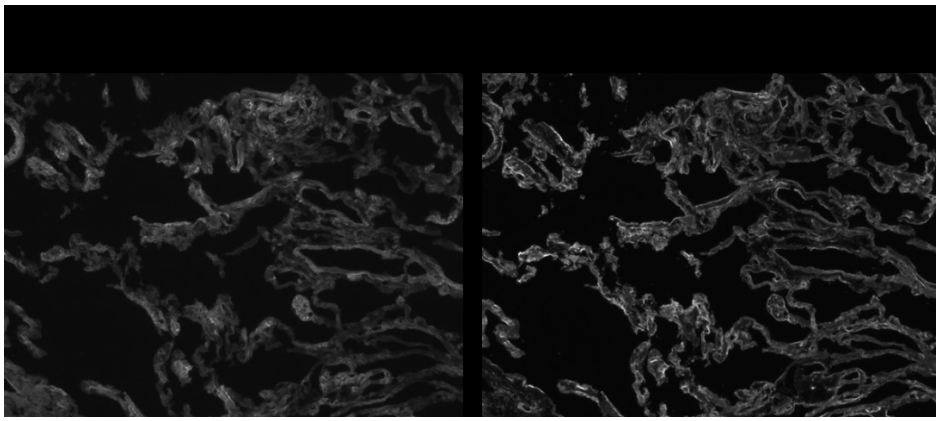

Figure 4.3 Collagen I (left) and Collagen III (right) after the new immunostaining protocol. Colocalization is not happening, Collagen III covers the Collagen I bundles as explained in [18].

4.2.4 AFM indentations correlated with fluorescence microscopy

A JPK®Nanowizard®IV head was mounted on the stage of a Nikon TE-Eclipse inverted microscope to obtain correlated AFM indentations and images of the indented area. Samples were illuminated with a cooled PE-300 LED microscope Illuminator, and the lens used for the assay was a 60X Nikon CFI APO NIR Objective, 1.0 NA, in water immersion. The whole set-up of the experiment is schematized in Figure 4.5, which represents all the steps followed undertaken to perform the combined AFM+ immunofluorescence assay.

Measurements were performed at room temperature with a 10 µm polystyrene sphere attached to cantilevers with a nominal spring constant (k_c) of 0.03 N/m (MLCT, Bruker, Mannheim, Germany). The spring constant of the cantilevers was calibrated by thermal tuning using the simple harmonic oscillator model. Photodiode calibration to obtain cantilever deflection (x) was performed on a bare region of the glass. The force exerted by the tip was computed as $F = k \cdot x$ [19], Figure 4.4.

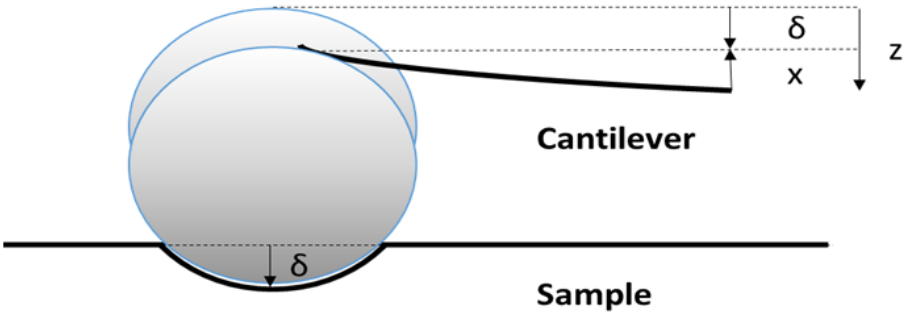

Figure 4.4 Indentation experiment. The cantilever moves to the sample a distance z which is the measured height. The cantilever bends in the opposite direction x, while the sample is indented a distance δ. The δ is calculated by subtracting the cantilever deflection from the height. The x can be calculated as the Force is equal to the spring constant of the cantilever by the displacement. F=kx.

For all the patients, measurements were taken in two histological regions previously identified by a pathologist: cancerous and non-cancerous. A 20x20 point map was taken separated by 5µm in a 100µm*100µm area in each region for each patient, making a total of 400 indentations per region and 800 indentations per patient. The indentations were performed in PBS at 37°C to avoid any humidity or temperature variation that could change the mechanical properties or the composition of the tissue.

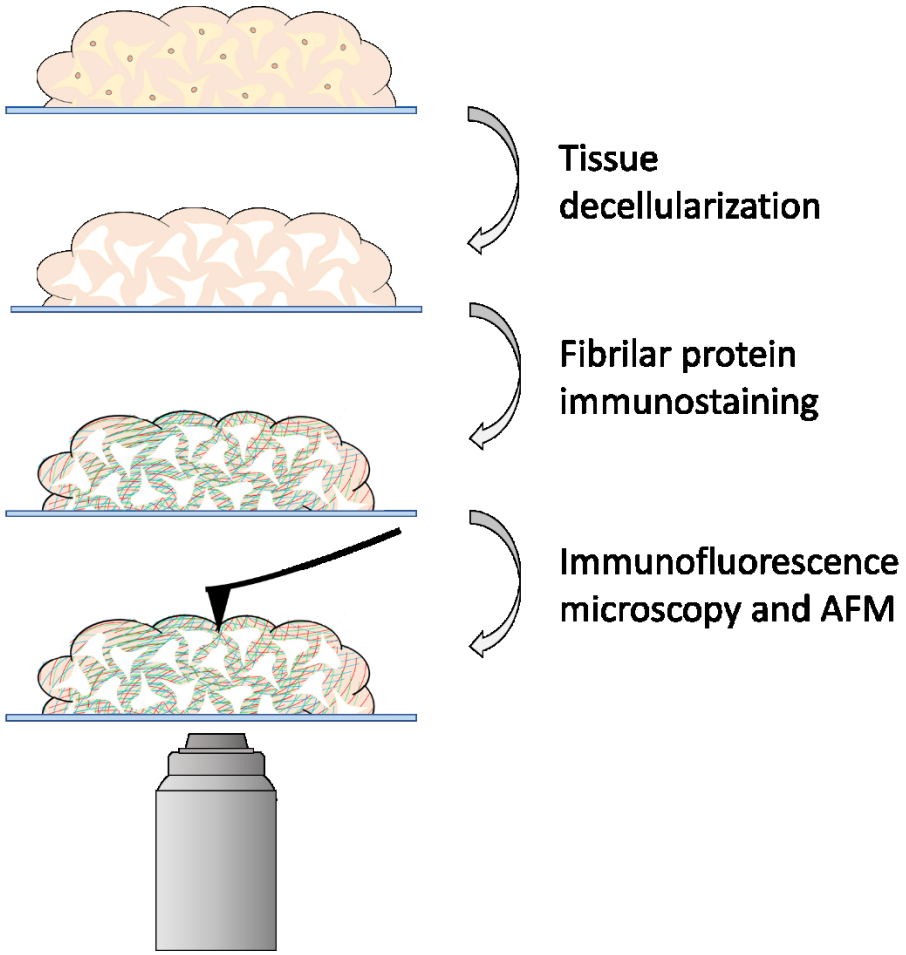

Figure 4.5 Set-up for the Fluorescence+AFM assay, it consists mainly in 4 steps. 1st, attachment of the sample to the glass. 2nd, decellularization of the tissue. 3rd, the immunostaining of the three main fibrillar proteins of the lung tissue. 4th, the observation of the microstructure changes in healthy and cancerous ECM and the AFM indentation assay on that same points.

A more detailed view of AFM-image correlation is shown in Figure 4.6. The immunofluorescence image for the Alexa 488, 405 and Cy3 (Collagen I, Elastin and Collagen III, respectively) and the stiffness map calculated

from the indentations are shown for a single experiment. Each indentation was done at the center of each quadrant of a 20*20 grid in the image. The figure shows a composite of the three proteins for a better visualization and comprehension. Each protein map was analyzed individually.

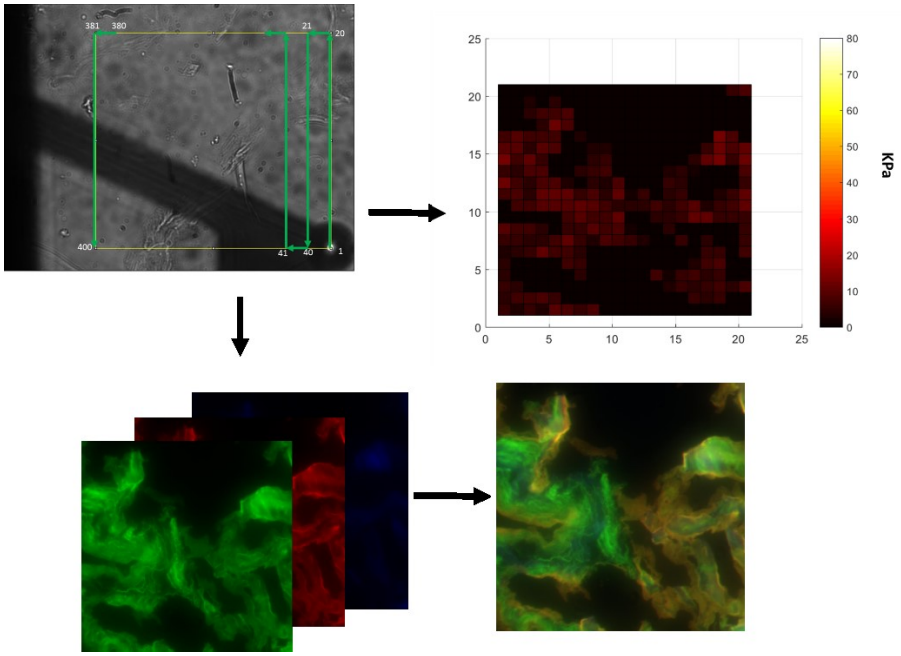

*Figure 4.6 Two types of acquisition maps obtained from the AFM+Immunofluorescence set-up. Top-left, the area traced for the 20*20 indentation spots of the AFM tip. Bottom-left, each channel for each fluorophore representing each fibrillar protein of the lung ECM. Top-right, stiffness map of the measured sample corresponding to the area of the bottom-right obtained immunofluorescence image,*

4.2.4.1 *AFM data processing*

The effective elastic modulus (E) of the ECM is calculated from the approaching phase of each force curve with data corresponding to a maximum penetration depth of 500 nm.

The sample is approximated as an isotropic and linear elastic solid, which occupies an infinitely extending half space. If the indenter is not deformable and there is no additional interaction between the indenter and the sample, the Young's modulus (E) of the sample can be calculated using the Hertz model. Traditional Hertz model is based on the shallow contact between two spherical bodies to approximate the Young's modulus of a sample, however extensions of the model have been made to include additional indenter geometries [20]. The recorded force-penetration curve is fitted using the following equation for spherical tips:

$$F = \frac{E}{1+\nu^2}\left[\frac{a^2+R^2}{2} ln \frac{R+a}{R-a}\right] - aR \qquad (1)$$

where F is the applied force, E is the effective elastic moduli, ν is Poisson´s coefficient, a is the contact radius and R is the tip radius.

The Hertz model assumes the sample to be an infinite half space, hence to avoid substrate effect the maximum penetration depth should be limited depending on the sample thickness. Finite Elements were used to study the volume of the sample affected by the indentation, The model consists of a 10 µm thick sample, with the bottom surface fixed, and a rigid sphere of 10 µm of diameter which is displaced vertically. The

problem simulated is axisymmetric and the sample has isotropic elastic properties (E=10 kPa, ν=0.3).

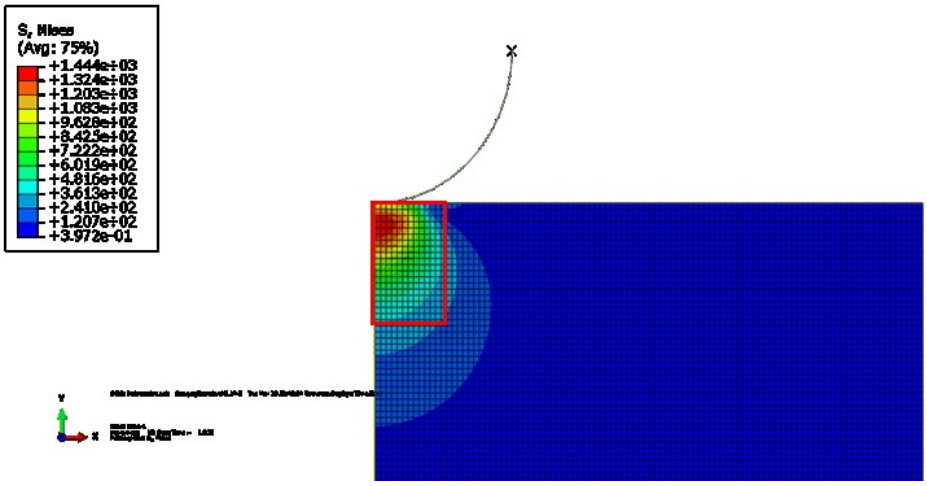

Figure 4.7 Distribution of the equivalent Von Mises Stresses when an indentation of a 10 µm diameter tip and a maximum penetration of 500 nm happens. The red box shows a cylindrical volume of radius 2,5 µm and a length of 4 µm in the frontier in which the stress falls down to the 25% of the maximum stresses as shown by the FEM model.

Figure 4.7 shows of the results of the FEM simulation. Considering that a relevant contribution in measuring the mechanical properties corresponds to an area which undergoes stresses over the 25% of maximum stress, then, our volume of interest can be approximated as a cylinder of 2.5 µm of radius and 4 µm of length surrounding the contact point between the tip and the sample. Therefore, as the ECM samples have a thickness of 7 µm, we will not have an effect of the substrate on the measurements.

4.2.5 Image processing

4.2.5.1 *Eliminating the crosstalk between the fluorophores*

One of the issues we had to overcome in this work was to avoid the crosstalk between the different fluorophores employed to dye the three different fibrillar proteins.

The crosstalk is the signal interference arising from emission overlap by two or more fluorophores.

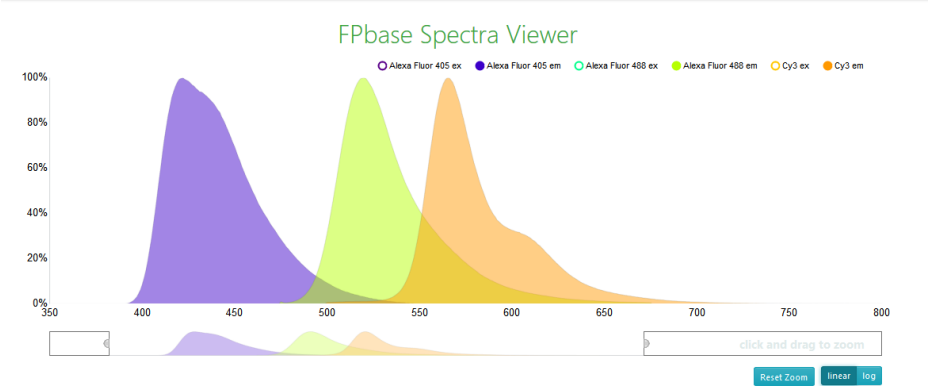

Figure 4.8 Example of the crosstalk between Alexa 405, Alexa 488 and Cy3 emission spectra. As can be seen, there is a crosstalk between the 405 and the 488 in the range from 475 to 550 nm, between the 488 and the cy 3 in the range from 550 to 650 nm and between the three of them in the range from 500 to 550 nm. Image taken from FPbase.org spectra viewer.

To overcome this issue, a linear unmixing algorithm was applied. The algorithm, developed by the Imaging group in CIMA, directed by Prof. Carlos Ortiz de Solorzano, can separate fluorescent probes that would otherwise have emission overlap based on the theoretic emission spectra of the fluorophores.

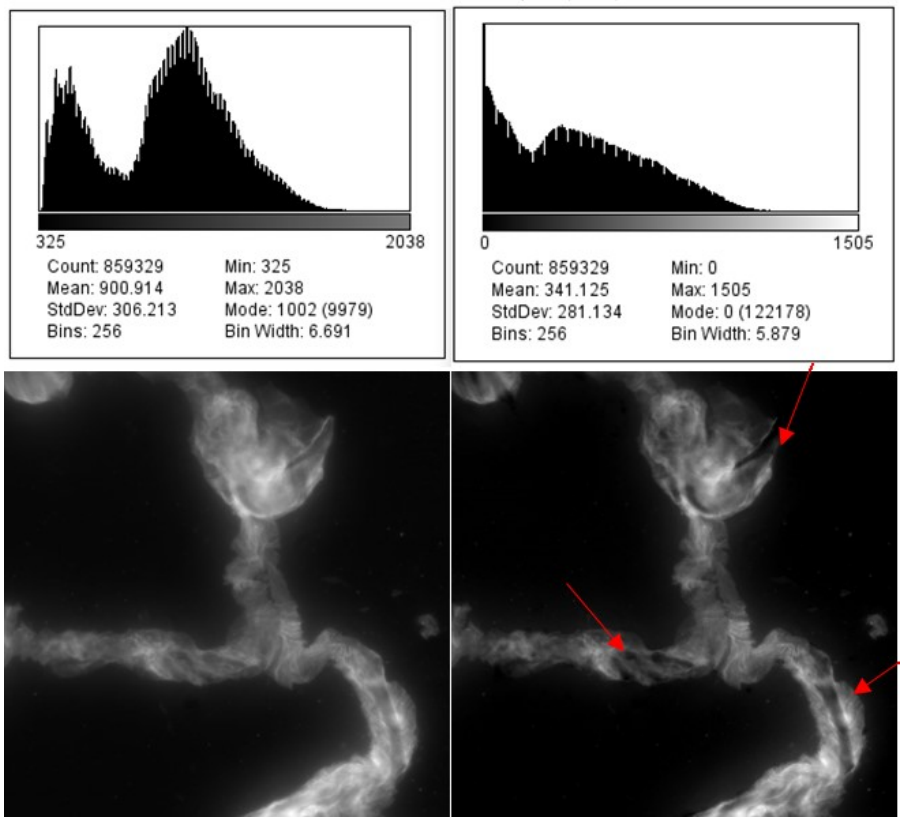

Figure 4.9 Differences between the original epifluorescence image for Collagen I (Alexa 488) in a lung ECM sample prior to unmixing (left), and after unmixing (right). The top histograms show the change on the intensity values before and after the unmixing, the fall in the intensity values corresponds to the part of the emission spectra of the other fluorophores that were crosstalking with the Alexa 488.

As it is shown, applying the linear unmixing algorithm results in removing the parts of the sum of the intensities that were not part of the Alexa 488, decreasing the intensity levels and leaving mostly those that belong to the Alexa 488, which represents the Collagen I. This is applied twice for each sample, in order to remove the other two fluorophores that could be introducing signal errors to the image due to the crosstalk.

Unmixing was applied to the three channels, Collagen I, Collagen III and Elastin, to all the images by the group of Prof. Ortiz de Solorzano.

4.2.5.2 *Segmentation of the immunofluorescence images*

Uneven illumination was corrected through a bleach correction procedure using a Gaussian blurring with σ = 120.

Three kind of structures were distinguished:

- The protein contained in the ECM (the fluorescence signal on each channel)
- All the protein (the fluorescence signal of all the channels)
- The fibrillar structures of each protein.

Hence, three kind of binary masks were calculated. The mask providing information about the protein was obtained by applying a median filter with a kernel-size of 5, followed by a linear stretching of the intensity values and using a hysteresis thresholding, whose parameters are the first and the second level of an Otsu multi-threshold. The tissue segmentation resulted from the union of the masks of the three different proteins. The latter were also used to remove the background in the original channels and hence, avoid the extraction of debris in the segmentation of fibrillar structures. Finally, the fibers were obtained through the following workflow: (1) a linear stretching of the intensity values, (2) a median filter with a kernel of size 3 if the images were of collagen type I or III, (3) fiber enhancement based on Frangi's vesselness filtering (Fiji's implementation) [21] with σ = 2 for collagen type I and III and σ = 7 for elastin fibers respectively, and (4) binarization using hysteresis thresholding with l and h being the lower and higher thresholds respectively. l is the second level and h is the midpoint between the second and the third level of an Otsu multi-threshold. The

entire image processing was performed in Matlab and Matlab-ImageJ connection using the plugin MIJ.

The threshold and the binary masks were obtained by Dr. Arrate Muñoz and collaborators from the Biomedical Imaging and Instrumentation group in Universidad Carlos III.

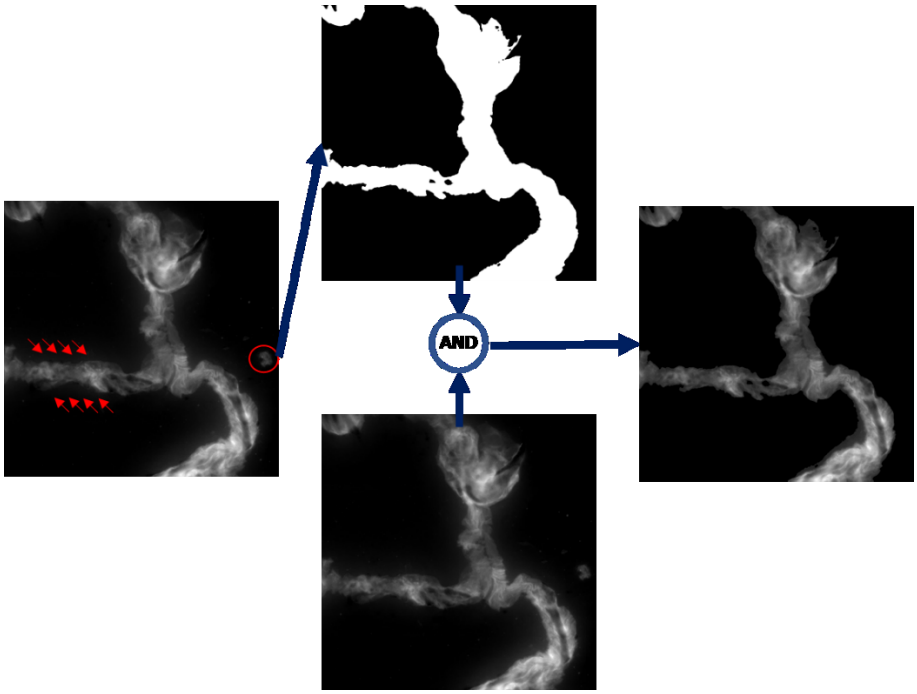

Figure 4.10 Simplified process of the application of a binary mask to the unmixed image. Left, the unmixed image where the crosstalk between the fluorophores has been diminished. Top, The binary mask created by thresholding the unmixed image. Bottom, the unmixed image Right, the resulting image after the binary mask is applied.

The obtained image, which shows just one of the proteins is then divided in a 20x20 grid. The center of each quadrant is the area where an indentation was made, as 20x20 indentations were performed per image as will be explained in detail later,

To calculate a relative volume fraction of the protein in the ECM the next equation is used:

$$Vf = \frac{\sum ICollI}{NpECM*(ImaxColI+ImaxColIII+ImaxElastin)} \quad (2)$$

Where V_f is the volume fraction of the calculated protein, the IColI is each of the intensities of ColI protein in that quadrant, ImaxColI, ImaxColIII and ImaxElastin are the maximum intensity measured for CollagenI, CollagenIII and Elastin and NpECM is the number of pixels where there is at least one of the three proteins is found.

This means that the volume fraction of a protein is calculated as the sum of all the intensities for that protein in a certain quadrant, divided by the sum of the maximum intensity shown by each protein in all the samples by the number of pixels illuminated by any protein in that same quadrant Figure 4.11.

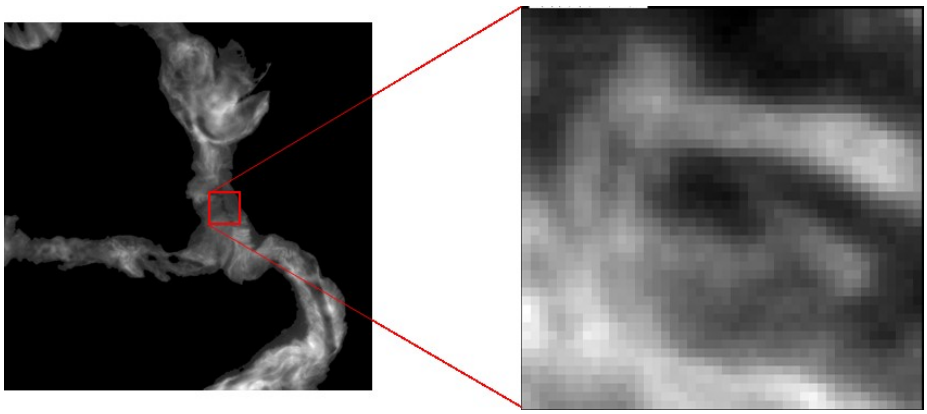

Figure 4.11 Example of one of the resultant quadrants after applying the binary mask. The summed intensities of collagen I for the quadrant marked in red is 2473142. Left picture size. 100 µm x100 µm.

4.3 RESULTS

4.3.1 The Elastic Modulus of Lung ECM

Young's modulus (E) of the non-cancerous ECM and cancerous ECM was obtained from the samples of 7 patients. For the non-cancerous part of the ECM the averages of the E for the 400 indentations for each patient oscillates from a minimum of 4.39 ± 1.81 kPa to a maximum of 7.98 ± 3.22 kPa. For the cancerous part, the softer ECM present within the 7 patients has an average E=7.85 ± 4.91 kPa and the stiffer cancerous ECM presents an average E=20.01±10.13 kPa. These results are gathered in Figure 4.12. Each patients' cancerous and non-cancerous E values were paired and

the mean differences of the mechanical parameters between regions were analyzed using one-way analysis of variance (ANOVA). All the cases showed $p < 0.05$..

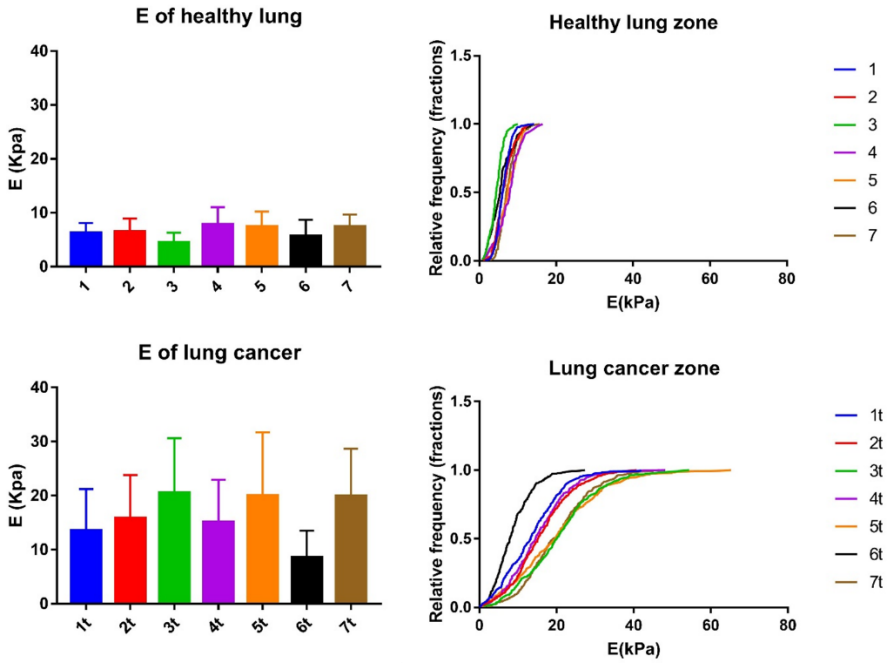

Figure 4.12 Differences between the measured E between the non-cancerous (top) and cancerous (bottom) lung ECM. Each number and color correspond to the samples of healthy and non-healthy tissue of the same patient. Left, means of the E of each patient for healthy and cancerous ECM. Right, cumulative distribution of the E for each sample in healthy and cancerous lung ECM.

Figure 4.12 shows also the cumulative density functions of the elastic modulus for cancerous and healthy ECM for each patient. It is clear that the cancerous regions are stiffer and exhibit a higher variability. As an example, Figure 4.13 represents the probability density distribution of the cancerous and non-cancerous region for a patient. Again, it is clear that cancerous ECM shows a much higher heterogeneity, the non-cancerous

ECM samples showed a mean coefficient of variation of 38.61% and the cancerous ECM samples showed a mean coefficient of variation of 52.68%. For this patient, in the case of healthy ECM, E ranges from 1.82 to 13.53 kPa while the values of E of the cancerous region range from 0.23 to 65.17 kPa. Both distributions fit a Gaussian distribution of median 7.40 kPa with standard deviation of 2.74 kPa for the non-cancerous ECM and a median of 19.63 kPa with a standard deviation of 11.70 kPa for the cancerous ECM.

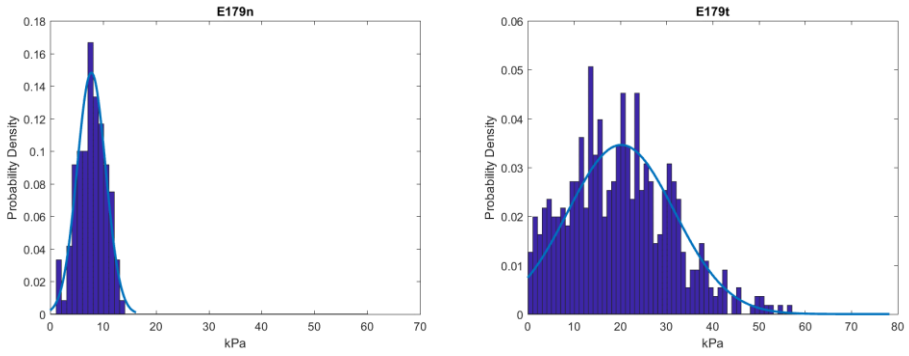

Figure 4.13 Example of the Probability Density distribution of a non-cancerous ECM (left) and cancerous ECM (right) elastic modulus of the same patient.

If we consider all the cancerous and non-cancerous regions together, independently of the patient, we obtain an elastic modulus of 6.44 ±2.52 kPa for healthy lung ECM and an elastic modulus of 16.37±9.62 kPa for cancerous lung ECM. These results are shown in Figure 4.14.

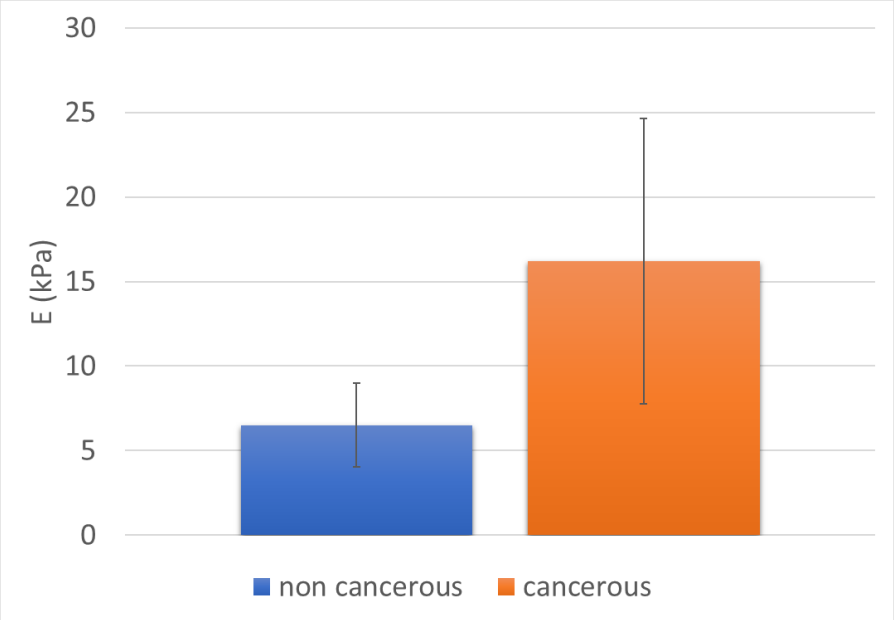

Figure 4.14 Mean values of the measured elastic modulus of all the tumoral and non-tumoral samples.

Since a pathologist marked the cancerous zones and the healthy zones prior to the AFM indentation experiments, we have worked with two separate sets of data per patient. However, when indentation is used to diagnose cancer [22] an enormous amount of indentations are performed in order to detect tumors. Therefore, it was decided to merge all the AFM measurements of both cancerous and non-cancerous zones of the ECM for each sample .and to extract the properties of each region from these data. To do so, the distribution obtained will be fitted as a bimodal distribution. The first peak should be close to the median of the non-cancerous ECM stiffness distribution and a second peak close to the median of the cancerous ECM stiffness distribution.

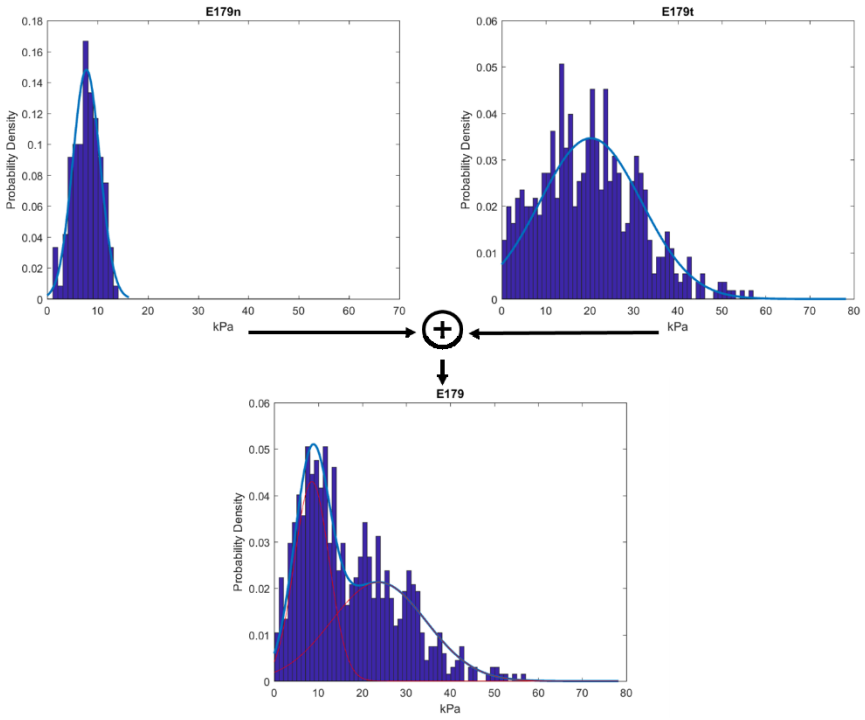

Figure 4.15 Approach of the bimodal distribution when adding the measurements of the cancerous and non/cancerous zone. The red curves in the bottom image show each of the non-cancerous and cancerous distribution estimated by the bimodal distribution.

Figure 4.15 shows an example for the stiffness distribution of healthy, tumoral and combined regions. While the non-cancerous and cancerous ECM peaks show a median stiffness of 7.4 kPa with a standard deviation of 2.74 kPa and 19.63 kPa with a standard deviation of 11.7 kPa respectively when analyzed separately, when the two samples are treated as a bimodal distribution, the peaks show a median stiffness of 8.55 ±3.94 kPa and 23.75 ± 10.76 kPa for the non-cancerous and cancerous ECM stiffness respectively. The error between the separately calculated medians and the medians obtained from the peaks of the bimodal distribution are 13.51% and 17.36% for the non-cancerous and

cancerous peaks. In both cases, the median elastic modulus is overestimated when derived from the bimodal distribution. Figure 4.16 shows an example of the whole process for another patient. Again, the average values are overestimated when calculated from the aggregated data using a bimodal, but in this case the dispersion obtained for the cancerous region is slightly reduced. The results for all the samples can be found in Table 4.1 confirming the trends described.

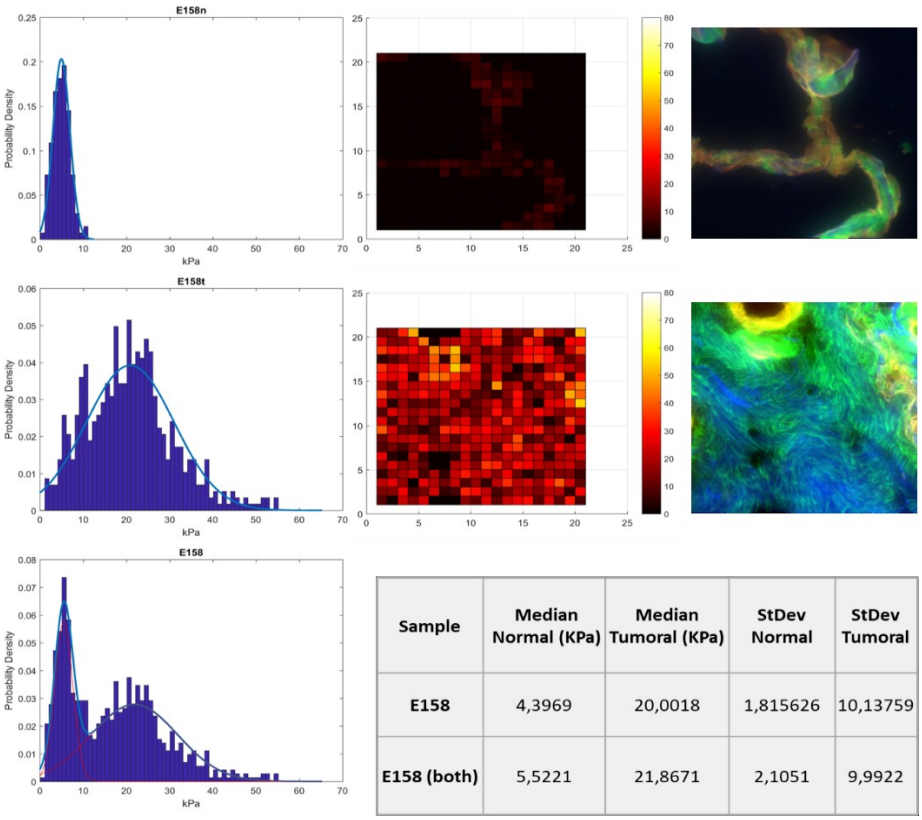

Sample	Median Normal (KPa)	Median Tumoral (KPa)	StDev Normal	StDev Tumoral
E158	4,3969	20,0018	1,815626	10,13759
E158 (both)	5,5221	21,8671	2,1051	9,9922

*Figure 4.16 Summary of the results of the measured Young Modulus on a sample. Columns, from left to right, distribution of the measured stiffness. In the middle, stiffness maps showing the measured area of the sample (400 indentations in a 20*20 grid in a 100*100 µm area, the black squares show the zones where de substrate was indented), and an immunofluorescence map showing the tissue for comparison. From top to bottom, Non-cancerous tissue, cancerous tissue and the sum of both samples fitted to a bimodal distribution. The table represents the values of the measured cancerous and non-cancerous Young modulus for the sample and where the peaks appear on the bimodal distribution of the aggregated data.*

Table 4.1 the differences between the real distribution of the Young's modulus values in the measured samples of lung non-cancerous tissue and cancerous tissue and the estimation made by the bimodal distribution approach.

Sample	M Normal (KPa)	M tumoral (KPa)	M First Peak	M Second Peak	Error Normal	Error Tumoral	Alfa
1	6.03 ± 1.89	13.31 ± 7.72	6.78 ± 2.10	15.15 ± 7.23	11.12%	12.13%	**0.6752**
2	6.09 ± 2.42	15.13 ± 7.96	7.61 ± 3.00	18.06 ± 7.66	19.89%	16.21%	**0.5723**
3	4.4 ± 1.81	20.01 ± 10.14	5.52 ± 2.11	21.87 ± 9.99	20.38%	8.53%	**0.3046**
4	7.98 ± 3.23	14.53 ± 7.82	9.07 ± 3.86	17.36 ± 7.30	12.00%	16.28%	**0.445**
5	7.40 ± 2.75	19.63 ± 11.71	8.55 ± 3.94	23.76 ± 10.77	13.51%	17.36%	**0.4253**
6	5.45 ± 2.96	7.85 ± 4.91	5.93 ± 2.55	11.77 ± 4.75	8.11%	33.32%	**0.6143**
7	7.023 ± 2.27	19.13 ± 8.71	8.05 ± 2.37	21.09 ± 8.40	12.92%	9.31%	**0.4507**

4.3.2 Structural composition differences between the non-cancerous and cancerous lung Extracellular Matrix

Differences between the mean intensity of the non-cancerous and cancerous samples of the same patient for each fibrillar protein were measured from the processed images.

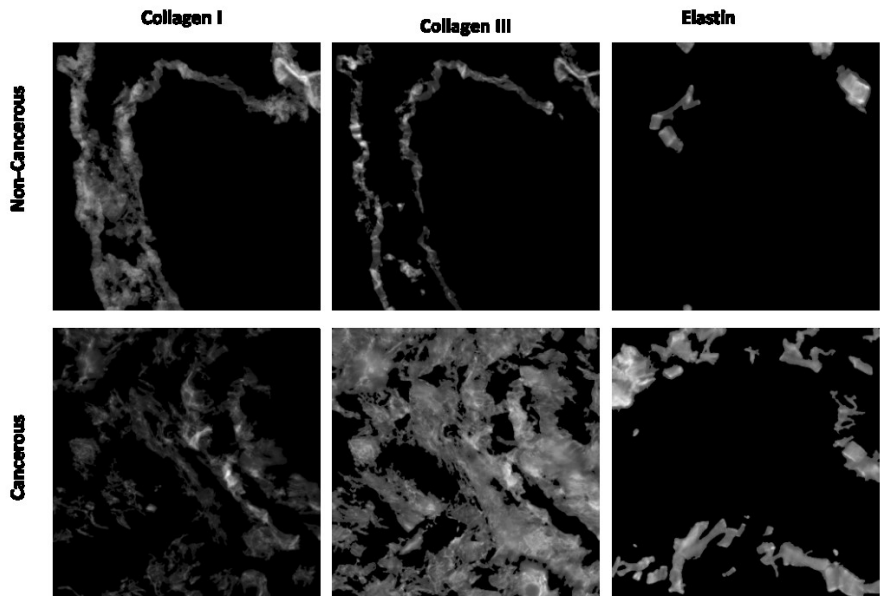

Figure 4.17 Comparison between the Non-Cancerous and Cancerous ECM in the same lung cancer patient.

For Collagen I most of the samples showed an increase in the mean intensity of the acquired image. In 4 of them show an increase and 3 of them show an increase in the mean intensity of the cancerous ECM of two times the mean intensity of the non-cancerous ECM. One of the samples did not show any relevant change of the mean intensity when comparing both cancerous and non-cancerous ECM, and two of them showed a mean intensity drop. From these last two, one of them already

showed this drop before any of the unmixing and binary mask processing.

For the Collagen III, in non-cancerous ECM all the samples show same amounts of mean intensity when comparing between samples. For the cancerous ECM there is not an evident trend respect the non-cancerous ECM.

For the Elastin, there is a high variability in the mean intensity of each sample independent of the source. In non-cancerous ECM the mean intensity can be up to 4 times higher from one sample to another, the same effect can be observed in the cancerous ECM.

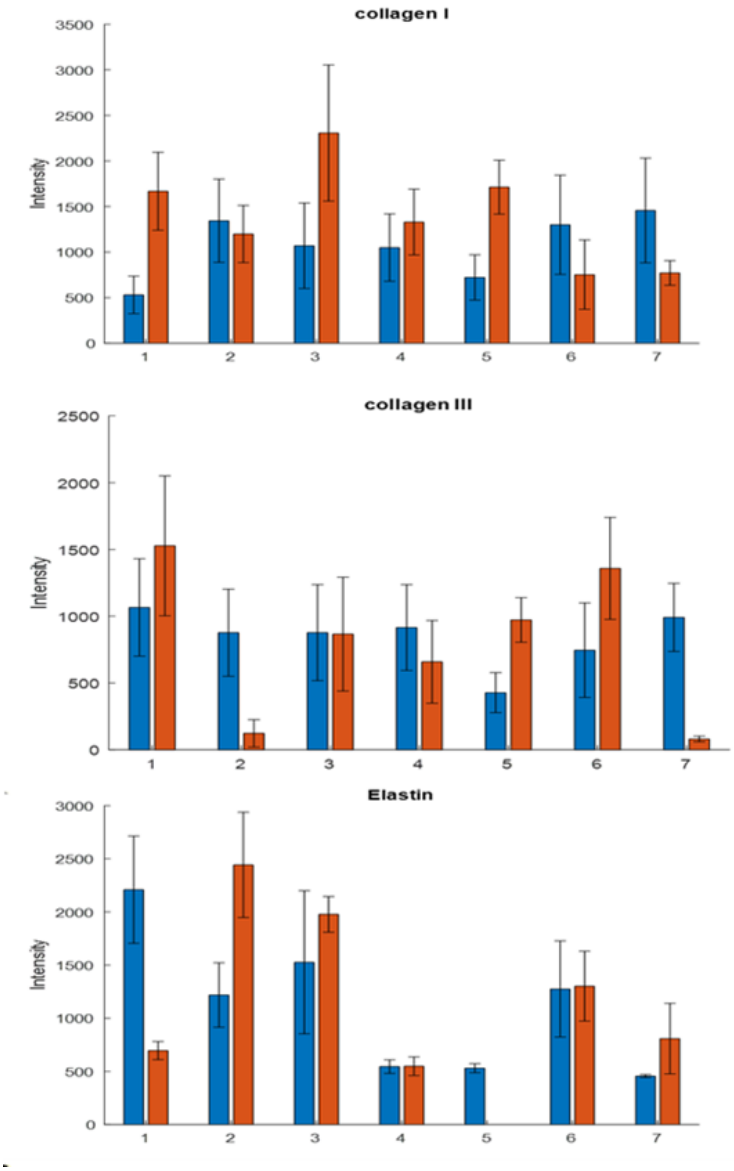

Figure 4.18 Mean intensity of the images taken from non-cancerous (blue) and cancerous (orange) ECM for each patient. From top to bottom, Collagen I, Collagen III and Elastin.

The volume fraction of the three main fibrillar proteins was then calculated following the previous equation (2). Figure 4.19 shows the results for each protein on each sample. The mean collagen I volume fraction showed a mean 1.7-fold and up to a maximum 3.48-fold increase from non-cancerous to cancerous ECM samples. Collagen III and elastin mean volume fraction showed a 1.18-fold increase and 1.08-fold increase respectively.

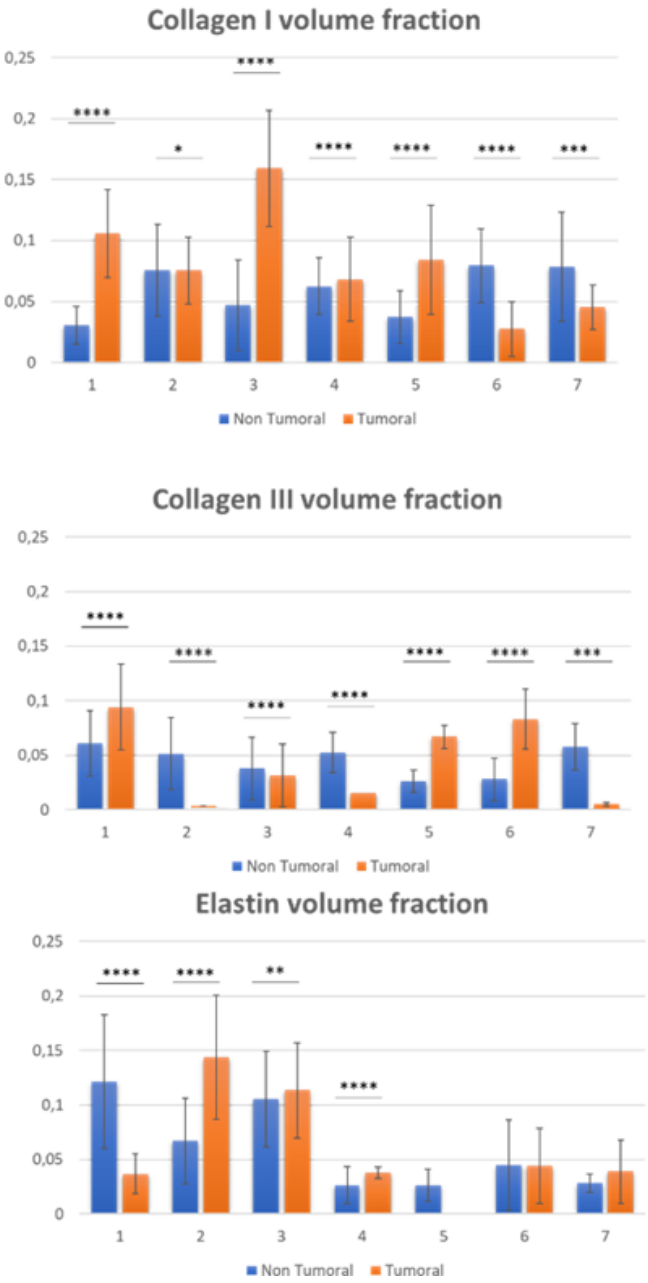

Figure 4.19 Volume fraction mean and standard deviation for each sample for all three fibrillar proteins, collagen I, collagen III and elastin.

4.3.3 Matching the mechanical properties of the lung cancer ECM with its structural composition

First, the correlation between the measured Young's modulus and the volume fraction of each fibrillar protein on each quadrant of the picture (each quadrant representing one AFM indentation) was plotted.

Figure 4.21 shows the result of each scatter plot between Collagen I, Collagen III, Elastin and the sum of the three proteins' volume fraction plotted against Young's modulus for each quadrant for a Non-Cancerous sample. Pearson's correlation coefficient (ρ) showed for the Non-cancerous sample and the Collagen I, the coefficient ρ=0.42, for the Collagen III ρ=0.3 and for the Elastin ρ=0.0058. Meaning that the two collagens seem to follow an increment of the Young's modulus when the volume fraction of that protein increases, according to the Critical values of Pearson's correlation coefficient that must be exceeded to be considered significantly nonzero at the 0.05 level shown in Figure 4.20.

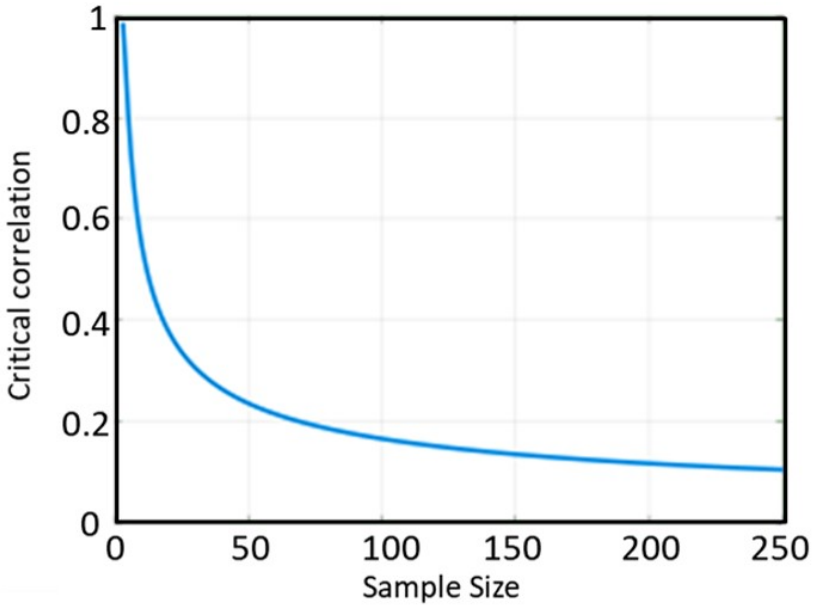

Sample	Collagen I	Collagen III	Elastin	ECM
1	0.427	0.295	0.005	0.259
1t	0.367	0.325	0.102	0.375
2	0.591	-0.09	0.416	0.540
2t	0.183	-0.09	0.106	0.094
3	0.349	-0.05	0.442	0.451
3t	0.330	0.156	-0.03	0.251
4	0.449	0.315	0.247	0.495
4t	0.126	0.043	-0.05	0.073
5	0.414	0.301	0.259	0.414
5t	0.273	-0.03		0.292
6	0.680	0.346	-0.13	0.580
6t	0.459	0.386	-0.05	0.459
7	0.726	-0.07	0.346	0.688
7t	0.312	-0.23	0.232	0.276

Figure 4.20 Top, Critical values of Pearson's correlation coefficient that must be exceeded to be considered significantly nonzero at the 0.05 level. Bottom, summary of the Pearson's correlation coefficient obtained for each protein on each sample. The names of the samples are shown with an "n" for non-cancerous sample and "t" for the cancerous sample.

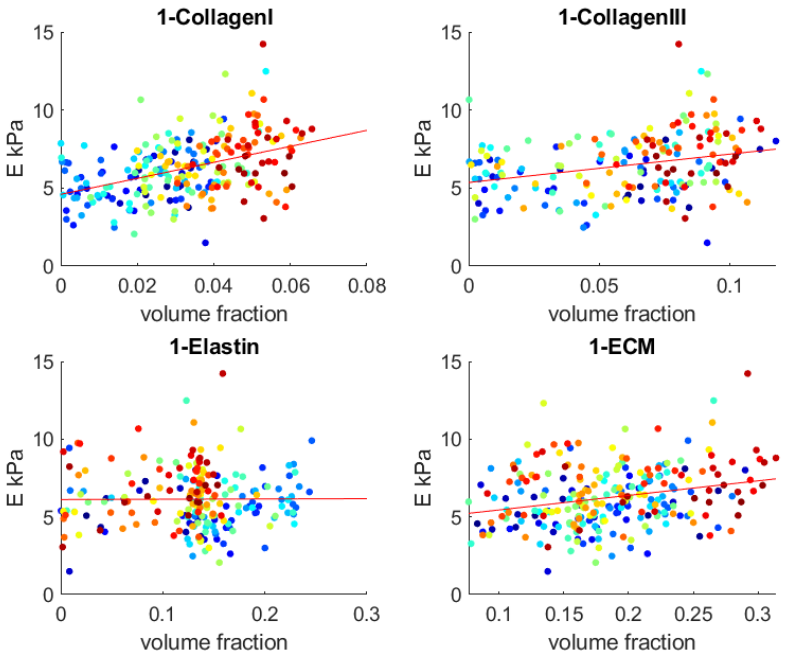

Figure 4.21 Example of a scatterplot between the volume fraction of each fibrillar protein and the Young's modulus measured in each quadrant of an image for a non-cancerous sample. The last of the scatterplots shows the sum of the three proteins, Sample 1

For the cancerous counter part of the same sample, results are shown in Figure 4.22. The Pearson's coefficients for each protein against the measured young modulus on each quadrant are ρ= 0.367 for the Collagen I, ρ=0.325 for the Collagen III and ρ=0.102 for the Elastin. As happened to the non-cancerous tissue, the two collagens seem to follow an increment of the Young's modulus when the volume fraction of that protein increases although this trend seems to be lower for the collagen I in cancerous ECM than it is in non-cancerous ECM for the same patient.

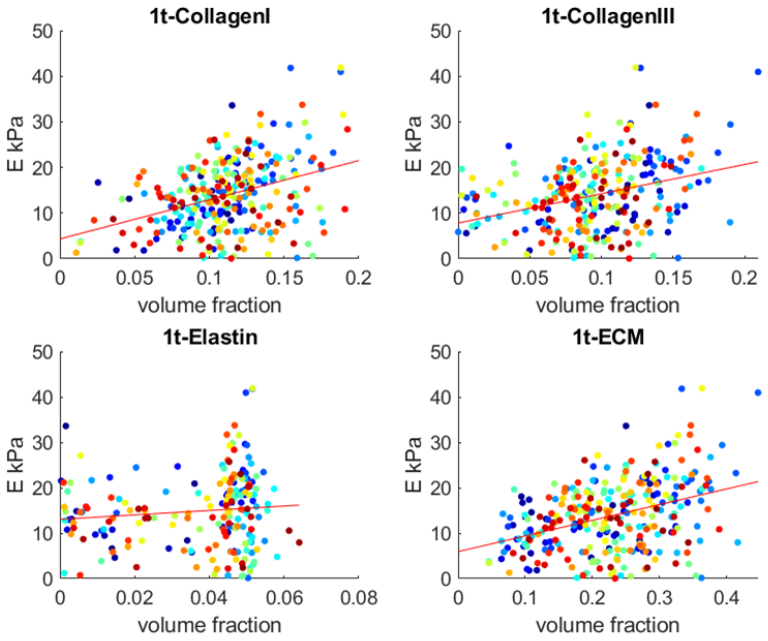

Figure 4.22 Example of a scatterplot between the volume fraction of each fibrillar protein and the Young's modulus measured in each quadrant of an image for a cancerous sample. The last of the scatterplots shows the sum of the three proteins, Sample 1

All the results for all the samples are gathered in the table shown at the bottom of Figure 4.20. As can be observed, most of the values except two of the cancerous samples match the criteria of the Pearson's correlation coefficients for a sample number higher than 100 for the Collagen I. All the samples, nevertheless, show a higher ρ in non-cancerous ECM than in cancerous ECM for the same patient.

Next, we observed if there is any relationship between the mean volume fraction and the mean Young's modulus of each sample and compared all the samples to see if there was any trend. The correlation between the mean volume fraction of each sample and the mean measured E of each

sample is show in Figure 4.23. The correlation of the Collagen I gave a result of R^2=0.2704 being this the highest correlation value, the Collagen III and Elastin showed R^2=0.0638 and R^2=0.0227 respectively.

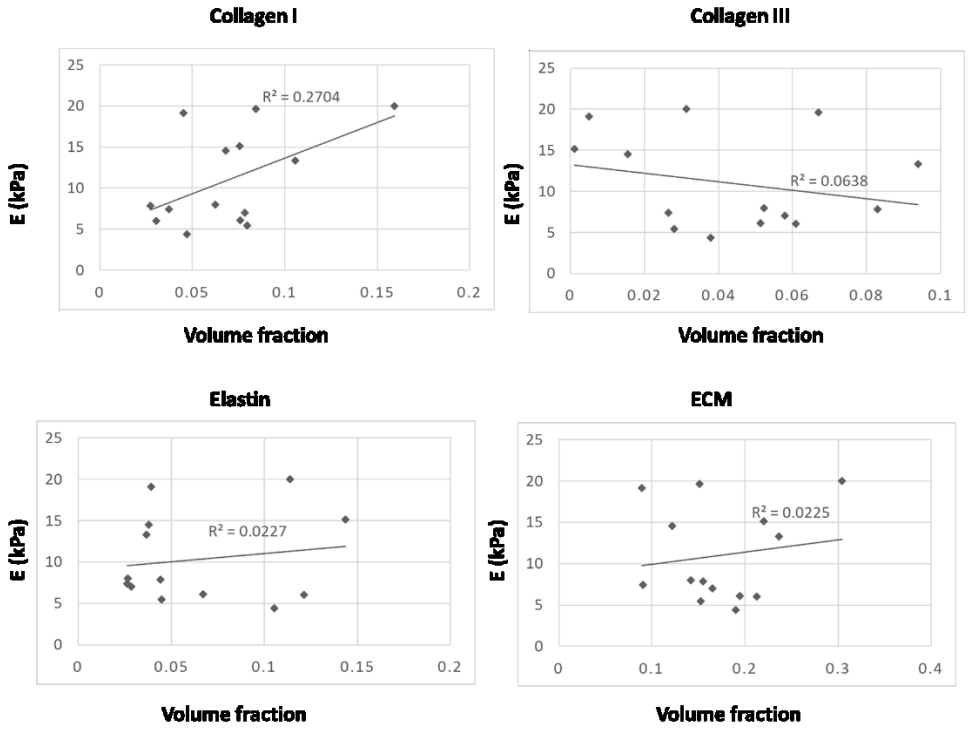

Figure 4.23 Correlation between the mean volume fraction of Collagen I, Collagen III and Elastin and the sum of the three volume fractions with the mean measured E for all the cancerous and non-cancerous samples.

4.4 DISCUSSION

4.4.1 Measuring the Elastic Modulus of Lung ECM

The results of the AFM measurements of the Young's modulus of the samples taken from patients with lung cancer show a distinct value on cancerous ECM and non-cancerous ECM. Cancerous ECM of a same patient can show up to 5 times higher Young's modulus from 4 kPa in non-Cancerous ECM to 20kPa in cancerous ECM, the mean E is increased 2.5 folds from the non-cancerous to the cancerous ECM. This increase of the elastic modulus of the Cancerous ECM has been observed previously in different types of cancer, from breast cancer [22] to prostate cancer [11] going through, thyroid, bladder and kidney cancer [23].

The cancerous ECM shows much more heterogeneity in the AFM measurements than the non-cancerous ECM does, with values ranging from 0.2 kPa to 65 kPa for a same sample. The standard deviation of the measured Young's modulus of the non-cancerous ECM samples range between 1 and 3 kPa and the one for the cancerous ECM can go up to 11.7 kPa . The mean value of the Young's modulus of the cancerous ECM is 2.5 times higher than the one of the non-cancerous tissue, 15.65±4.04 kPa and 6.33 ±1.13 kPa respectively. The non-cancerous ECM samples showed a mean coefficient of variation of 38.61% and the cancerous ECM samples showed a mean coefficient of variation of 52.68%. This happens in other tumors such as breast cancer, especially in aggressive ones. The stiffness of the ECM is correlated with disease progression and poor prognosis [24].

The resulting Young's modulus from both cancerous and non-cancerous ECMs seem to have differentiated stiffness peaks on their respective stiffness distributions for each patient. Other works, such as Plodinec et al. [22], show that in breast cancer. In this work, the tissue was not decellularized. The first peak in the distribution was assigned to a less stiff breast cancer cells than normal cells and the second peak to the cancerous ECM. We plotted together the data obtained for lung cancer for each patient, as if we had obtained the measurements from a unique indentation map performed on a region in the limit between the cancerous and non-cancerous ECM , In our case, the ECM was decellularized to avoid any mechanical measurement not related with the ECM. As we have observed, the distribution shown behaves like a bimodal distribution with two characteristic peaks. The softer peak represents the non-cancerous part of the ECM and the stiffer peak represents the cancerous ECM. When comparing the average of the peaks with the average of each distribution separately, we observe that the peaks in the bimodal distribution have overestimated the Young's modulus average for each ECM type. This is because the tissue area in non-cancerous samples is lower than the tissue area in cancerous samples, resulting in a lower number of indentations. Since the stiffness of the cancerous ECM is more heterogeneous than the non-cancerous ECM, some of the measured values fall into the non-cancerous stiffness distribution, increasing the average of the non-cancerous distribution. For the same reason, the average of the cancerous ECM stiffness distribution increases, due to the loss of those values of lesser stiffness. However, even if the Young's modulus of both tissues is being overestimated, the two peaks appear to be clearly differentiated.

4.4.2 Structural composition differences between the non-cancerous and cancerous lung ECM

The main discussion about the differences between the cancerous and non-cancerous lung ECM composition is going to focus in the main differences between the Collagen in both cases, since an increase in Collagen I is a characteristic of an increase on cancer risk [25]. A higher collagen density promotes fast and persistent migration and can induce epithelial-to-mesenchymal transitions in metastatic tumors [25]. The mean values of the intensities measured in the image for Collagen I show an increment of the intensity when comparing the non-cancerous ECM with the cancerous ECM in most of the patients.

The composition of collagen I on cancerous lung ECM showed a volume fraction increase from 1.7 up to 3.48 folds the volume fraction found in non-cancerous ECM. Collagen III and Elastin also showed and overall presence increase in cancerous lung ECM even though this tendency was not found in all the samples.

To reduce variability between the different immunostained samples the next protocol was followed. Samples 6 and 7 showed a lower collagen I volume fraction for the non-cancerous ECM than for the cancerous ECM. When observing these images, Figure 4.24, we can see a much more dense tissue in the right image, the one representing the Collagen I in the cancerous ECM, but the intensity values of this sample are lower than the respective non-cancerous sample.

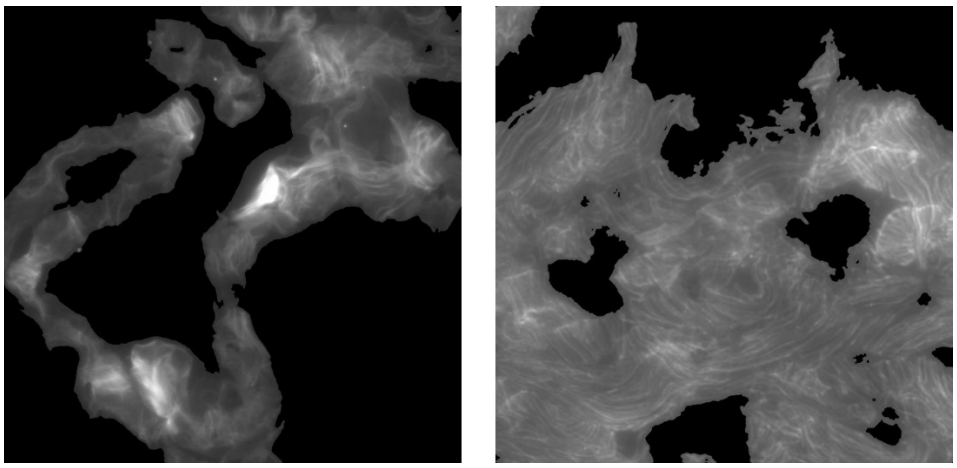

Figure 4.24 Sample n=7, left non-cancerous Collagen I, right cancerous collagen I.

In order to minimize the possible variability coming from the immunofluorescence between patients, a new equation for calculating the volume fraction of the proteins V_f in each quadrant of the image was proposed (3).

$$Vf = \frac{\sum IColI}{NpECM*(ImaxrColI+ImaxrColIII+ImaxrElastin)} \quad (3)$$

Where the IColI is each of the intensities of ColI protein in that quadrant, ImaxrColI, ImaxrColIII and ImaxrElastin are the maximum relative intensities measured for CollagenI, CollagenIII and Elastin on each measured sample (each image) respectively and NpECM is the number of pixels in each quadrant where at least one of the three proteins is found.

This means that the volume fraction of a protein is calculated as the sum of all the intensities for that protein in a certain quadrant, divided by the

sum of the maximum intensity shown by each protein in the whole image multiplied by the number of pixels illuminated by any protein in that same quadrant.

The difference between these two equations (2) and (3) is that one of them has into account the maximum intensity measured in all the samples (2), and the other, has into account the maximum intensity measured on that sample (3). A sample being each of the regions tested per patient.

The volume fraction of the three main fibrillar proteins was then calculated following the previous equation (3). Figure 4.25 shows the mean results for each protein on each sample. The mean collagen I volume fraction showed a 1.5-fold and up to 3.74-fold increase from non-cancerous to cancerous ECM samples. Collagen III and elastin mean volume fraction showed a 1.18-fold increase and 0.97-fold decrease respectively. Even though the mean increased in Collagen III, the measurements showed different volume fractions increases and decreases depending on the patient.

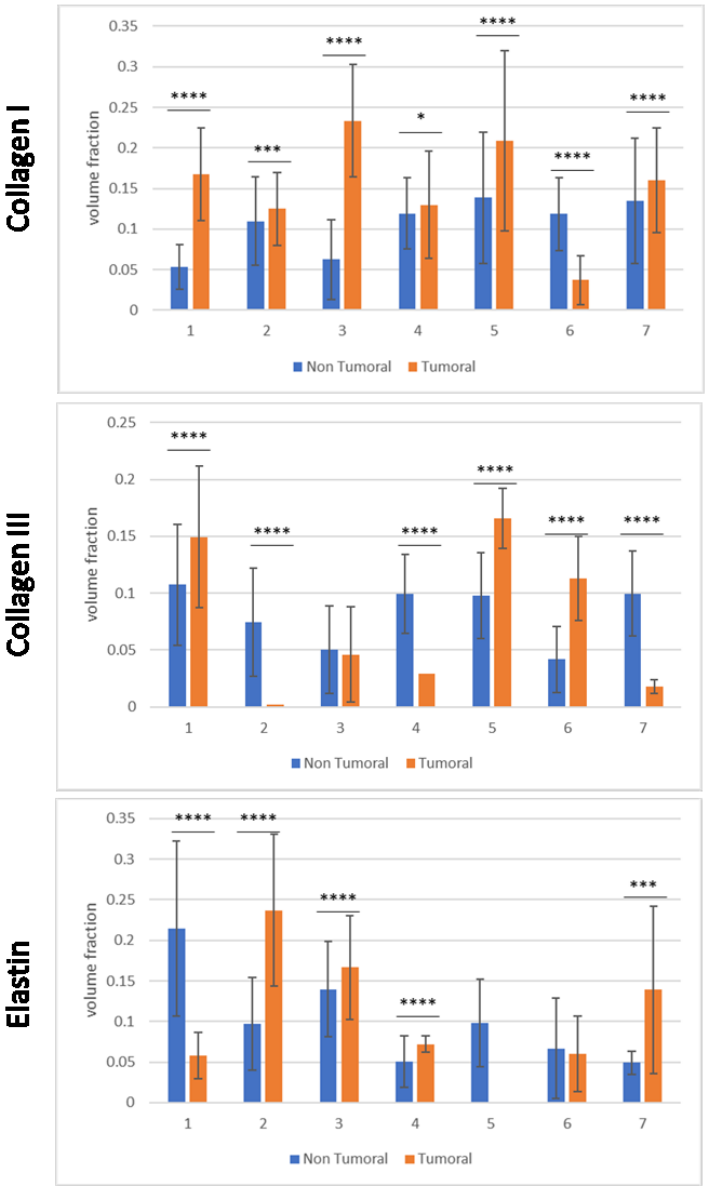

Figure 4.25 Volume fraction mean and standard deviation for each sample for all three fibrillar proteins, collagen I, collagen III and elastin.

As can be observed, the overall volume fraction increased since the maximum values are relatives to the sample. This fixes the problem with cancerous sample 7 and justifies the differences we saw in the images of Figure 4.24. Since the immunostaining protocol was the same for all the samples and was made at the same time for all of them, it is hard to explain why the intensity of the cancerous matrix has a lower value in sample 7. The tendency in sample 6 did not change, but this sample also is the one that has a lower elastic modulus increase between the non-cancerous and cancerous ECM.

4.4.3 Matching the mechanical properties of the lung cancer ECM with its structural composition

The correlation between the measured Young's modulus and the volume fraction of each fibrillar protein on each quadrant of the picture (each quadrant representing one AFM indentation) was calculated .The results show a positive correlation with the increment of the Collagen I and the measured Young's modulus on every non-cancerous ECM sample following the Pearson's correlation coefficient criteria. The trend seems to be inferior in the cancerous ECM samples. This could be explained not with the Collagen I quantity but with the structure. It is proven that Collagen in cancerous ECM show a higher grade of crosslinking that the one in non-cancerous ECM, this is due to the higher levels of Lysil Oxidase (LOX), family of oxidases which contains a group of extracellular copper-dependent enzymes that catalyze the cross-linking of collagen [26]. Lysil Oxidase was not measured in this work so we cannot know if this Collagen quantity is crosslinked or not.

After, the relationship between the mean measured Young's modulus and the mean volume fraction of each protein was compared between all the samples, an example of one patient is shown in Figure 4.21 and Figure 4.22. For the Collagen I, the data does not show any correlation although the elastic modulus seems to increase with the volume fraction.

Even though each sample showed a positive correlation between the collagen I volume fraction and the measured elastic modulus, Figure 4.20, the mean elastic modulus and the mean volume fraction of collagen I showed a small correlation , R^2=0.2704 Figure 4.23.

Since it has been seen that using equation (3) to calculate the volume fraction instead of equation (2) could improve the volume fraction ratios, it was decided to calculate the correlation between the volume fraction and the measured Elastic modulus.

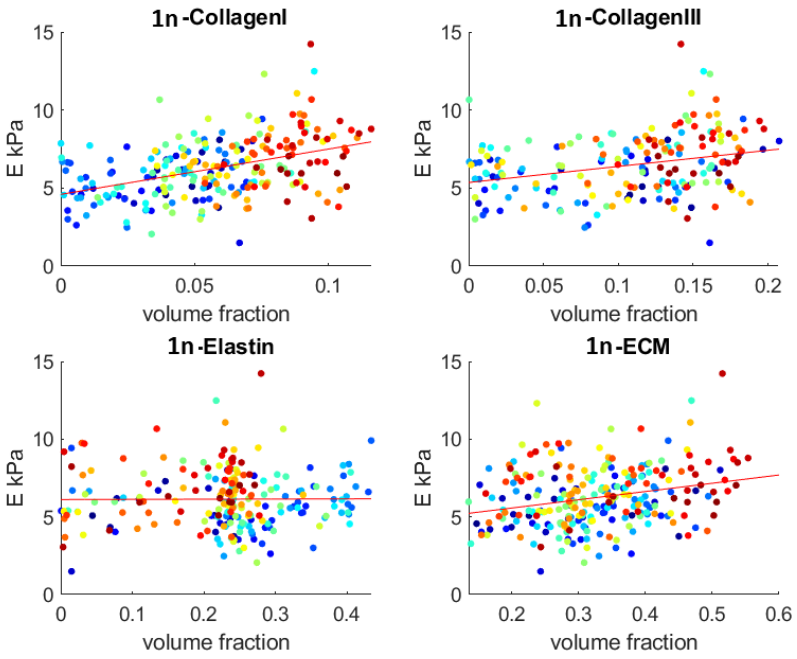

Figure 4.26 Example of a scatterplot between the volume fraction of each fibrillar protein and the Young's modulus measured in each quadrant of an image for a non-cancerous sample. The last of the scatterplots shows the sum of the three proteins,

Since the correlation values were calculated for each sample, the results were the same even though the volume fraction values were higher when calculated using equation (3). Figure 4.26 and Figure 4.27 show the correlation between the volume fraction and the measured elastic modulus for each quadrant in a sample for the non-cancerous region and cancerous regions respectively. Since the results were the same they are already gathered in Figure 4.20.

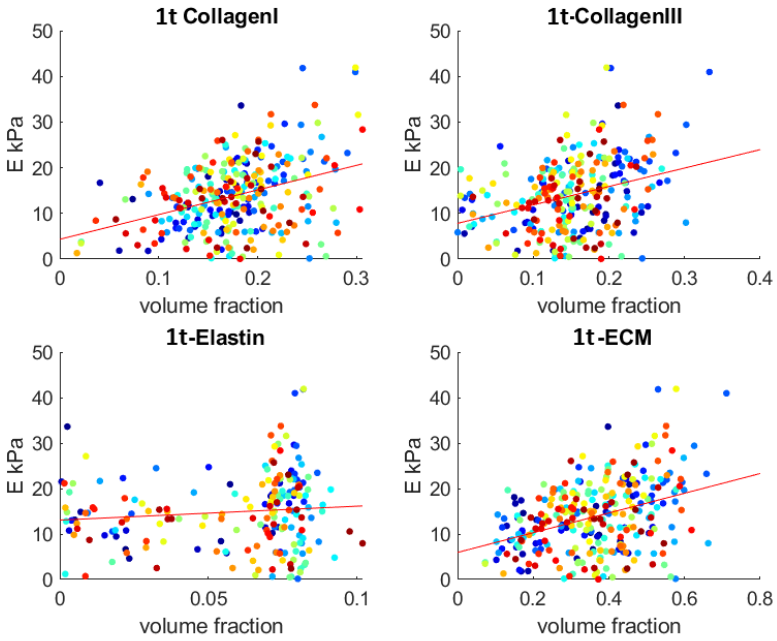

Figure 4.27 Example of a scatterplot between the volume fraction of each fibrillar protein and the Young's modulus measured in each quadrant of an image for a cancerous sample. The last of the scatterplots shows the sum of the three proteins,

The main change appeared when comparing the correlation of the mean volume fraction and mean elastic modulus between samples.

We observed if there is any relationship between the mean volume fraction and the mean Young's modulus of each sample and compared all the samples to see if there was any trend Figure 4.28. The volume fraction of all samples vs the mean measured elastic modulus were computed. For all the samples, the collagen I seemed to be the only fibrillar protein that showed a substantial positive correlation with an R^2 =0.6081. This correlation is higher than the one with the calculated volume fraction from equation (2), R^2=0.2704. This shows that there is a

positive correlation between the measured E and the mean Collagen I volume fraction of the samples when the volume fraction is calculated with the maximum intensity value of each sample. Collagen III and elastin didn't show any correlation with an R^2=0.013 and R^2=0.0922 respectively. This results agree with the work of Michael S. Samuel et al. where they justify an elevated tissue stiffness via increased collagen [27], with the work of Kandic R. Levental et. al [28] and [29].

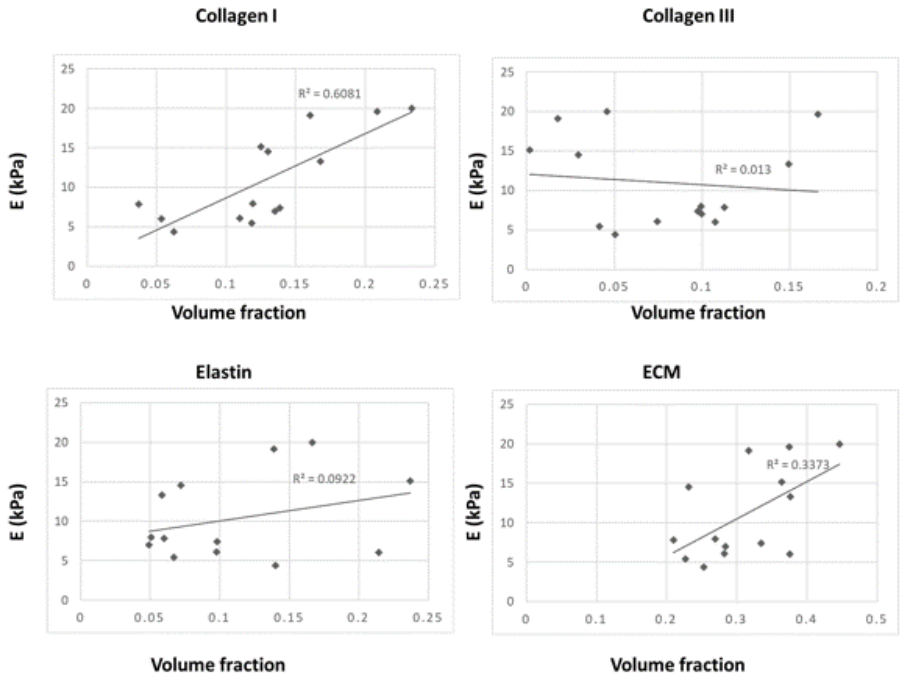

Figure 4.28 Relationship between the mean Young's modulus and the mean volume fraction of the three fibrillar proteins for all samples.

4.5 CONCLUSIONS

4.5.1 Measuring the Elastic Modulus of Lung ECM

Differences in the Elastic modulus of the lung ECM have been found between the cancerous ECM and the non-cancerous ECM. The cancerous ECM shows an Elastic modulus up to 5 times higher than the non-cancerous ECM, the mean E is increased 2.5 folds from the non-cancerous to the cancerous ECM. The measured values of the non-cancerous ECM range from 0.76 kPa to 16.45 kPa with a total mean value of all samples of 6.33 ±1.13 kPa, while the measured values of the cancerous ECM range from 0.2 kPa to 65 kPa with a total mean value of all samples of 15.65±4.04 kPa.

When both stiffness distributions are considered as one larger sample, the distribution fits a bimodal distribution. Each peak of the distribution is related to the cancerous and non-cancerous part of the ECM. The average of each peak on the bimodal distribution is overestimated due to the different indentation number between the cancerous and non-cancerous ECM, which can go up to a 30%. However, since both peaks are shown in every sample, this could be a robust diagnosis tool for lung cancer.

4.5.2 Structural composition differences between the non-cancerous and cancerous lung ECM

The mean of the intensities for each fibrillar protein between non-cancerous and cancerous ECM shows that, in most of the samples, there is an increase in the mean intensity of the Collagen I in cancerous ECM.

When calculating the volume fraction with equation (2), which uses as a reference value the maximum intensity value of each protein in all the samples, we found that collagen I in the cancerous lung ECM showed a mean volume fraction increase of 1.7-folds and up to 3.48 folds the volume fraction found in non-cancerous ECM. This data correlates with previous works that associate the increase of the stiffness of the cancerous tissue with the increment of Collagen I deposition and crosslinking [14], [28], [30], [31].

When calculating the volume fraction with equation (3) which uses as a reference value the maximum intensity value of each protein for the measured sample, we found that collagen I in the cancerous lung ECM showed a mean volume fraction increase of 1.5 folds and up to 3.74 folds the volume fraction found in non-cancerous ECM.

4.5.3 Matching the mechanical properties of the lung cancer ECM with its structural composition

The correlation between the measured Young's modulus of each sample and the volume fraction of protein on each indentation site seems to follow a positive trend: when the volume fraction increases, the measured Young's modulus increases for Collagen I.

The collagen I shows a low correlation R^2= 0.27 when comparing the mean Young's modulus with the mean volume fraction between samples in cancerous ECM nor non-cancerous ECM when the volume fraction of the proteins is calculated with equation (2).

When equation (3) is applied to calculate the volume fraction, the correlation of the mean Young's modulus with the mean volume fraction between samples in all samples increases up to R^2=0.6081, indicating that a higher volume fraction of Collagen I could be related with an increase of the stiffness of the ECM.

4.6 BIBLIOGRAPHY

[1] R. O. Hynes and A. Naba, "Overview of the matrisome-An inventory of extracellular matrix constituents and functions," *Cold Spring Harb. Perspect. Biol.*, vol. 4, no. 1, pp. 1–16, 2012.

[2] C. A. J. Hoeve and P. J. Flory, "The elastic properties of elastin," *Biopolymers*, vol. 13, no. 4, pp. 677–686, 1974.

[3] D. Vader, A. Kabla, D. Weitz, and L. Mahadevan, "Strain-induced alignment in collagen gels," *PLoS One*, vol. 4, no. 6, 2009.

[4] M. W. Conklin *et al.*, "Aligned collagen is a prognostic signature for survival in human breast carcinoma," *Am. J. Pathol.*, vol. 178, no. 3, pp. 1221–1232, 2011.

[5] J. M. C. Paolo P Provenzano*1, 2, Kevin W Eliceiri2 and 2 David R Inman1, John G White2 and Patricia J Keely*1, "Collagen reorganization at the tumor-stromal interface facilitates local invasion," *BMC Med.*, vol. 4, no. 38, pp. 190–195, 2006.

[6] R. M. S. Sigrist, J. Liau, A. El Kaffas, M. C. Chammas, and J. K. Willmann, "Ultrasound elastography: Review of techniques and clinical applications," *Theranostics*, vol. 7, no. 5, pp. 1303–1329, 2017.

[7] C. D. Madsen and T. R. Cox, "Relative Stiffness Measurements of Tumour Tissues by Shear Rheology," *Bio-protocol*, vol. 7, no. 9, p. e2265, 2017.

[8] I. Andreu *et al.*, "Heterogeneous micromechanical properties of the extracellular matrix in healthy and infarcted hearts," *Acta*

Biomater., vol. 10, no. 7, pp. 3235–3242, 2014.

[9] M. Lekka and P. Laidler, "Applicability of AFM in cancer detection," *Nat. Nanotechnol.*, vol. 4, p. 72, Feb. 2009.

[10] X. Deng *et al.*, "Application of atomic force microscopy in cancer research," *J. Nanobiotechnology*, vol. 16, no. 1, p. 102, 2018.

[11] M. Lekka, "Discrimination Between Normal and Cancerous Cells Using AFM," *Bionanoscience*, vol. 6, no. 1, pp. 65–80, 2016.

[12] Q. S. Li, G. Y. H. Lee, C. N. Ong, and C. T. Lim, "Probing the Elasticity of Breast Cancer Cells Using AFM BT - 13th International Conference on Biomedical Engineering," 2009, pp. 2122–2125.

[13] J. I. Lopez, I. Kang, W. K. You, D. M. McDonald, and V. M. Weaver, "In situ force mapping of mammary gland transformation," *Integr. Biol.*, vol. 3, no. 9, pp. 910–921, 2011.

[14] A. Stylianou and T. Stylianopoulos, "Atomic Force Microscopy Probing of Cancer Cells and Tumor Microenvironment Components," *Bionanoscience*, vol. 6, no. 1, pp. 33–46, 2016.

[15] A. J. Rice *et al.*, "Matrix stiffness induces epithelial-mesenchymal transition and promotes chemoresistance in pancreatic cancer cells," *Oncogenesis*, vol. 6, no. 7, pp. 1–9, 2017.

[16] T. Luque *et al.*, "Local micromechanical properties of decellularized lung scaffolds measured with atomic force microscopy," *Acta Biomater.*, vol. 9, no. 6, pp. 6852–6859, 2013.

[17] Y. Zhou *et al.*, "Extracellular matrix in lung development, homeostasis and disease," *Matrix Biol.*, no. 2017, 2018.

[18] M. Asgari, N. Latifi, H. K. Heris, H. Vali, and L. Mongeau, "In vitro fibrillogenesis of tropocollagen type III in collagen type i affects its relative fibrillar topology and mechanics," *Sci. Rep.*, vol. 7, no. 1, pp. 1–10, 2017.

[19] J. Alcaraz *et al.*, "Microrheology of human lung epithelial cells measured by atomic force microscopy," *Biophys. J.*, vol. 84, no. 3, pp. 2071–2079, 2003.

[20] D. C. Lin, E. K. Dimitriadis, and F. Horkay, "Robust Strategies for Automated AFM Force Curve Analysis—I. Non-adhesive Indentation of Soft, Inhomogeneous Materials," *J. Biomech. Eng.*, vol. 129, no. 3, p. 430, 2007.

[21] S. P. and J. S. Jean-Yves Tinevez, Mark Longair, "Tubeness." .

[22] M. Plodinec *et al.*, "The nanomechanical signature of breast cancer.," *Nat. Nanotechnol.*, vol. 7, no. 11, pp. 757–65, 2012.

[23] M. Lekka *et al.*, "Cancer cell detection in tissue sections using AFM," *Arch. Biochem. Biophys.*, vol. 518, no. 2, pp. 151–156, 2012.

[24] M. W. Conklin *et al.*, "Aligned collagen is a prognostic signature for survival in human breast carcinoma," *Am. J. Pathol.*, vol. 178, no. 3, pp. 1221–1232, 2011.

[25] D. O. Velez *et al.*, "3D collagen architecture induces a conserved migratory and transcriptional response linked to vasculogenic mimicry," *Nat. Commun.*, vol. 8, no. 1, 2017.

[26] T. R. Cox *et al.*, "LOX-mediated collagen crosslinking is responsible for fibrosis-enhanced metastasis," *Cancer Res.*, vol. 73, no. 6, pp. 1721–1732, 2013.

[27] M. S. Samuel *et al.*, "Actomyosin-mediated cellular tension drives increased tissue stiffness and β-catenin activation to induce epidermal hyperplasia and tumor growth," *Cancer Cell*, vol. 19, no. 6, pp. 776–791, 2011.

[28] K. R. Levental *et al.*, "Matrix Crosslinking Forces Tumor Progression by Enhancing Integrin Signaling," *Cell*, vol. 139, no. 5, pp. 891–906, 2009.

[29] L. Kass, J. T. Erler, M. Dembo, and V. M. Weaver, "Mammary epithelial cell : Influence of extracellular matrix composition and organization during development and tumorigenesis," vol. 39, pp. 1987–1994, 2007.

[30] G. Akiri *et al.*, "Lysyl oxidase-related protein-1 promotes tumor fibrosis and tumor progression in vivo," *Cancer Res.*, vol. 63, no. 7, pp. 1657–1666, 2003.

[31] D. T. Butcher, T. Alliston, and V. M. Weaver, "A tense situation: Forcing tumour progression," *Nat. Rev. Cancer*, vol. 9, no. 2, pp. 108–122, 2009.

5

ESHELBY'S MODEL TO PREDICT THE MECHANICAL BEHAVIOR OF THE LUNG CANCEROUS AND NON-CANCEROUS EXTRACELLULAR MATRIX

The aim of this chapter is to predict the elastic properties of the lung cancerous and non-cancerous Extracellular Matrix from its microstructure using a model based on the Eshelby method. These models have been extensively used for composite materials and the goal is to assess their validity for ECM. The input parameters of the model are obtained from the immunofluorescence images of lung ECM described in chapter 4. The model is then used to predict the experimental elastic moduli obtained from the Atomic Force Spectroscopy indentations performed in cancerous and non-cancerous lung ECM slices.

5.1 THE ECM AS A COMPOSITE MATERIAL. MODEL DESCRIPTION

A composite material can be defined as a combination of two or more materials that results in better properties than those of the individual components used alone. The two constituents of a composite material are a reinforcement and a matrix. The reinforcement provides the strength and stiffness and in most cases is harder, stronger and stiffer

than the matrix. The matrix performs several critical functions, including maintaining the fibers in the proper orientation and spacing and protecting them from abrasion and the environment [1].

Tissue extracellular matrix (ECM) is a complex material made up of fibrous proteins, proteoglycans and other biomolecules [2]. The ECM can be represented as a composite material, in which the matrix (proteoglycans) is reinforced by fibers (fibrous proteins). Tissues characterized by one family of fibers are, for example, tendons and ligaments [3]. The interstitial ECM of the lung is composed of a relaxed meshwork, largely based on type I and III collagens and elastin as important core fibrous proteins [4]. Apart from fibrous collagens and glycoproteins, proteoglycans (PGs) are major constituents of the ECM. Proteoglycans consist of a core protein component covalently linked to sulfated polysaccharides or glycosaminoglycans (GAGs). [5].

Therefore, we can consider the ECM as a composite material with a matrix mainly of proteoglycans reinforced with collagen I, collagen III and elastin fibers. There exist several micromechanical models in literature to predict the elastic, thermal and electrical properties of composite materials based on the properties of the individual phases and the architecture of the reinforcement (volume fraction, aspect ratio, orientation). These models can be divided in two main groups: analytical models based in the equivalent inclusion method and numerical models based in the Finite Element Method (FEM) combined with the Representative Volume Element (RVE) [6]. FEM models are best suited when local behavior needs to be studied but these models are complex and costly computationally.

The purpose of this study is to assess the capability of predicting the elastic modulus of the ECM from its microstructure and the properties of its constituents using a model for composite materials based on the equivalent inclusion model and the Differential Effective Medium (DEM) approach.

5.1.1 The elastic inclusion problem

5.1.1.1 *The fundamental Eshelby's solution in elasticity*

Most models to predict the average physical properties of multiphase materials are based on Eshelby's solution for the problem of the behaviour of an ellipsoidal region (the inclusion) within an elastic matrix [7]. Eshelby illustrated the problem as a series of virtual cutting and welding experiments.

Consider a homogeneous elastic medium ("the matrix"), see Figure 5.1. We extract a region ("the inclusion") and change its shape without introducing stresses. This strain originated in a stress-free state is called an eigenstrain or transformation strain, $\boldsymbol{\varepsilon}^*$. In order to introduce the inclusion back in the original position, surface tractions must be applied to recover the original shape. Once back in position, the two regions are welded and the surface tractions are removed. Then when reaching equilibrium between matrix and inclusion, a constrained strain $\boldsymbol{\varepsilon}^C$ appears in the inclusion relative to the original shape before removal.

Eshelby demonstrated that for ellipsoidal inclusions the constrained strain $\boldsymbol{\varepsilon}^C$ is uniform and is related to the eigenstrain $\boldsymbol{\varepsilon}^*$ by means of a fourth order tensor, termed the Eshelby $\mathbf{S}$ tensor, which depends on the shape of the inclusion and the elastic properties of the matrix [8].

$$\boldsymbol{\varepsilon}^{C} = \mathbf{S}\boldsymbol{\varepsilon}^{*} \tag{1}$$

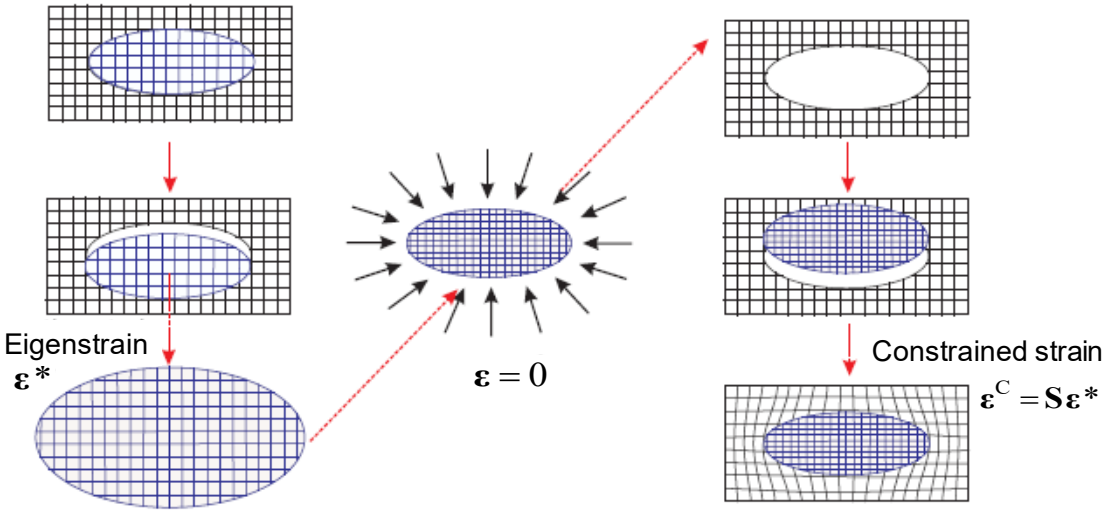

*Figure 5.1 Eshelby's cutting and welding exercises for an ellipsoidal inclusion. The constrained strain $\boldsymbol{\varepsilon}^{C}$ is related to the eigenstrain $\boldsymbol{\varepsilon}^{*}$ through the Eshelby **S** tensor.*

5.1.1.2 *The equivalent elastic inclusion*

The fundamental solution of Eshelby can be used to solve the problem of an inclusion of stiffness $\mathbf{C}_{\mathrm{I}}$ embedded in a matrix of different stiffness, $\mathbf{C}_{\mathrm{M}}$. Assume we apply a remote strain $\boldsymbol{\varepsilon}$. The strain in the inclusion can then be written as the remote strain $\boldsymbol{\varepsilon}$ corrected by a constrained strain $\boldsymbol{\varepsilon}^{C}$,

$$\boldsymbol{\varepsilon}_{\mathrm{I}} = \boldsymbol{\varepsilon} + \boldsymbol{\varepsilon}^{C} \tag{2}$$

and therefore, the stress in the inclusion is given by

$$\boldsymbol{\sigma}_{\mathrm{I}} = \mathbf{C}_{\mathrm{I}}(\boldsymbol{\varepsilon} + \boldsymbol{\varepsilon}^{\mathrm{C}}) \tag{3}$$

The problem can be solved in an alternative way using the concept of the *equivalent homogeneous inclusion* (sometimes called the *ghost* inclusion) made of the matrix material, and then applying Eshelby's fundamental solution for the homogeneous inclusion. In this equivalent problem, the eigenstrain, $\boldsymbol{\varepsilon}^*$, must be chosen such that the resulting strain and stress in the inclusion be the same as in the real inclusion. Therefore the strain is again given by Eq. (2) and taking into account that the eigenstrain $\boldsymbol{\varepsilon}^*$ corresponds to a stress-free state, the stress in the equivalent problem is now

$$\boldsymbol{\sigma}_{\mathrm{I}} = \mathbf{C}_{\mathrm{M}}(\boldsymbol{\varepsilon} + \boldsymbol{\varepsilon}^{\mathrm{C}} - \boldsymbol{\varepsilon}^*) \tag{4}$$

Using Eqs. (1), (3) and (4), the required eigenstrain is obtained as

$$\boldsymbol{\varepsilon}^* = -\left[(\mathbf{C}_{\mathrm{I}} - \mathbf{C}_{\mathrm{M}})\mathbf{S} + \mathbf{C}_{\mathrm{M}}\right]^{-1}(\mathbf{C}_{\mathrm{I}} - \mathbf{C}_{\mathrm{M}})\boldsymbol{\varepsilon} \tag{5}$$

And using Eqs. (1), (2) and (5), the resulting strain in the inclusion is

$$\boldsymbol{\varepsilon}_{\mathrm{I}} = \mathbf{A}_{\mathrm{I}}\boldsymbol{\varepsilon} \tag{6}$$

$$\mathbf{A}_{\mathrm{I}} = \left[\mathbf{I} + \mathbf{S}\mathbf{C}_{\mathrm{M}}^{-1}(\mathbf{C}_{\mathrm{I}} - \mathbf{C}_{\mathrm{M}})\right]^{-1} \tag{7}$$

where **I** is the unit tensor of fourth order. The fourth order tensor $\mathbf{A}_{\mathrm{I}}$ is called the strain concentration tensor for dilute systems.

5.1.2 The mean field approach in dilute systems

The mean field models determine the effective properties of the composite assuming that the relevant variables (the stress and strain fields in the elastic problem) in each phase are well defined through their average values. The effective stress, σ, and strain, ε, are calculated by integrating the corresponding average values of the variables in each phase,

$$\boldsymbol{\sigma} = f_M \boldsymbol{\sigma}_{\mathbf{M}} + \sum_{\alpha=1}^{N} f_\alpha \boldsymbol{\sigma}_{\boldsymbol{\alpha}} \qquad (8)$$

$$\boldsymbol{\varepsilon} = f_M \boldsymbol{\varepsilon}_{\mathbf{M}} + \sum_{\alpha=1}^{N} f_\alpha \boldsymbol{\varepsilon}_{\boldsymbol{\alpha}} \qquad (9)$$

$$f_M = 1 - \sum_{\alpha=1}^{N} f_\alpha \qquad (10)$$

where M stands for the matrix, $\alpha = 1,2,\dots,N$ for the N phases embedded in the matrix and f_M and f_α are the volume factions of matrix and phases of inclusions. For the matrix and the N embedded phases, we have

$$\boldsymbol{\sigma}_{\boldsymbol{\alpha}} = \mathbf{C}_{\boldsymbol{\alpha}} \boldsymbol{\varepsilon}_{\boldsymbol{\alpha}} \text{ and } \boldsymbol{\sigma}_{\mathbf{M}} = \mathbf{C}_{\mathbf{M}} \boldsymbol{\varepsilon}_{\mathbf{M}} \qquad (11)$$

On the other hand, applying Eshelby's theory we can write the strain in each phase using the concentration tensors $\mathbf{A}_\alpha$, see Eqs. (6)-(7),

$$\boldsymbol{\varepsilon}_{\boldsymbol{\alpha}} = \mathbf{A}_{\boldsymbol{\alpha}} \boldsymbol{\varepsilon} \qquad (12)$$

Using Eqs. (8)-(12), the effective stress in the composite can be related to the effective strain as

$$\boldsymbol{\sigma} = \mathbf{C_c}\boldsymbol{\varepsilon} \qquad (13)$$

Where $\mathbf{C_c}$ is the effective stiffness of the composite given by

$$\mathbf{C}_{\mathrm{C}} = \mathbf{C}_{\mathrm{M}} + \sum_{\alpha=1}^{N} f_{\alpha}(\mathbf{C}_{\alpha} - \mathbf{C}_{\mathrm{M}})\mathbf{A}_{\alpha} \qquad (14)$$

5.1.3 Stiffness in non-dilute systems: the DEM approach

The relation given in Eq. (14) is valid for a dilute system, i.e., where the inclusion volume fractions are small enough that the concentration tensors given by Eq. (7) are valid. In order to incorporate higher volume fractions, the interaction between the different inclusions has to be considered. There exist a number of methods to account for finite volume fractions of inclusions. Here we mention the mean field approach (MFA) version of Mori-Tanaka [9] reformulated by Benveniste [10], which will be termed MTB, and the Differential Effective Medium (DEM) approach, see for example McLaughlin [11]. In this work we decide to implement the DEM scheme as it is "exact" in the sense that we use Eshelby's solution for

dilute systems in an incremental process while the MFA is an approximation which interpolates between exact solutions for $f \to 0$ and for $f \to 1$. Besides, several works show [12]–[14] the superior predictive capability of the DEM scheme in the case of high contrast of properties between matrix and inclusion and for high volume fractions.

The starting point is Eshelby's solution for dilute concentrations of a single phase of inclusions in a matrix subject to a remote strain, i.e., from Eq. (14) we have

$$\mathbf{C}_{\mathrm{C}} = \mathbf{C}_{\mathrm{M}} + c(\mathbf{C}_{\mathrm{I}} - \mathbf{C}_{\mathrm{M}})\mathbf{A}_{\mathrm{I}} \qquad (15)$$

where now we call c ($c \to 0$) the volume fraction of inclusions.

In the DEM scheme, we apply this solution in an incremental manner as follows. Assume $\mathbf{C}_{\mathrm{C}}$ is the stiffness of a compound with a volume faction f (which can be non-dilute) of inclusions. (Note that $\mathbf{C}_{\mathrm{C}}$ is unknown for the moment.) We replace the composite by a homogeneous material having the same stiffness $\mathbf{C}_{\mathrm{C}}$. We want to compute the stiffness for a volume fraction $f + \Delta f$. Imagine a unit volume of composite with stiffness $\mathbf{C}_{\mathrm{C}}$ corresponding to f. We add an infinitesimal volume Δv of inclusions. Therefore the volume fraction of new inclusions in the "homogeneous material" of stiffness $\mathbf{C}_{\mathrm{C}}$ is $\frac{\Delta v}{1+\Delta v}$. It is easy to show that $\frac{\Delta v}{1+\Delta v} = \frac{\Delta f}{1+\Delta f}$. Then, the stiffness of the new composite, $\mathbf{C}_{\mathrm{C}}^{*}$, can be obtained using the dilute solution as

$$\mathbf{C}_{\mathrm{C}}^{*} = \mathbf{C}_{\mathrm{C}} + \frac{\Delta f}{1-f}(\mathbf{C}_{\mathrm{I}} - \mathbf{C}_{\mathrm{C}})\mathbf{A}_{\mathrm{I}} \qquad (16)$$

Note that now $\mathbf{A}_{\mathrm{I}}$ is not constant as it depends on the instantaneous value of the stiffness of the "homogeneous composite", i.e.,

$$\mathbf{A}_{\mathrm{I}} = \left[\mathbf{I} + \mathbf{S}\mathbf{C}_{\mathrm{C}}^{-1}(\mathbf{C}_{\mathrm{I}} - \mathbf{C}_{\mathrm{C}})\right]^{-1} \qquad (17)$$

The relation (16) can be written as

$$\frac{\mathbf{C}_{\mathrm{C}}^{*} - \mathbf{C}_{\mathrm{C}}}{\Delta f} = \frac{1}{1-f}(\mathbf{C}_{\mathrm{I}} - \mathbf{C}_{\mathrm{C}})\mathbf{A}_{\mathrm{I}} \qquad (18)$$

And finally, in the limit as $\Delta f \to 0$ we have

$$\frac{\mathrm{d}\mathbf{C}_{\mathrm{C}}}{\mathrm{d}f} = \frac{1}{1-f}(\mathbf{C}_{\mathrm{I}} - \mathbf{C}_{\mathrm{C}})\left[\mathbf{I} + \mathbf{S}\mathbf{C}_{\mathrm{C}}^{-1}(\mathbf{C}_{\mathrm{I}} - \mathbf{C}_{\mathrm{C}})\right]^{-1} \qquad (19)$$

This is a first order ordinary differential equation for matrix $\mathbf{C}_{\mathrm{C}}$ with initial conditions $\mathbf{C}_{\mathrm{C}} = \mathbf{C}_{\mathrm{M}}$ for $f = 0$. This equation can be integrated to obtain the stiffness matrix of the composite at any volume fraction of inclusions. In general, the above ODE has to be solved numerically. An equivalent

stiffness is calculated from the stiffness matrix as an average of the orientation dependent Young modulus.

5.1.4 Input parameters

The model implemented in Matlab works with an idealized microstructure defined from the data obtained in Chapter 4 from immunofluorescence images of lung ECM. The input parameters in the implemented model are:

1. The elastic modulus of the matrix where the fibers are embedded: E_{Matrix}
2. A number N of phases representing fibers with the same elastic modulus, aspect ratio and orientation
3. For each phase or group of fibers:
    a. The volume fraction of fibers: V_α
    b. The aspect ratio
    c. The orientation
    d. The elastic modulus: E_α
    e. Poisson's ratio: 0.3

Both the matrix and the fibers are considered isotropic.

The input parameters should be determined from the immunofluorescence images of lung ECM and the corresponding effective elastic modulus measured with the AFM (chapter 4). However, several limitations should be considered.

First, the elastic modulus of the proteoglycan matrix where the fibers are embedded cannot be directly obtained from the AFM indentation experiments since the tip used had a diameter of 20 μm. This means that the volume tested will contain fibers and hence we do not have spatial resolution to test only the matrix. The same apply for the nanometric fibers. Therefore, we need to use data from bibliography as starting point and validate these data using the model and the experimental results for the elastic modulus of the ECM.

In various works, lung material is assumed to be elastic. Its mechanical properties are described with the Young modulus and the Poisson's ratio. A clinical test called compliance provides the ratio of air volume variation to the related air pressure variation. If alveolar surface tension is ignored, a link between this static compliance and the elastic properties could be established [15]. This pressure-volume curve provides then enough information to estimate bulk modulus. Poisson's ratio (v) is quite difficult to measure. Using the technique of finite elements, West and Matthews [16] studied how the lung is deformed by its own weight. However, the lack of data on human lung tissues brought them to measure dog lung mechanical parameters. They found and used a mean value v = 0.3. Lambert and Wilson [17] developed a mathematical model of elastic properties for a lung parenchyma considered as randomly oriented. Values of elastic moduli are obtained from the pressure-volume diagram for the whole lung. They obtained v = 0.25. Lai-Fook [18] used two tests of uniaxial compression on dog lung lobes between parallel plates and punch indentations. They obtained v = 0.47. Although these data are very few and only belong to dogs, recent works refer to these three values. Alder et al. [19] used v = 0.49 in a model considering

mechanical and electrical properties. Owen et al. [15] used v = 0.3 for a study of high-frequency ventilation influence on lung tissue. Grimal [20] used v = 0.3 in his model of injuries modelling of thoracic impact.

Second, regarding the architecture, we should note that the image resolution is too big to differentiate single fibers so we cannot measure their orientation and aspect ratio. However, we can distinguish bundles of fibers that will be considered in the model as single fibers with a given aspect ratio and orientation. Regarding the orientation, since the technique employed to image the tissue is based on epifluorescence, a 2D projection of the sample, the orientation will be measured in-plane and the out-of-plane dimension will be lost.

Finally, as explained in previous chapters of this thesis, it is not possible to measure the actual volume fraction of the fibers from the images obtained. Instead, a relative volume fraction of the protein in the ECM is obtained as follows for example for collagen I:

$$Vf = \frac{\sum ICollI}{NpECM*(ImaxColI+ImaxColIII+ImaxElastin)} \quad (20)$$

Where V_f is the volume fraction of the calculated protein, the ICollI is each of the intensities of CollI protein in that quadrant, ImaxCollI, ImaxCollIII and ImaxElastin are the maximum intensities measured for CollagenI, CollagenIII and Elastin and NpECM is the number of pixels where there is at least one of the three proteins.

Taking into account all the above mentioned limitations and the fact that it has been reported and observed in this work that Collagen I is the fiber mainly affecting the overall elastic properties of the ECM, the first decision is to simplify the model considering only the Collagen I fibers in the idealized model of the ECM.

5.2 STRATEGY TO DEFINE THE INPUT PARAMETERS FOR THE COMPOSITE MODEL OF THE ECM

In this section, we describe the strategy used to define the input parameters for the model from the images and AFM experiments described in chapter 4. For this purpose, the effect of different input parameters is studied using the model and combining measured inputs and data from bibliography. Then the results are compared with the effective elastic modulus measured by AFM.

5.2.1 Effect of the elastic modulus of the matrix where the fibers are embedded.

In order to study the effect of the elastic modulus of the matrix on the overall behavior of the composite, that is the ECM, several simulations are run and the results compared with the effective modulus measured with the AFM.

The collagen I fibers are assumed to be randomly distributed throughout the sample, their elastic modulus and aspect ratio is obtained from bibliography [21], [22]. The diameter of a collagen I fiber can range from 30 nm to 1000 nm and its length can go up to a millimeter. The elastic modulus of a single collagen I fiber can range from 100 to 360 MPa, in these simulations the value was set at 100 MPa. The model was employed to study the effect of varying the ratio between the elastic modulus of the Collagen I fibers and the elastic modulus of the matrix. The practical limit of reinforcement that can be added to form a composite when the fibers are continuous and aligned is a volume fraction of 0.7. For continuous and random fibers, the limit is set at 0.5[1]. Therefore, the volume fraction of the Collagen I fibers was increased from 0.0001 to 0.50001 in 0.1 steps. All the input parameters used in the simulations are gathered in Table 5.1.

Table 5.1 Input parameters of the Eshelby's model used to study the effect of the Young modulus of the matrix embedding the collagen I fibers on the equivalent modulus of the ECM

Input Parameter	*Value*
Volume Fraction of fibers	0 to 0.5
E of the Collagen I	100 MPa
E of the matrix	From 0.01 kPa to 100 kPa
Aspect ratio of fibers	10000
Fiber Direction	Random 3D

The model was run for a total of five different matrix stiffnesses ranging between 100 kPa and 0.01 kPa and 100MPa Collagen I fibers. The fibers were supposed to be aligned randomly in 3D, Figure 5.2 3D Random fiber orientation representation

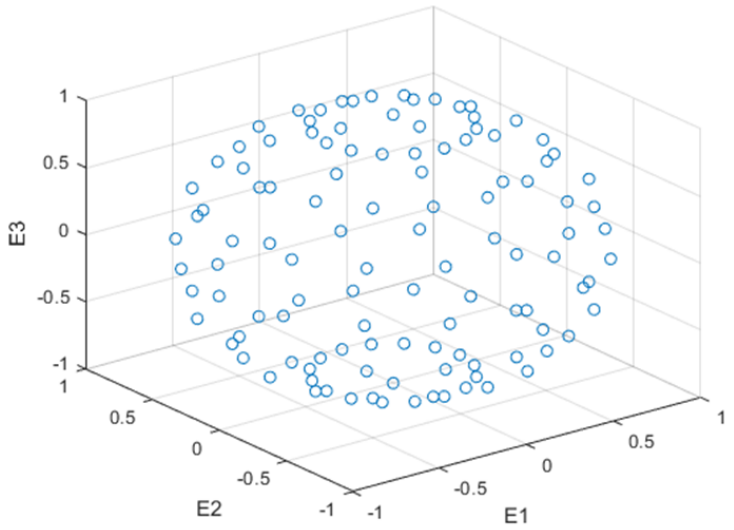

.

Figure 5.2 3D Random fiber orientation representation

Table 5.2 Results of the estimated E_{ECM} for a 3D randomly oriented 100MPa Collagen I fibers as the volume fraction increases and the E of the matrix decreases.

	100kPa	10kPa	1 kPa	0.1 kPa	0.01kPa
fv	E_{ECM}	E_{ECM}	E_{ECM}	E_{ECM}	E_{ECM}
0.001	118.636027	27.4366261	17.9185167	16.9374727	16.8321547
0.101	1829.36221	1714.83591	1703.32522	1702.16749	1702.04563
0.201	3542.69773	3402.86659	3388.82938	3387.41985	3387.27356
0.301	5270.52884	5092.3722	5074.48234	5072.6881	5072.50413
0.401	7025.02506	6784.5824	6760.40661	6757.98396	6757.73792
0.501	8834.46588	8482.39579	8446.89258	8443.33628	8442.97763

The resulting E_{ECM} for a 3D randomly oriented 100MPa Collagen I fibers, Figure 5.2, does not show any results close to the measured E in previous chapters, 4-8 kPa for the non-cancerous ECM and 8-20 kPa for the cancerous ECM, for a reasonable volume fraction, between 0.05 and 0.15.

Figure 5.3 shows the predicted elastic modulus of the ECM (E_{ECM}) as a function of the volume fraction of collagen I for different values of the elastic modulus of the matrix (E_{matrix}). Besides, the horizontal blue line represents the maximum E_{ECM} measured with the AFM for all the lung samples, which was of 65 kPa. Firstly, it is observed that when E_{matrix} is at least 1000 times lower than E_{coll}, the effect of the elastic modulus of the matrix on the properties on the ECM can be neglected for a volume fraction of fibers above 0.1. In fact, when E_{matrix} is 1000 times smaller than E_{coll}, reducing the E_{matrix} by one order of magnitude introduces an error of 6.67% for a volume fraction of 0.1. This error is reduced as the volume fraction of collagen I increases up to 4.15% for a volume fraction of 0.5 (see Table 5.2).

Firstly, it is not possible to measure the stiffness of the proteoglycan matrix with the tip used for the AFM experiments as the volume tested will contain the protein fibers of the ECM. However, the mean E_{ECM} value measured for the non-cancerous ECM is around 7 kPa, and the lowest mean values are found near 1 kPa. It is then reasonable to assume that the stiffness of the matrix would be lower than this value. Therefore, taking into account these experimental results, the value of 100 MPa reported for the collagen I fibers in bibliography and negligible effect of the elastic modulus of the matrix when it is 3 orders of magnitude smaller than the elastic modulus of the fibers, that is 100 kPa, it is decided to use a value of 1 kPa for the elastic modulus of the matrix.

Secondly, it is observed that all the predicted values of the E_{ECM} are significantly higher than the maximum E_{ECM} value of 65 kPa obtained from AFM indentations performed on the lung ECM. The volume fractions calculated from the immunofluorescence assays vary from 0.03 to 0.28. However, with the model we are obtaining values of 3388 kPa for a volume fraction of 0.2 and an E_{Matrix} of 1 kPa, which is about 50 times bigger than the highest measured stiffness in lung.

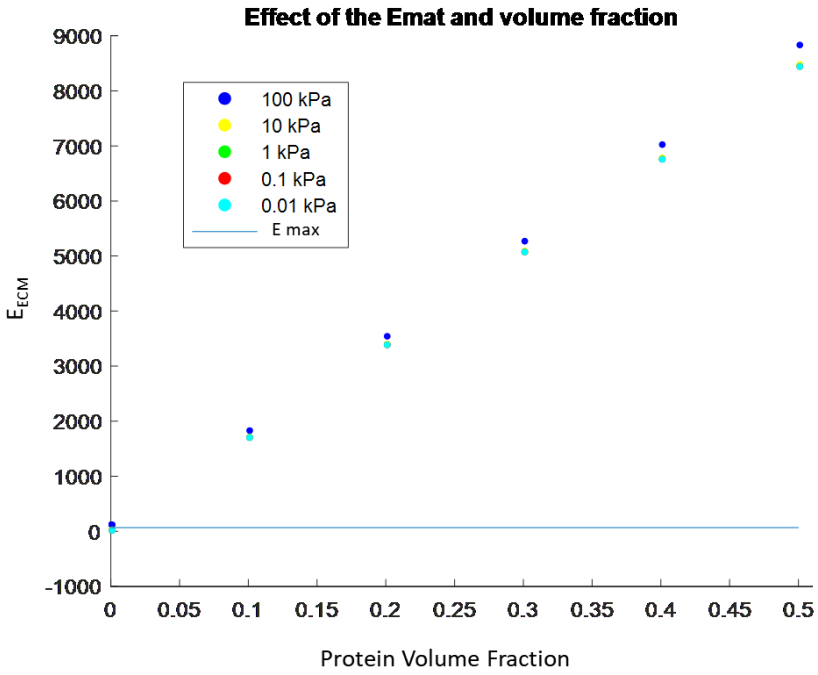

Figure 5.3 Predicted elastic modulus of the ECM (E_{ECM}) as a function of the volume fraction of collagen I for different values of the elastic modulus of the matrix (E_{matrix}). The horizontal blue line represents the maximum E_{ECM} measured with the AFM for all the lung samples, which was of 65 kPa.

Since the results were much higher than expected using the elastic modulus of the Collagen reported in other works (100-360 MPa) [6], it was decided to characterize the elastic modulus of Collagen I fibers using the model and experimental AFM measurements.

5.2.2 Effect of the fiber orientation

Since the resolution of the immunofluorescence technique employed to measure the lung ECM proteins was not enough to distinguish single collagen I fibers, the aspect ratio and orientation of bundles of fibers was measured instead as Figure 5.4 shows. The volume fraction of the protein that could not be measured as bundled fibers was supposed to be randomly oriented in the three dimensional space with an aspect ratio of 10000 [22].

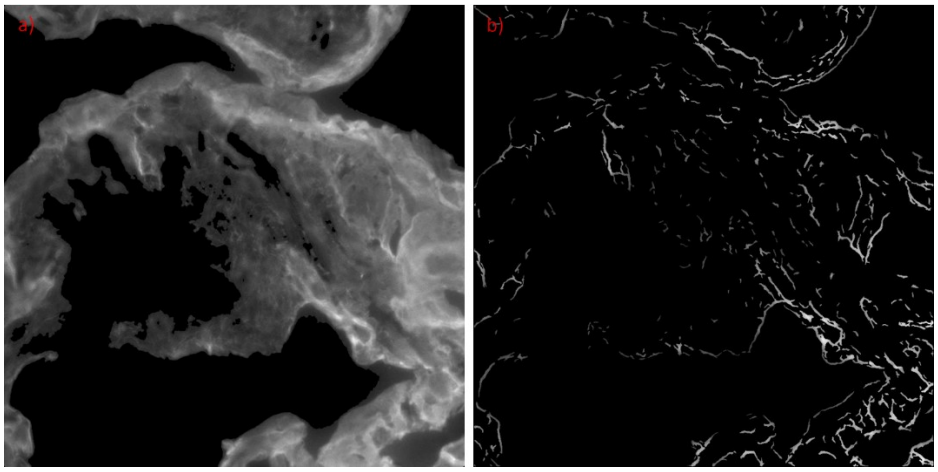

Figure 5.4 a) Unmixed Collagen I immunofluorescence. b) Image after the fiber segmentation. As b) shows, just a part of the whole collagen can be observed as bundled fibers. The aspect ratio and orientation of these bundles were measured as model inputs.

The effect of the fiber orientation on the E_{ECM} was studied by generating different cases of 2D and 3D random fiber orientation. A total of 4 different models were proposed and are gathered in Figure 5.5, being X and Y the directions of the plane that holds the sample and Z the direction

in which the AFM indentations were performed (normal to the sample surface). The inputs used for the model are gathered in Table 5.3

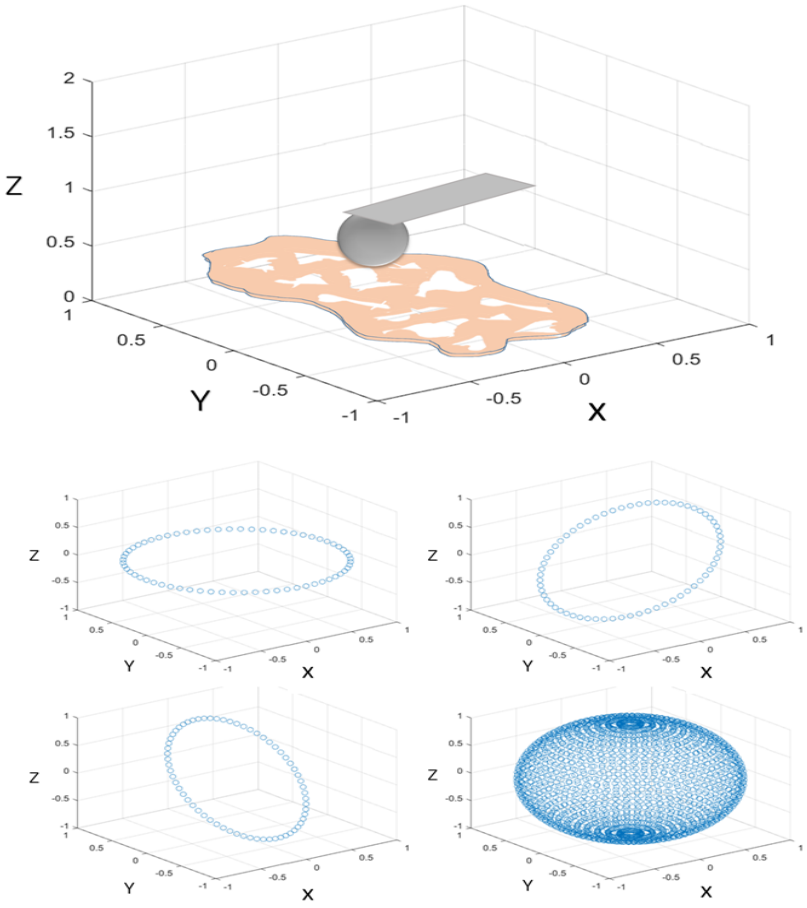

Figure 5.5 Top. Scheme of the sample and the AFM tip during the indentation assay. The tip moves parallel to the Z axis perpendicular to the surface of the lung ECM slice that is contained in the XY plane. Bottom. The 4 fiber distributions introduced for all of them randomly oriented: the 3 planes (XY, YX and XZ) and the 3D (XYZ) fiber distribution.

Table 5.3 Input parameters of the Eshelby's model used to study the effect of different fiber orientations (see figure 5.4.) on the equivalent modulus of the ECM

Input Parameter	*Value*
Volume Fraction of fibers	0.001 to 0.501
E of the Collagen I	100 MPa
E of the matrix	1 kPa
Aspect ratio of fibers	10000
Fiber Direction	Random 2D in X and Y Random 2D in X and Z Random 2D in Y and Z Random 3D

For this study, the E_{ColI} was kept as 100MPa. The results are gathered in kPa in Table 5.4. As expected, in all the cases the E_{ECM} increases as the volume fraction of fibers increases. For fibers randomly distributed in the XY plane, the E_{ECM} varies form 5.7 kPa for a volume fraction of 0.01 up to 222 kPa for a volume fraction of 0.501. For the fibers randomly distributed within planes XZ and YZ identical results are obtained, as expected as both configurations are equivalent. The E_{ECM} obtained ranges from 5.7 kPa up to 230 kPa for a volume fraction of 0.501. It should be noted that the predicted E_{ECM} is very similar if we consider the fibers distributed randomly in one plane, independently of the plane considered: the maximum difference if of 3.7% for a volume fraction of fibers of 0.5. The loweest values of the E_{ECM} are obtained when the fibers are distributed randomly within the sample XY plane. When the fibers are randomly oriented in 3D, the E_{ECM} goes from 17.9 kPa for a volume fraction

of 0.01 up to 8446 kPa for a volume fraction of 0.501. That is, for a volume fraction above 0.1, the E_{ECM} is multiplied by more than 25 when the fibers are distributed in 3 dimensions instead of in 2 dimensions. In any case, all these values are above the values measured for the healthy lung ECM where the highest measured value is 7.98 ± 3.23 kPa.

Table 5.4 Results of the model when calculating the elastic modulus of the ECM with the 4 proposed orientation distributions for fibers embedding a matrix of 1 kPa and a volume fraction of Collagen I fibers ranging from 0.01 to 0.501 with an elastic modulus of 100 MPa.

	XY	XZ	YZ	XYZ
Collagen I volume fraction	***E_{ECM} (kPa)***	***E_{ECM} (kPa)***	***E_{ECM} (kPa)***	***E_{ECM} (kPa)***
0.01	5.739	5.739	5.739	17.918
0.101	61.045	61.835	61.835	1703.325
0.201	92.716	95.772	95.772	3388.829
0.301	125.751	131.213	131.213	5074.482
0.401	166.559	173.901	173.901	6760.406
0.501	222.051	230.253	230.253	8446.892

The results shown in Table 5.4 fit with the results obtained by Simha et al. [23] for a volume fraction between 0.05 and 0.15, and an elastic modulus of 120MPa of the Collagen fibers on the cartilaginous tissue. But for our experimental data and using for the model an elastic modulus of 1 kPa and 100 MPa for the matrix and the collagen I fibers respectively, we have reached the next conclusions:

1. The predicted E_{ECM} values are much higher than the E_{ECM} measured by AFM. For a range of volume fractions between 0.05 and 0.15, the measured E_{ECM} ranges between 1 and 40 kPa whereas the predicted E_{ECM} for a volume fraction of 0.1 ranges between 1703 kPa and 6760 kPa for a volume fraction of 0.2.
2. When the fibers are distributed in 3D, the E_{ECM} is two orders of magnitude higher than when the fibers are distributed in 2D for a volume fraction of fibers above 0.1.
3. When the fibers are oriented in a 2D plane, the effect of the plane orientation has not much significance in the real volume fraction range (<0.5). Also, the results obtained for the modulus of the ECM are closer to the effective elastic modulus measured by AFM.

Taking into account these results, both 2D and 3D distributions are studied. For the 3D distribution, as previously mentioned, the elastic modulus of the collagen I fibers will be calculated from the AFM measurements using the model. The 2D distribution approach is described in section 5.3.2.

5.2.3 Measurement of the elastic modulus of Collagen I fibers using the Eshelby's model. Fibers randomly oriented in 3D

As has been observed in previous results, the predicted E_{ECM} is much higher than the ones measured by means of AFM force spectroscopy when using an elastic modulus of 100 MPa for collagen I fibers distributed

randomly in 3D. To overcome this problem, the model implemented is used to calculate the elastic modulus of collagen I fibers E_{CollI} from the effective elastic modulus of the ECM measured by AFM using the values measured for the 10 points with higher Collagen I volume fraction. The model is first used considering all the fibers distributed randomly in 3D, But, in a second step, the volume fraction, orientation and aspect ratio of the "bundled" collagen I fibers are also considered.

It should be noted that the effect of the crosslinking was not measured in this work. However, there is a relationship reported between the grade of crosslinking to fibrosis and collagen deposition on the cancerous ECM, [24]–[26], Therefore, the E_{CollI} was calculated separately using the data from cancerous and non-cancerous ECM. This means that two sets of 10 tests with the highest volume fraction of Collagen I fibers were selected independently from all the tests performed on cancerous and non-cancerous ECM.

5.2.3.1 *Elastic modulus of collagen I assuming long fibers randomly distributed in three dimensions.*

The immunofluorescence images were sectioned in a 20x20 grid equivalent to the 20x20 AFM indentations made for the characterization of the elastic modulus of the lung ECM, Figure 5.6 Colocalization of the higher values of Collagen I volume fraction obtained from the immunofluorescence images and their respective position in the stiffness maps measured by Atomic Force Microscopy. Of those 400 values, the 10 highest values of Collagen I volume fraction were found, and their equivalent stiffness values matched for each sample. Then the

mean value of those maximum volume fraction of Collagen I was calculated. The calculated maximum collagen I volume fraction for non-cancerous lung ECM was 0.12058±0.04 and the one for the cancerous ECM 0.15102±0.06 with an equivalent stiffness of 8.02±3.36 kPa for non-cancerous ECM and 23.492±13.93 for the cancerous ECM. With these data, the Elastic modulus of the Collagen I fibers was calculated using the Eshelby's model with the inputs shown in Table 5.5.

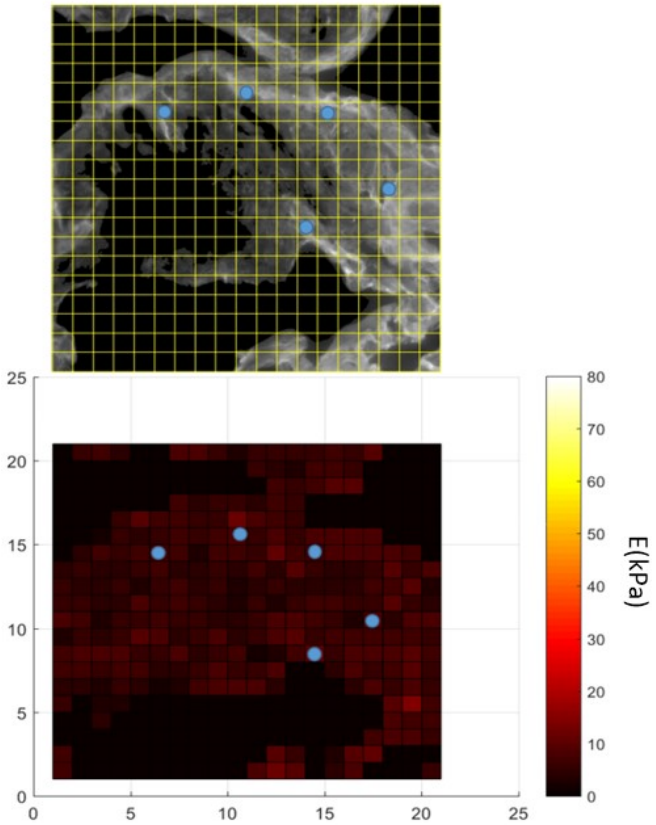

Figure 5.6 Colocalization of the higher values of Collagen I volume fraction obtained from the immunofluorescence images and their respective position in the stiffness maps measured by Atomic Force Microscopy.

Table 5.5 Inputs of the Eshelby's model used to calculate the elastic modulus of the Collagen I fibers using the volume fraction obtained from the immunofluorescence images.

Parameter	Value
Volume Fraction of fibers	0.12058 Non-cancerous 0.15120 Cancerous
E of the Collagen I	1 to 1000 kPa
E of the matrix	1 kPa
Aspect ratio of fibers	10000
Fiber Direction	Random in 3D

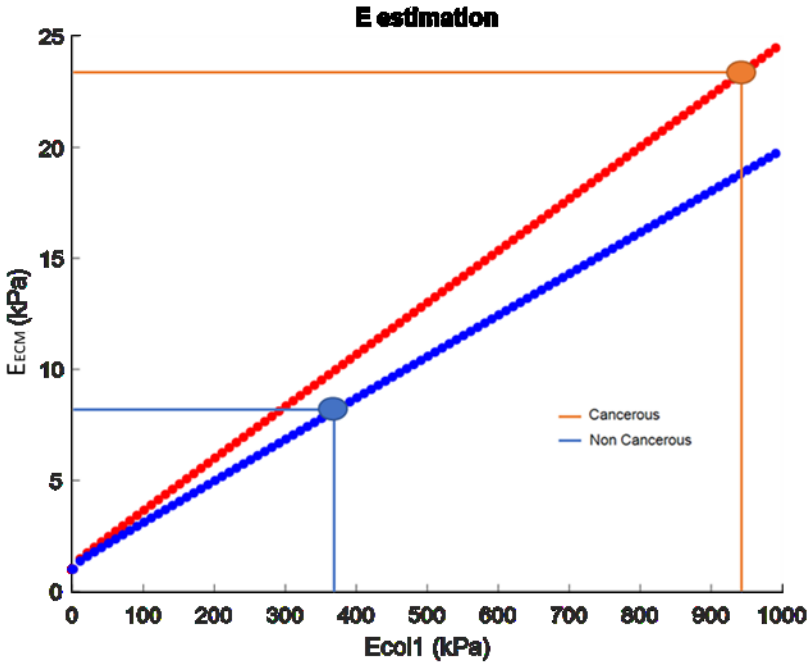

Figure 5.7 Elastic modulus of the ECM predicted by the model as a function of the elastic modulus of the Collagen I fibers for two volume fraction of fibers, 0.12058 (non-cancerous) and 0.1512 (Cancerous), with the input parameters described in Table 5.5. E_{ColI} was calculated from the average modulus measured with AFM (blue and orange dots).

Figure 5.7 shows the E_{ECM} predicted by the model as a function of E_{Coll} for the volume fraction of fibers corresponding to cancerous and non-cancerous ECM. By comparing the predicted and measured mean values of cancerous and non-cancerous E_{ECM}, the values of E_{Coll} were obtained. The resulting values for the elastic modulus of Collagen I was of 365 kPa for non-cancerous ECM and of 948kPa for cancerous ECM. This calculation was made supposing that the aspect ratio of the Collagen I fibers is 10000. The next step was to perform the same calculation using the aspect ratios obtained from the immunofluorescence images for "bundled" fibers.

In summary,

- In the non-cancerous ECM for a volume fraction of Collagen I of 0.12058±0.04 and a measured stiffness of 8.02±3.36 kPa, the ideal elastic modulus of the Collagen I fibers would be 365 kPa.
- In the cancerous ECM for a volume fraction of Collagen I of 0.15102±0.06 and a measured stiffness of 23.492±13.93 kPa, the ideal elastic modulus of the Collagen I fibers would be 948 kPa.

5.2.3.2 *Elastic modulus of collagen I fibers including the effect of the bundles of fibers*

Earlier in this chapter, it was explained that due to the limitations of the employed immunofluorescence imaging technique just bundled Collagen I fibers were able to be characterized. Two types of Collagen I configurations were chosen as Figure 5.4 shows:

- Bundled Collagen I fibers, with a measured aspect ratio and orientation.
- No bundled Collagen I fibers, or fibers beyond the resolution of the images.

The volume fraction of fibers used in the previous chapter refers to the total volume fraction of collagen I for cancerous and non-cancerous lung ECM. But part of the fibers were bundled. In particular, from the immunofluorescence images, it was obtained that for the two sets of 10 tests with maximum volume fraction of fibers 11.03% of the non-cancerous Collagen I and 13.9% of the cancerous Collagen I were bundled.

Thus, the model was used to characterize the effect of the aspect ratio of the bundled fibers. The volume fraction of the Collagen I bundled fibers was added based on the measured percentage, keeping the rest of the volume fraction as long fibers of aspect ratio 10000. The effect of the aspect ratio of the bundled fibers on the E_{ECM} was studied by varying the aspect ratio of the bundles from 1 to 150 in steps of 1. The input parameters are gathered in Table 5.6.

Table 5.6 Input parameters of the Eshelby's model used to study the effect of the aspect ratio of the bundled fibers on the E_{ECM}

Input Parameter	*Value*
Total volume Fraction of fibers	0.12058 Non-cancerous 0.15120 Cancerous
Percentage of Bundled fibers	11.031 Non-cancerous 13.932 Cancerous
E of the Collagen I	EColIn= 365 kPa EColIt= 948 kPa
E of the matrix	1 kPa
Aspect ratio of bundled fibers	From 1 to 150
Aspect ratio of filling fibers	10000
Fiber Direction of filling fibers and bundled fibers	Random in 3D

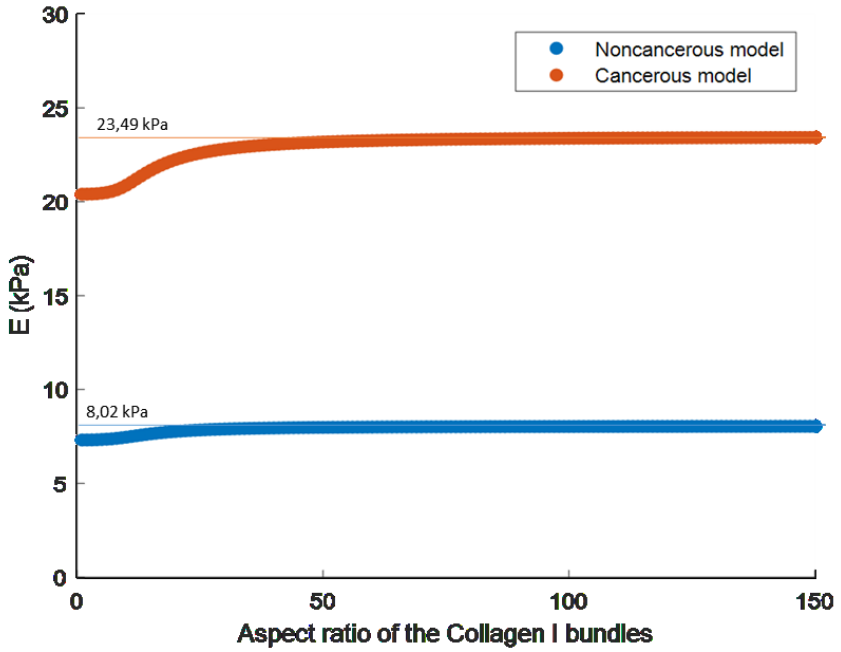

Figure 5.8 Elastic modulus of the ECM predicted by the model as a function of the aspect ratio of the Collagen I bundled fibers for cancerous and non-cancerous ECM (see input parameters in Table 5.5) The orange and blue thin lines represent the measured values of the E_{ECM}.

As we can observe in Figure 5.8, using the values of elastic modulus for the Collagen I obtained previously (365 and 948 kPa for non-cancerous and cancerous respectively), the measured mean values of cancerous and non-cancerous E match the model when the aspect ratio of the fibers is over 50. In non-cancerous ECM, the E_{ECM} ranges from 7.315 kPa for fibers of aspect ratio 1 to 8.051 kPa for fibers of aspect ratio 150. From aspect ratio 1 to 50 the value of the calculated E_{ECM} increases in a 9% being the E_{ECM} for an aspect ratio of 50 equal to 7.98 kPa. In cancerous ECM, E_{ECM} goes from 20.404 kPa for fibers of aspect ratio 1 to 23.4576 kPa for fibers of aspect ratio 150. From aspect ratio 1 to 50 the value of the

calculated E_{ECM} increases in a 13% being the E_{ECM} for an aspect ratio of 50 equal to 23.18 kPa.

For the next optimization of the elastic modulus of Collagen I fibers, the aspect ratio of the bundled Collagen I fibers had to be obtained. If the obtained aspect ratio is lower than 50, then the elastic modulus of Collagen I fibers should be characterized using the aspect ratio obtained from the immunofluorescence images.

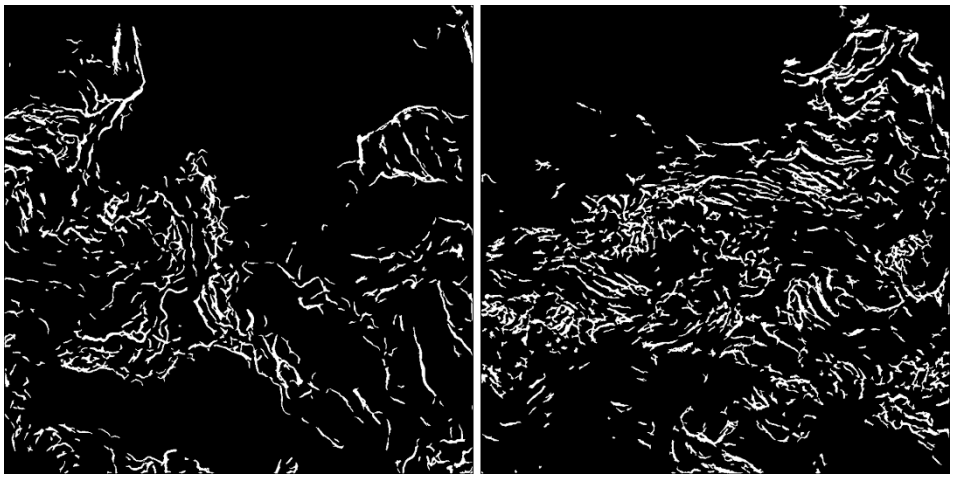

Figure 5.9 Masks of the Collagen I bundled fibers obtained from the immunofluorescence images. For the same patient, left, non-cancerous ECM. Right, cancerous ECM.

The mean aspect ratio of the Collagen I bundled fibers was obtained using the Filter Region Analyzer tool from Matlab® from the images shown in Figure 5.9 for each sample.

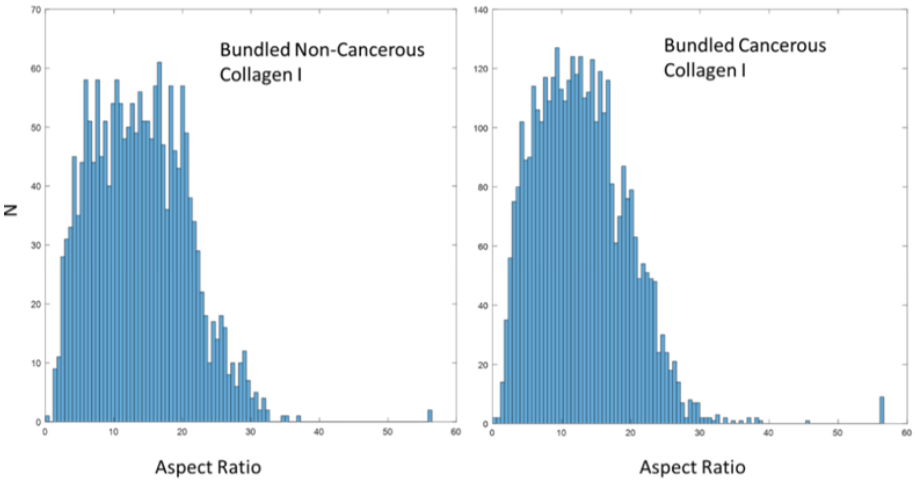

Figure 5.10 Distribution of the measured aspect ratios for all samples in cancerous and non-cancerous ECM.

The aspect ratio of all bundled fibers from all cancerous and non-cancerous fibers were obtained, giving as a result a value of 13.836±6.92 for non-cancerous fibers and 12.882±6.72 for cancerous fibers, Figure 5.10. Then, the Eshelby's model was fit to the measured aspect ratios to adjust the elastic modulus of cancerous and non-cancerous Collagen I fibers. The input parameters employed in the model are gathered in Table 5.7

Table 5.7 Input parameters used in the Eshelby's model to calculate the elastic modulus of the Collagen I fibers when using the aspect ratios of the bundled fibers.

Input Parameter	*Value*
Volume Fraction of fibers	0.12058 Non-cancerous 0.15120 Cancerous
Percentage of Bundled fibers	11.031 Non-cancerous 13.932 Cancerous
E of the Collagen I	Unknown
E of the matrix	1 kPa
Aspect ratio of bundled fibers	13.836 Non-cancerous 12.882 Cancerous
Aspect ratio of filling fibers	10000
Fiber and bundle Direction of filling fibers	Random in 3D

As can be observed in Figure 5.11, the E_{ColI} was set so that the E_{ECM} measured (8.033 kPa for non-cancerous and 23.468 for cancerous) matches the E_{ECM} predicted by the model for an aspect ratio of 13.836 and 12.882 for non-cancerous and cancerous lung ECM, respectively. The obtained E_{ColI} for non-cancerous lung ECM was 390 kPa and the obtained E_{ColI} for cancerous lung ECM was 1050 kPa.

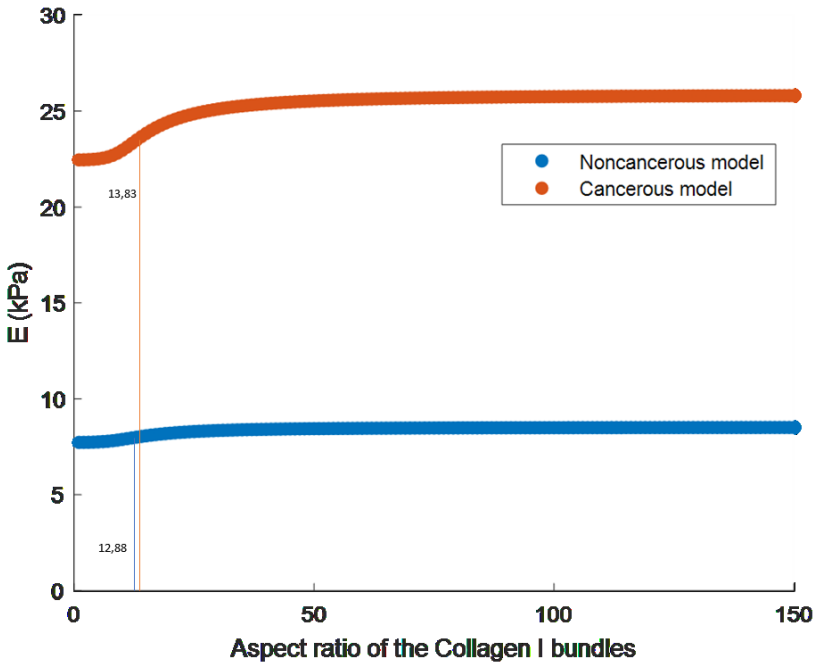

Figure 5.11 Elastic modulus of the ECM predicted by the model as a function of the aspect ratio of the Collagen I bundled fibers for cancerous and non-cancerous ECM (see input parameters in Table 5.7). The E_{Coll} has been modified to match the E_{ECM} predicted and measured by AFM for the aspect ratio of the bundled fibers. The values used for E_{Coll} are 390 and 1050 kPa for non-cancerous and cancerous, respectively.

5.3 PREDICTING THE ELASTIC MODULUS OF THE CANCEROUS AND NON-CANCEROUS LUNG ECM FROM ITS MICROSTRUCTURE

In this section, the elastic modulus of the ECM is calculated using the Eshelby´s model from the microstructural data measured from each immunofluorescence image and compared to the average elastic modulus of the ECM obtained from the measures performed on this same region by AFM. Two cases are considered:

1- Collagen I fibers randomly oriented in 3D with E_{matrix}=1kPa, E_{Coll}=390 kPa for non-cancerous ECM and E_{Coll}=1050 kPa for cancerous ECM.
2- Collagen I fibers randomly oriented in-plane with E_{Coll}=100 MPa.

5.3.1 Eshelby's model for a 3D orientation of the Collagen I fibers

The input parameters used to predict the elastic modulus of the ECM using the Eshelby´s model are collected in Table 5.8. The data obtained from the immunofluorescence images were the total volume fraction of Collagen I, the percentage of bundled fibers and the aspect ratio and orientation of the bundled fibers.

Table 5.8 Input parameters of the Eshelby's model used to calculate the elastic modulus of the extracelullar matrix based on immunofluorescence images of Collagen I in cancerous and non-cancerous lung.

Input Parameter	*Value*
Volume Fraction of fibers	The one of the measured sample
Percentage of Bundled fibers	The one of the measured sample
E of the Collagen I	EColIn=390 kPa EColIt= 1050 kPa
E of the matrix	1 kPa
Aspect ratio of bundled fibers	The one of the measured sample
Aspect ratio of filling fibers	10000
Fiber Direction of bundled fibers	The one of the measured sample
Fiber Direction of filling fibers	Random in 3D

Figure 5.12 shows the results gathered in Table 5.9 and Table 5.10.that is, the predicted and measured E_{ECM} grouped by patient. The model captures the increase of elastic modulus occurring in the cancerous region, even if for patients 6 and 7 the measured volume fraction of collagen fibers decreases for cancerous regions (Figure 4.19). This could be related to the use of two different values for the stiffness of the collagen I fibers.

Table 5.9 Data comparison between the model estimation of the elastic modulus for each non-cancerous sample and the measured mean elastic modulus of each sample

Non-Cancerous			
	Model E (kPa)	Measured E (kPa)	Error%
1	2.9064	6.0297	-52
2	5.5533	6.0972	-9
3	3.9045	4.3969	-11
4	5.1638	7.9806	-35
5	3.4052	7.4026	-54
6	5.5050	5.4505	1
7	6.0773	7.0177	-13

Table 5.10 Data comparison between the model estimation of the elastic modulus for each cancerous sample and the measured mean elastic modulus of each sample

Cancerous			
	Model E (kPa)	Measured E (kPa)	Error%
1	18.1109	13.3152	36
2	11.9804	15.1371	-21
3	24.4180	20.0018	22
4	10.3479	14.5338	-29
5	15.2324	19.6329	-22
6	4.9021	7.8513	-38
7	7.3662	19.1292	-61

Table 5.9, and Table 5.10, show the predicted and measured elastic modulus of the lung extracellular matrix and the error in the predicted value for each sample for non-cancerous and cancerous ECM respectively. It is noted that a mean absolute error of 25% and 33% are found in the prediction for non-cancerous and cancerous ECM respectively.

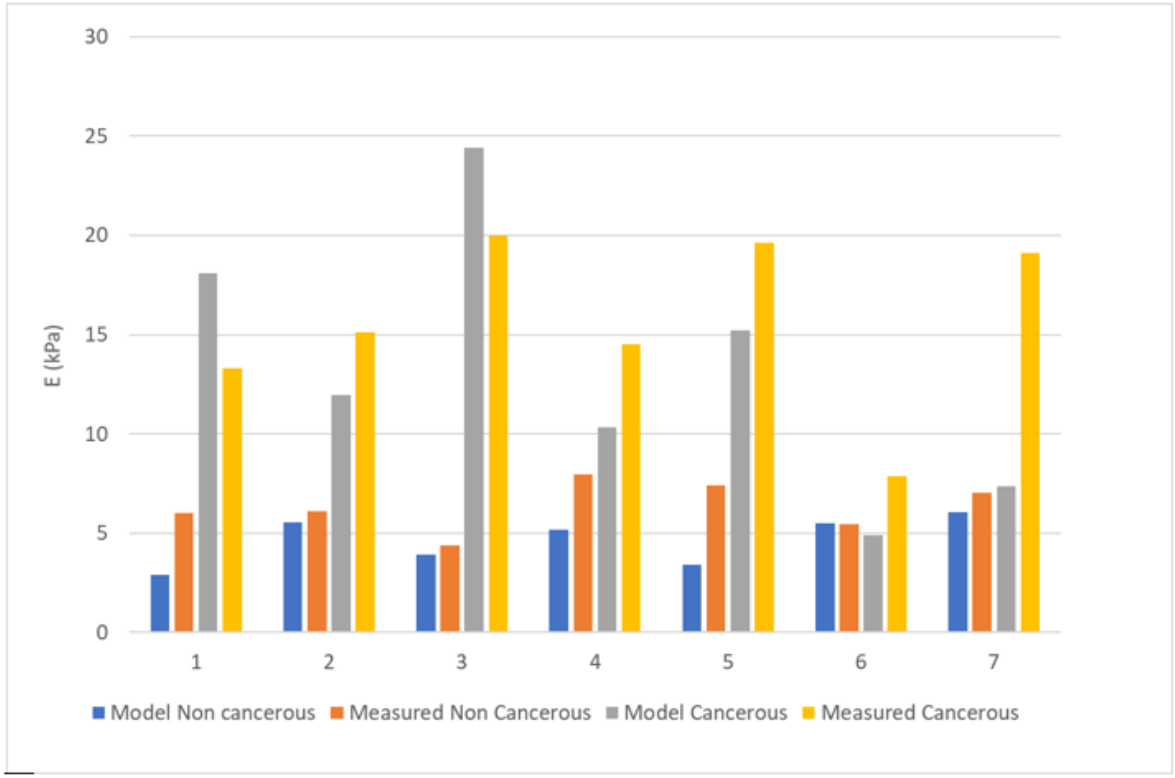

Figure 5.12 Representation of the estimated elastic modulus of cancerous and non-cancerous ECM using the Eshelby's model in seven different patients. The measured data is composed of the mean of all the indentations performed in the sample by AFM: The model data is composed from the results of the Collagen I fiber stiffens calculated from the mean Collagen I volume fraction and measured elastic modulus,

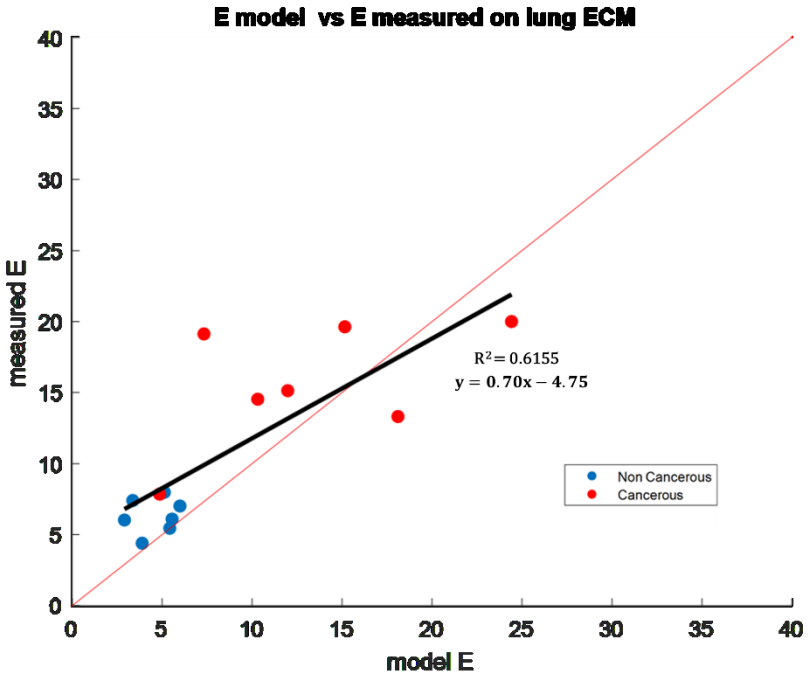

Figure 5.13 Mean measured Elastic modulus of each sample against the model estimation for each sample in cancerous and non-cancerous lung ECM. The cancerous and non-cancerous data fit a linear regression with an R2=0.6155. The red line represents the perfect match between the model estimated E and the measured E. Both axis are represented in kPa.

Figure 5.13 shows the measured against the predicted E_{ECM} for all the samples tested: non-cancerous and cancerous regions for all the patients with a correlation of R^2=0.6155.

5.3.2 Eshelby's model for a 2D orientation of the Collagen I fibers

As previously mentioned, when the collagen I fibers are randomly oriented in 3D the values obtained for the E_{ECM} using E_{Coll} reported in literature (100 MPa) are 238 times higher than the measured ones.

Moreover, the effect of the E_{matrix} is negligible in the actual volume fraction range. However, for a 2D distribution of fibers the predicted values were closer to the measured ones using an E_{matrix} of 1 kPa. Therefore, it was decided to study the effect of the elastic modulus of the matrix where the fibers are embedded for the fibers oriented randomly in-plane. For this purpose, simulations were run for a total of five different matrix stiffnesses ranging between 100 kPa and 0.01 kPa. All the input parameters of the simulations are gathered in Table 5.11

Table 5.11 Input parameters of the Eshelby's model used to study the effect of the Young modulus of the matrix embedding the collagen I fibers on the equivalent modulus of the ECM when the fibers are randomly distributed in 2D

Input Parameter	*Value*
Volume Fraction of fibers	0.001 to 0.5001
E of the Collagen I	100 MPa
E of the matrix	From 0.01 kPa to 100 kPa
Aspect ratio of fibers	10000
Fiber Direction	Random 2D (XY, see figure 5.5)

Table 5.12 Results of the estimated E_{ECM} for a 2D randomly oriented 100MPa Collagen I fibers as the volume fraction increases and the E of the matrix decreases.

E_{Matrix}	100kPa	10kPa	1 kPa	0.1 kPa	0.01kPa
fv	E_{ECM}	E_{ECM}	E_{ECM}	E_{ECM}	E_{ECM}
0.001	115.673622	20.6803218	5.74989117	1.78713687	0.5485908
0.101	635.334598	197.447709	61.179102	12.4180425	1.43549993
0.201	986.641035	309.16681	92.9590716	16.2492473	1.78570586
0.301	1356.26196	426.405286	126.173282	20.9832113	2.27569343
0.401	1794.72925	565.538596	167.292444	27.7624426	3.00928366
0.501	2361.53333	745.76741	223.345405	38.3319552	4.1911518

Table 5.12 shows the predicted E_{ECM} for different volume fractions of fibers (0.001 to 0.501) calculated for an E_{matrix} from 100 kPa to 0.01 kPa. Focusing on the range of volume fractions of collagen I between 0.001 and 0.2, that is the experimental range, we observe that for the non-cancerous ECM the measured E_{ECM} was in the range of 4 kPa to 8 kPa, which is predicted by the model for values of E_{matrix} between 0.01 kPa and 0.1 kPa. In the case of the cancerous ECM, E_{matrix} should be between 0.1 kPa and 1 kPa for the model to predict the measured values from 8 kPa to 20 kPa.

We decided to use an elastic modulus of the collagen I fibers of 100 MPa, as reported in bibliography, for all the samples and to change E_{matrix} based on the absolute minimum stiffness measured in the samples, which was of 0.043 kPa, in order to predict the experimental values for the E_{ECM}. This was done through trial and error separately for cancerous and non-cancerous samples until the average error is minimized. The fitting was done separately taking into account the results obtained for the 3D distribution and the fact that we are using a unique elastic modulus for the collagen I fibers, but we are not taking into account crosslinking or the contribution of collagen III and elastin.

The best results were obtained for the input parameters gathered in Table 5.13. A value of 0.15 kPa of E_{matrix} is used for cancerous samples and of 0.0545 kPa for non-cancerous samples. On the other hand, Table 5.14 and Table 5.15 show the corresponding values and the error in % for non-cancerous and cancerous samples, respectively. The predicted E_{ECM} showed an absolute mean error of 17.38% for the non-cancerous lung ECM and of 16.96% for the cancerous ECM.

Figure 5.14 shows the correlation between predicted and measured values of the E_{ECM} obtained for these values of E_{matrix}. Even though the model can approach the measures with an error of about 17% for non-cancerous and cancerous ECM, the correlation between the measured and the estimated E_{ECM} is not good, especially for non-cancerous samples (R^2 = 0.0369). The correlation appears to be higher on the cancerous samples, with an R^2 = 0.3587. This could also be related to the

heterogeneity of the cancerous samples, which result in a bigger span of E_{ECM} values more appropriate for a linear fitting.

Figure 5.15 shows the results gathered in Table 5.14 and Table 5.15, that is, the predicted and measured E_{ECM} grouped by patient. It should be noted that for all the patients the model captures the increase of elastic modulus occurring in the cancerous region, even if for patients 6 and 7 the measured volume fraction of collagen fibers decreases for cancerous regions (Figure 4.19). This could be related to the use of two different values for E_{matrix}.

Table 5.13 Parameters of the Eshelby's model to calculate the estimated elastic modulus of the extracelullar matrix based on immunofluorescence images of Collagen I in cancerous and non-cancerous lung.

Input Parameter	*Value*
Volume Fraction of fibers	The one of the measured sample
Percentage of Bundled fibers	The one of the measured sample
E of the Collagen I	ECoII=100 MPa
E of the matrix	0.15 kPa Cancerous Matrix 0.0545 kPa Non-cancerous Matrix
Aspect ratio of bundled fibers	The one of the measured sample
Aspect ratio of filling fibers	10000
Fiber Direction of bundled fibers	The one of the measured sample
Fiber Direction of filling fibers	Random in 2D

Table 5.14 Data comparison between the model estimation of the elastic modulus for each non-cancerous sample and the measured mean elastic modulus of each sample

Non-Cancerous			
	Model E (kPa)	Measured E (kPa)	Error%
1	5.3569	6.0297	-11
2	6.6520	6.0972	9
3	5.9559	4.3969	35
4	6.5412	7.9806	-18
5	5.6965	7.4027	-23
6	6.6683	5.4505	22
7	7.1976	7.0177	2

Table 5.15 Data comparison between the model estimation of the elastic modulus for each cancerous sample and the measured mean elastic modulus of each sample

Cancerous			
	Model E (kPa)	Measured E (kPa)	Error%
1	17.5560	13.3152	32
2	15.1636	15.1371	0.2
3	20.2805	20.0018	1
4	14.3479	14.5338	-1
5	16.4349	19.6329	-16
6	10.2651	7.8514	31
7	12.5397	19.1293	-34

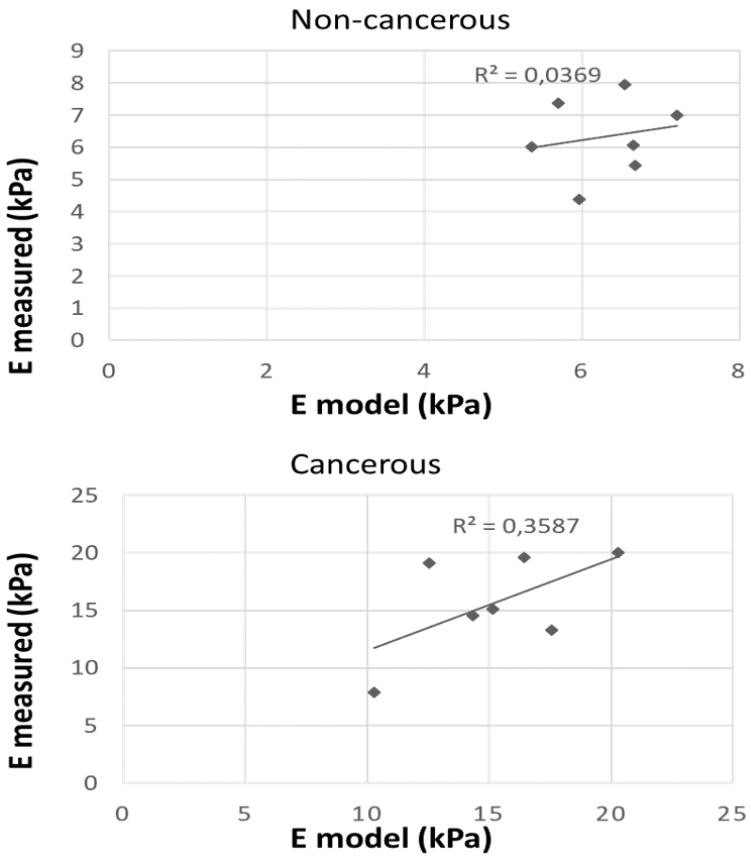

Figure 5.14 Correlation between the estimation of the model and the measured E_{ECM} for non-cancerous and cancerous samples. E_{ECM} is the average ECM stiffness measured from each indentation map.

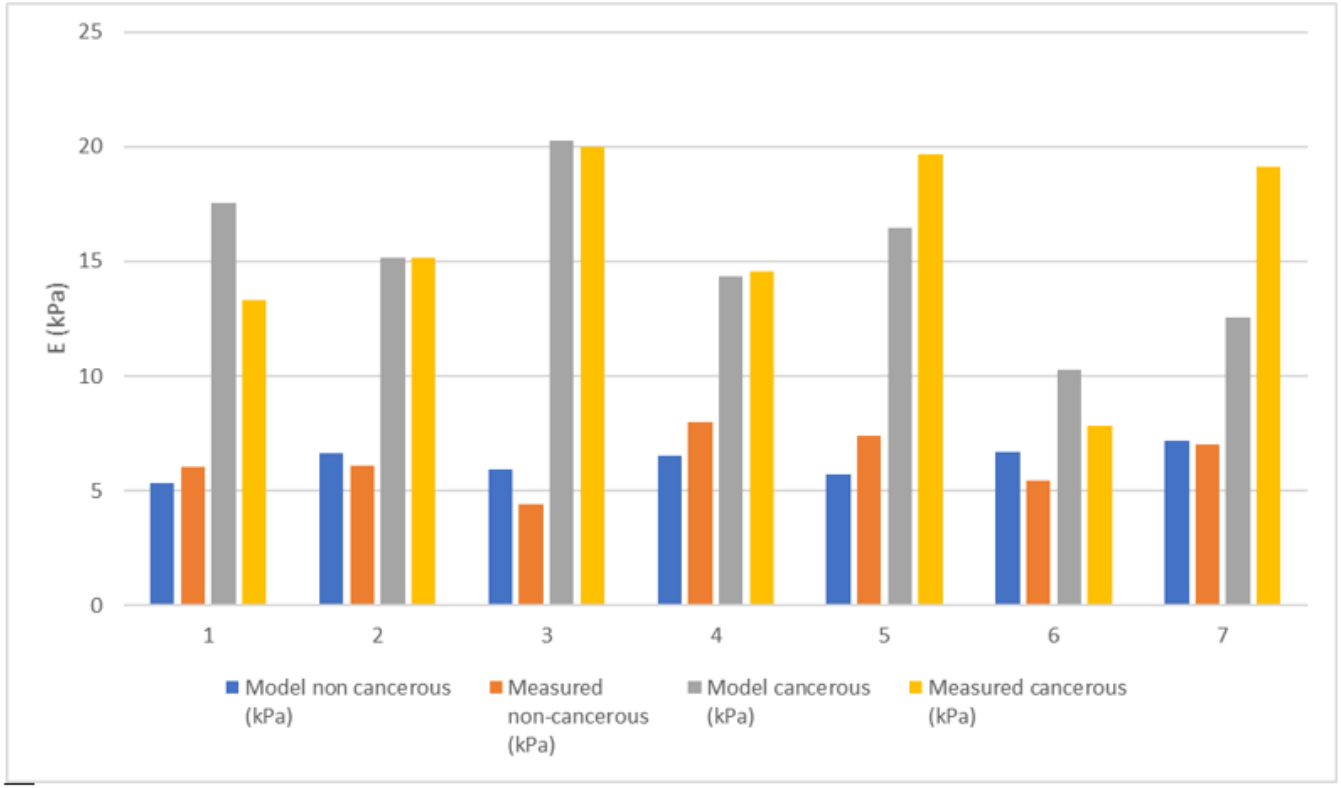

Figure 5.15 Representation of the estimated elastic modulus of cancerous and non-cancerous ECM using the Eshelby's model in seven different patients. The measured data is composed of the mean of all the indentations performed in the sample by AFM, and the model data is the resulting from the 2D randomly oriented 100MPa Collagen I fibers.

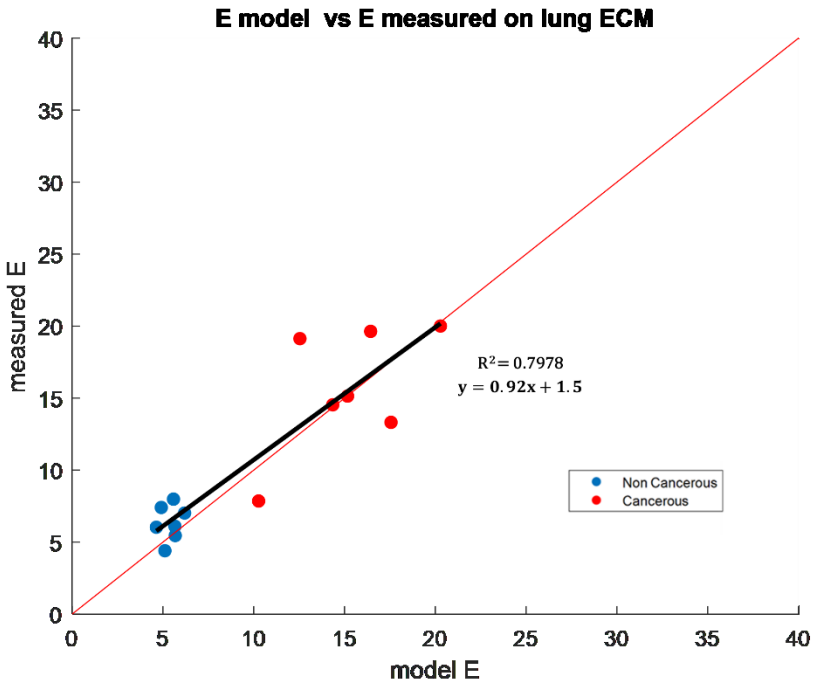

Figure 5.16 Mean measured Elastic modulus of each sample against the model estimation for each sample in cancerous and non-cancerous lung ECM. The red line represents the perfect match between the model estimated E and the measured E. Both axis are represented in kPa.

Figure 5.16. shows the measured against the predicted E_{ECM} for all the samples tested: non-cancerous and cancerous regions for all the patients. There exists a good correlation, up to an R^2 = 0.7978.

All these results show that if we consider the fibers randomly oriented in-plane the values of the elastic modulus we have to use for the matrix and the collagen I fibers to predict the E_{ECM} are in the range reported in bibliography and the measured by AFM in this work (E_{Coll}=100-360 MPa, minimum E_{ECM}=0.045 kPa).

5.3.3 Eshelby's model for a 2D orientation of the Collagen I fibers with volume fractions relative to the sample

Taking into account the results from chapter 4, we decided to repeat the calculation performed in the previous section for a 2D orientation of the fibers using the volume fraction calculated with the maximum values of intensities measured in each sample, following the next equation:

$$Vf = \frac{\sum ICoII}{NpECM*(ImaxrCoII+ImaxrCoIIII+ImaxrElastin)} \quad (21)$$

Where V_f is the volume fraction of collagen I, the ICoII is each of the intensities of CoII protein in that quadrant, ImaxCoII, ImaxCoIIII and ImaxElastin are the maximum intensity measured for CollagenI, CollagenIII and Elastin on that sample and NpECM is the number of pixels where there is at least one of the three proteins.

We use the procedure described in section 5.3.2 in order to determine, through trial and error, the values of the elastic modulus of the matrix to be used to minimize the errors in the predicted average values of the E_{ECM}. This is done separately for the non-cancerous and cancerous samples. The best results are obtained for an E_{matrix}=0.05 kPa for the non-cancerous samples and Ematrix=0.12 kPa for the cancerous samples. Table 5.16 gathers the input parameters used in the Eshelby´s model to calculate the E_{ECM} from the microstructural data derived from the immunofluorescence images.

Table 5.16 Input parameters of the Eshelby's model used to calculate the estimated elastic modulus of the extracelullar matrix based on immunofluorescence images of Collagen I in cancerous and non-cancerous lung.

Input Parameter	*Value*
Volume Fraction of fibers	The one of the measured sample
Percentage of Bundled fibers	The one of the measured sample
E of the Collagen I	ECoII=100 MPa
E of the matrix	0.12 kPa Cancerous Matrix 0.05 kPa Non-cancerous Matrix
Aspect ratio of bundled fibers	The one of the measured sample
Aspect ratio of filling fibers	10000
Fiber Direction of bundled fibers	The one of the measured sample
Fiber Direction of filling fibers	Random in 2D

The obtained results are gathered in Table 5.17 for the non-cancerous ECM and Table 5.18 for the cancerous ECM. The predicted E_{ECM} showed an absolute mean error of 14.48% for the non-cancerous lung ECM and 11.152% for the cancerous ECM, which is slightly better than the error of around 1% obtained in the previous section.

The data in Table 5.17 and Table 5.18 are represented in Figure 5.17. The correlation values between the measured E and the estimated E are of R^2 =0.5167 for non-cancerous samples and of R^2 =0.8527 for the cancerous samples.

Table 5.17 Data comparison between the model estimation of the elastic modulus for each non-cancerous sample and the measured mean elastic modulus of each sample

Non-Cancerous			
	Model E (kPa)	Measured E (kPa)	Error%
1	5.71437075	6.0297	5
2	6.79657124	6.0972	-11
3	5.92399882	4.3969	-35
4	7.27870292	7.98064653	9
5	7.51733626	7.40266387	-2
6	6.90391794	5.45053503	-27
7	7.92712838	7.01774328	-13

Table 5.18 Data comparison between the model estimation of the elastic modulus for each cancerous sample and the measured mean elastic modulus of each sample

Cancerous			
	Model E (kPa)	Measured E (kPa)	Error%
1	17.4963216	13.3152	-31
2	15.2584365	15.13711	-1
3	20.4566923	20.0018	-2
4	15.3375788	14.5338461	-6
5	19.8861324	19.6329134	-1
6	10.213411	7.85135201	-30
7	17.8509698	19.1292895	7

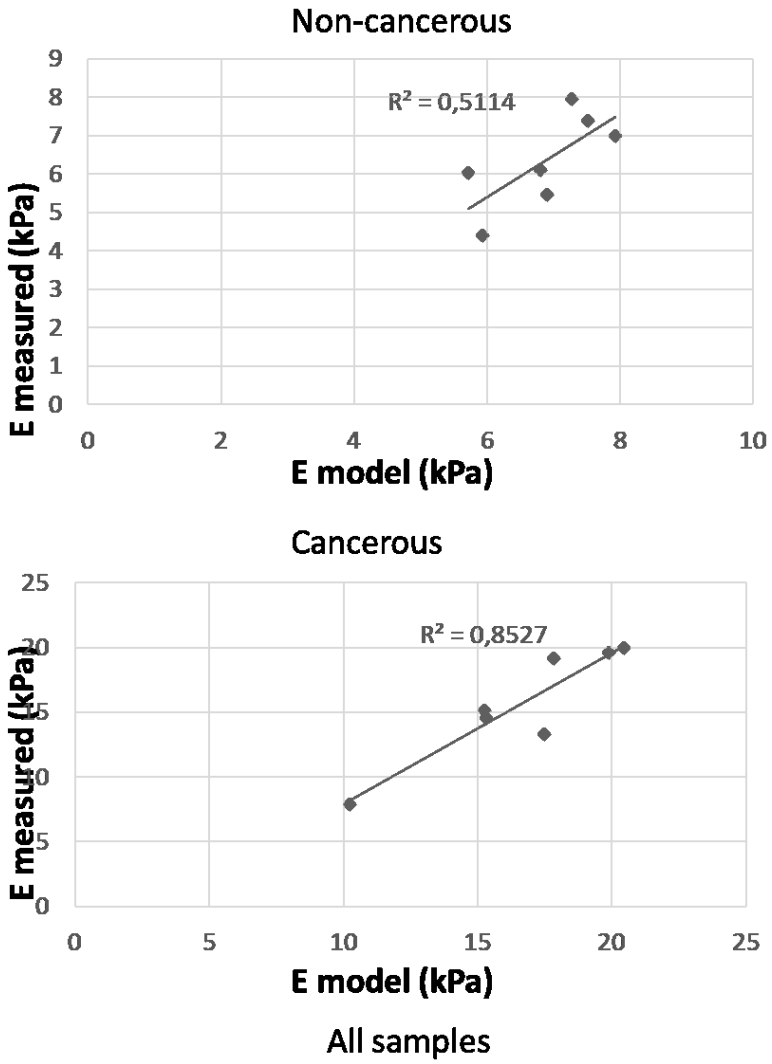

Figure 5.17 Correlation between the estimation of the model and the measured E for non-cancerous, cancerous and all the samples.

Figure 5.18 represents the predicted and measured E_{ECM} for the non-cancerous and cancerous regions for each patient. As in the previous

case, the model captures the increase of stiffness in the cancerous region for all the patients.

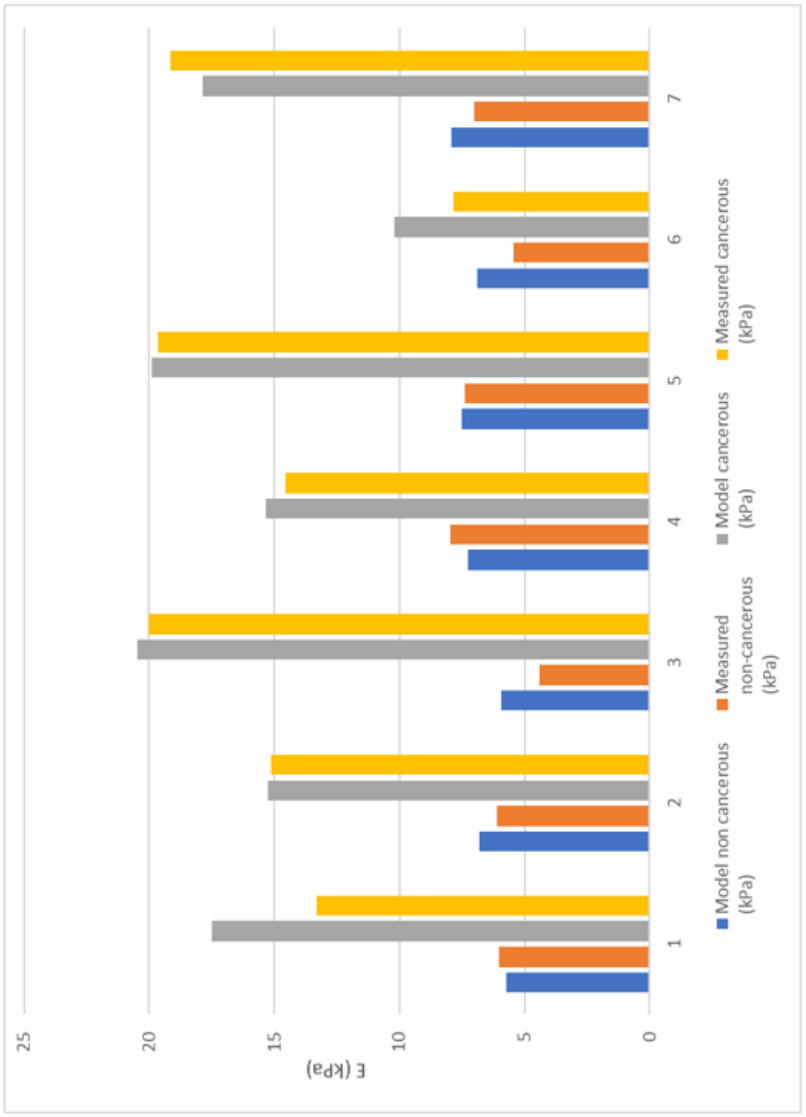

Figure 5.18 Representation of the estimated elastic modulus of cancerous and non-cancerous ECM using the Eshelby's model in seven different patients. The measured data is composed of the mean of all the indentations performed in the sample by AFM, and the model data is the resulting from

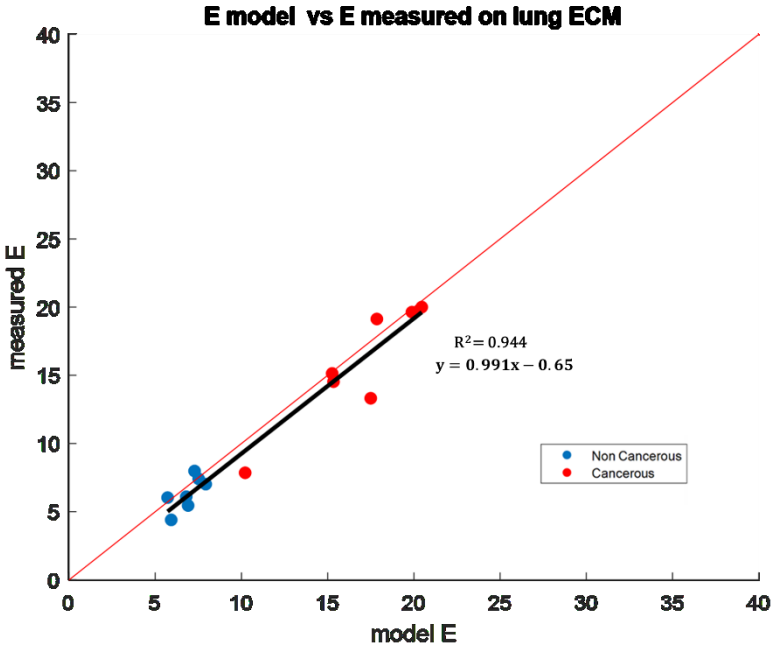

Figure 5.19 scatterplot of the mean measured Elastic modulus of each sample against the model estimation for each sample in cancerous and non-cancerous lung ECM. The red line represents the perfect match between the model estimated E and the measured E. Both axis are represented in kPa.

Finally, Figure 5.19 shows the measured E_{ECM} versus de predicted E_{ECM} for all the measured samples. A correlation coefficient of R^2 = 0.944 is obtained with a slope of 0.991. These are the best results obtained with the model in this work.

5.4 DISCUSSION

5.4.1 Eshelby's model for a 3D orientation of the Collagen I fibers

A model for the estimation of the elastic modulus of cancerous and non-cancerous ECM has been developed based on Eshelby's inclusions model. The model is fed with different input parameters, such as the volume fraction of the contained inclusions (Collagen I fibers) which was calculated using the maximum intensity value from all the samples as in equation (20), the aspect ratio of the inclusions (obtained from the immunofluorescence images for the bundled fibers and 10000 for the non-bundled fibers), the elastic modulus of the fibers (calculated from the experimental data), the fiber orientation (obtained from the experimental data) and the elastic modulus of the matrix.

For the measured volume fractions a 3D oriented fiber distribution did not match the results obtained experimentally for the collagen I stiffness values mentioned in bibliography (100-360MPa [6]) for any matrix stiffness as is shown in Table 5.2. To fit the physiological range of collagen I stiffness the volume fraction should be lower than 0.001 and we know that just collagens constitute the 60% of the dry lung weight [27]. So, the stiffness of the collagen I cancerous and non-cancerous fibers were estimated, resulting in 390 kPa and 1050 kPa respectively. The difference between the values is to mimic the effects of the fiber crosslinking which was not measured in this work and the model does not consider it.

With these data values an estimation of the elastic modulus of the non-cancerous and cancerous ECM has been achieved with an average error

of a 25.08% and 32.74% respectively. The values between the model estimation and the measured stiffness correlated with an R^2=0.61.

5.4.2 Eshelby's model for a 2D orientation of the Collagen I fibers, volume fraction calculated from the absolute protein intensity values.

Later the inputs of the model were changed to suppose a 2D fiber distribution. For a random 2D orientation of the collagen I fibers we observed that, for the volume fraction range measured and collagen I fibers of E= 100 MPa, the model Estimated an E inside the ranges of the measured E, Table 5.12. This happened for a model matrix with an E between 0.01 and 1 kPa being the lowest measured experimental value of 0.043 kPa. This would also justify the calculation of the volume fraction, since the model matches the experimental E measurements with physiologically coherent collagen I fiber stiffness. In chapter 4 we did not observe any correlation between the elastin and collagen III and the measured E. So, the model was just developed for collagen I.

For these inputs, the E_{matrix} of the cancerous and non-cancerous ECM was supposed to have a different value, being the cancerous E_{matrix} stiffest. This could be balancing the effect of the crosslinking, as we have mentioned before, previous works correlate the effect of a higher crosslinking ratio with a higher stiffness [24]–[26]. Also, in chapter 4, we observed that the relationship between the mean volume fraction and the mean measured E showed a correlation of R^2=0.274 for the collagen I. The differences in the $E_{matrix,}$ the directionality of the fibers and the aspect ratio of the fiber bundles that were used in the model seem to increase that correlation. If the model worked proportionally just with

the volume fraction the correlation would not increase that much, so the rest of the data increases the estimation of the E_{ECM}.

The model estimated the E of the cancerous and non-cancerous ECM with an absolute mean error of around 17% for an E_{matrix}=0.15 kPa for the cancerous ECM and a E_{matrix} =0.054 kPa for the non-cancerous ECM showing a correlation of R^2=0.79.

5.4.3 Eshelby's model for a 2D orientation of the Collagen I fibers with volume fractions relative to the sample

As was concluded in chapter 4, calculating the protein volume fraction from the highest values of intensity measured on each sample showed a better correlation of the volume fraction estimation and the measured E on the samples. Therefore, the model was run using as input data the volume fraction calculated as explained. The differences in the E_{matrix} , the directionality of the fibers and the aspect ratio of the fiber bundles that were used in the model seem to increase that correlation.So, The E_{matrix} was adjusted to E_{matrix}= 0.05 for the non-cancerous ECM, and E_{matrix}= 0.12 for the cancerous ECM..The model estimation showed a mean absolute error of 14.48% for the non-cancerous lung ECM and 11.15% for the cancerous ECM with a correlation of R^2=0.944. This result shows that calculating the volume fraction with the maximum measured protein intensity on each sample can increase even more the correlation. These input parameters of the model showed the best results.

Therefore, this model based on Eshelby´s inclusions can predict the behavior of the lung cancerous and non-cancerous ECM based on the

Collagen I volume fraction obtained from immunofluorescence images using input parameters that match the physiological conditions, also the aspect ratio and orientation of the fibers obtained from the images increase the correlation shown in chapter 4 (R^2=0.6) which just related the volume fraction with the measured E. In chapter 4 we did not observe any correlation between the elastin and collagen III and the measured E, no relationship was found between the samples with higher error% and the collagen III and elastin volume fractions. Justifying that the model was just developed for collagen I.

5.5 CONCLUSIONS

A model based on Eshelby's inclusions problem has been developed to predict the elastic modulus of the cancerous and non-cancerous extracellular matrix.

When the fibers are distributed in 3D, the model overestimates the measured results for physiological values of the collagen I fibers elastic modulus (100 MPa) and the calculated collagen I volume fractions on the samples. Thus, an estimation of the elastic modulus of the cancerous and non-cancerous collagen I fibers had to be made based on the calculated values of volume fraction and measured E of the lung ECM. The model estimated the E of the non-cancerous and cancerous lung ECM with a mean absolute error of 25.08% and 32.74% respectively, fitting a linear regression with R^2=0.6155 for a value of E_{coll}= 390 kPa for the non-cancerous ECM and a value of E_{coll}= 1050 kPa for the cancerous ECM.

Being these two values of the collagen I E, much lower than the bibliographic data, 100 MPa.

When the fibers are distributed in 2D, the model can predict the measured E of the ECM within the range of physiological stiffness parameters of the collagen I. When the fibers are distributed in 2D, the effect of the crosslinking and other stiffening mechanisms which were not measured, are reflected in the E of the model matrix, being the matrix of the cancerous ECM (E_{matrix} = 0.15 kPa) higher than the non-cancerous ECM(E_{matrix} = 0.045 kPa). The model estimation is better for the fibers distributed in 2D, with a mean absolute error 17% for both cancerous and non-cancerous ECM fitting a linear regression with R^2=0.79.

Finally, the model is run using as input data the volume fraction calculated from the maximum protein intensity value on each sample. The best results were obtained for an E_{matrix}=0.12 kPa for the cancerous ECM and an E_{matrix} =0.05 kPa for the non-cancerous ECM, with a mean absolute error of 14.48% for the non-cancerous lung ECM and 11.15% for the cancerous ECM and a correlation between measured and predicted elastic modulus of R^2=0.944.

Previously, the work of Simha et al.[23] predicted using a composites model theory relating cartilage tissue microstructure to macroscopic material stiffness. This model based on Eshelby´s inclusions problem can predict the E_{ECM} of the lung cancerous and non-cancerous ECM based on the Collagen I volume fraction, orientation and fiber aspect ratio obtained from immunofluorescence images and stiffness parameters

(100MPa) that match the physiological conditions, assuming a 2D in-plane distribution of the collagen I fibers.

5.6 BIBLIOGRAPHY

[1] F.C. Campbell, "Introduction to Composite Materials," in *Structural Composite Materials*, 2010.

[2] E. D. Hay, "Extracellular matrix.," *J. Cell Biol.*, vol. 91, no. 3 Pt 2, pp. 205s-223s, Dec. 1981.

[3] J. A. Weiss and J. C. Gardiner, "Computational modeling of ligament mechanics.," *Crit. Rev. Biomed. Eng.*, vol. 29, no. 3, pp. 303–371, 2001.

[4] G. Burgstaller, B. Oehrle, M. Gerckens, E. S. White, H. B. Schiller, and O. Eickelberg, "The instructive extracellular matrix of the lung: Basic composition and alterations in chronic lung disease," *Eur. Respir. J.*, vol. 50, no. 1, 2017.

[5] F. T. Bosman and I. Stamenkovic, "Functional structure and composition of the extracellular matrix," *J. Pathol.*, vol. 200, no. 4, pp. 423–428, 2003.

[6] D. Marcos-Gómez, J. Ching-Lloyd, M. R. Elizalde, W. J. Clegg, and J. M. Molina-Aldareguia, "Predicting the thermal conductivity of composite materials with imperfect interfaces," *Compos. Sci. Technol.*, vol. 70, no. 16, pp. 2276–2283, 2010.

[7] T. R. Society, R. Society, and P. Sciences, "Eshelby1957-1."

[8] T. W. Clyne and P. J. Withers, *An Introduction to Metal Matrix Composites*. Cambridge University Press, 1993.

[9] T. Mori and K. Tanaka, "Average stress in matrix and average elastic energy of materials with misfitting inclusions," *Acta Metall.*,

vol. 21, no. 5, pp. 571–574, 1973.

[10] Y. Benveniste, “A new approach to the application of Mori-Tanaka’s theory in composite materials,” *Mech. Mater.*, vol. 6, no. 2, pp. 147–157, 1987.

[11] M. McLAUGHLIN and T. R. CHEATHAM, “Effects of Communication Isolation on Job Satisfaction of Bank Tellers: a Research Note,” *Hum. Commun. Res.*, vol. 3, no. 2, pp. 171–175, 1977.

[12] A. M. Weber, L., C. Fischer, “On the influence of the shape of randomly oriented, non- conducting inclusions in a conducting matrix on the effective electrical conductivity L.,” *Acta Mater.*, vol. 51, pp. 495–505, 2003.

[13] L. Weber, J. Dorn, and A. Mortensen, “On the electrical conductivity of metal matrix composites containing high volume fractions of non-conducting inclusions,” *Acta Mater.*, vol. 51, no. 11, pp. 3199–3211, 2003.

[14] R. Tavangar, J. M. Molina, and L. Weber, “Assessing predictive schemes for thermal conductivity against diamond-reinforced silver matrix composites at intermediate phase contrast,” *Scr. Mater.*, vol. 56, no. 5, pp. 357–360, 2007.

[15] MARKUS R. OWEN and MARK A. LEWIS, “THE MECHANICS OF LUNG TISSUE UNDER HIGH-FREQUENCY VENTILATION,” *Soc. Ind. Appl. Math.*, vol. 61, no. 5, pp. 1731–1761, 2001.

[16] J. B. West and F. L. Matthews, “Stresses, strains, and surface pressures in the lung caused by its weight.,” *J. Appl. Physiol.*, vol. 32, no. 3, pp. 332–345, 1972.

[17] R. K. LAMBERT and T. A. WILSON, “a Model for the Elastic Properties of the Lung and Their Effect on Expiratory Flow,” *J. Appl. Physiol.*, vol. 34, no. 1 (JANUARY, 1973), pp. 34–48, 1973.

[18] S. J. Lai-Fook, “Lung parenchyma described as a prestressed compressible material,” *J. Biomech.*, vol. 10, no. 5–6, pp. 357–365, 1977.

[19] A. Adler and R. Guardo, “Electrical impedance tomography: Regularized imaging and contrast detection,” *IEEE Trans. Med. Imaging*, vol. 15, no. 2, pp. 170–179, 1996.

[20] Q. Grimal, S. Naili, and A. Watzky, “A study of impact wave propagation in the thorax,” *Mech. Res. Commun.*, vol. 29, no. 2–3, pp. 73–80, 2002.

[21] P. Dutov, O. Antipova, S. Varma, J. P. R. O. Orgel, and J. D. Schieber, “Measurement of elastic modulus of collagen type i single fiber,” *PLoS One*, vol. 11, no. 1, pp. 1–13, 2016.

[22] T. Ushiki, “Collagen fibers, reticular fibers and elastic fibers. A comprehensive understanding from a morphological viewpoint,” *Archives of Histology and Cytology*, vol. 65, no. 2. pp. 109–126, 2002.

[23] N. K. Simha, M. Fedewa, P. H. Leo, J. L. Lewis, and T. Oegema, “A composites theory predicts the dependence of stiffness of cartilage culture tissues on collagen volume fraction,” *J. Biomech.*, vol. 32, no. 5, pp. 503–509, 1999.

[24] K. R. Levental *et al.*, “Matrix Crosslinking Forces Tumor Progression by Enhancing Integrin Signaling,” *Cell*, vol. 139, no. 5, pp. 891–906, 2009.

[25] M. R. Ng and J. S. Brugge, “Previews A Stiff Blow from the Stroma : Collagen Crosslinking Drives Tumor Progression,” *Cancer Cell*, vol. 16, no. 6, pp. 455–457, 2009.

[26] D. T. Butcher, T. Alliston, and V. M. Weaver, “A tense situation: Forcing tumour progression,” *Nat. Rev. Cancer*, vol. 9, no. 2, pp. 108–122, 2009.

[27] M. R. Lang, G. W. Fiaux, M. Gillooly, J. A. Stewart, D. J. S. Hulmes, and D. Lamb, “Collagen content of alveolar wall tissue in emphysematous and non-emphysematous lungs,” *Thorax*, vol. 49, no. 4, pp. 319–326, 1994.

6

A FUNCTIONAL PLATFORM WITH TUNABLE STIFFNESS FOR THE STUDY OF 3D SINGLE CELL-ECM INTERACTIONS BASED ON METHACRYLATE HYALURONIC ACID HYDROGELS

In order to study cell-ECM interactions a platform with tunable stiffness made of methacrylate and hyaluronic acid hydrogels has been developed. Hyaluronic Acid hydrogels have been crosslinked with dithiothreitol to mimic the lung ECM, since their stiffness can be tuned by changing the Hyaluronic Acid concentration and crosslinker percentage. Ranges between 200 Pa and 19 kPa have been achieved for 3% wt. hydrogels. A rotatory platform set-up has been designed to obtain a homogeneous 3D cell distribution throughout the hydrogels. This set-up not only prevents the cells from pelleting at the bottom of the hydrogel, but also stops the cell migration towards the bottom or walls of the sample holder due to durotactic effects. 2.5D cell migration of A549 and H1299 cell lines was measured for a single focal plane, the results showed that cells can migrate towards hydrogels up to 6 kPa following a random path, what confirms that cells are not migrating motivated by durotactic effects that the stiffer parts of the platform such as the glass or the PDMS could generate.

6.1 STATE OF THE ART

Cells respond to the organization and mechanics of the tissues at subcellular [1], cellular [2] and multicellular [3] level, through interactions between the cell membrane and the substrate. This process is called mechanotransduction [4], which is the ability of living cells to sense mechanical forces applied and transduce this mechanical signal into a biological response [5]. The way in which cells sense and respond to the mechanical environment is complex and comes from the integration of the mechanical properties of the extracellular matrix (ECM) and the cellular cytoskeleton (CSK) [6]. In particular, the manner in which cells migrate and respond to their three-dimensional environment is the result of a complex and multiscale process integrating subcellular components of the CSK and the ECM of the tissue [7]. These mechanical forces play essential roles in many cellular processes, such as division, growth, deformation, adhesion, migration, remodeling and cell-cell interactions [8]. Cells can sense the stiffness of the substrate in a range from 0.1 to 25kPa [9] at least through integrin adhesion receptors [10]. For example, stem-cells have the ability to respond to the elasticity of the substrate showing different phenotypes accordingly [9].

Different tissues and organs show different mechanical properties, from soft tissues with low elastic modulus (E) such as fat (0.02 kPa) , brain (0.2-1 kPa) or liver (0.64kPa), to stiffer tissues such as cardiac muscle (20-150 kPa), articular cartilage (950 kPa) [11], compact bone (11,5 GPa) [12] or tooth dentin (100 GPa) [13]. There are several natural and synthetic biomaterials that can be used to mimic the ECM of physiological tissues

for the study of these cell-cell and cell-ECM interactions in 3D such as Collagen, Alginate or Hyaluronic Acid.

Collagen is the primary organic constituent of native tissues, most of the collagen in the human body is fibrillar. Type I collagen is the most common type and is the major structural component of many tissues[14]. Collagen hydrogels are mostly synthesized by increasing the temperatures and pH to initiate the collagen fibrils self-assembly [15]. This reaction can occur in presence of cells or culture medium[16]. The biomimetic properties of t collagen hydrogels are its most important advantage: they show cytocompatibility, cells adhere to them without the addition of any other component and they present a natural viscoelastic environment for the cells [17]. The most remarkable limitation of the collagen hydrogels is their lack of tuneability in the physiological stiffness scale, since it is difficult to synthesize hydrogels with a young modulus higher than 1 kPa. Collagen hydrogels have been used to study 3D directional migration of cancer stem cells [18].

Alginate is a polysaccharide derived from algae that has been used in industries as food, textiles and pharmaceuticals. It has the ability to form hydrogels via ionic-crosslinking, which is an advantage that makes it easy to encapsulate cells within. Alginate´s ionic crosslinks are formed by using divalent cations such as calcium, magnesium or barium to promote the formation of ionic bridges between alginate G units[19]. Alginate hydrogels must be modified with adhesive ligands to enable cell attachment. The stiffness of alginate hydrogels can be tuned from 5kPa to 110kPa [20].

Hyaluronic Acid (HA) is a nonsulfated glycosaminoglycan which is composed of a repeating disaccharide unit of glucuronate and N-acetylglucosamine. HA can be found in many tissues, such as skin, cartilage or brain, and it plays an important role in development, wound healing and disease [21]. HA presents many important advantages as a hydrogel platform, as can be its biological relevance or chemical tunability. HA can be modified to present functional groups enabling a range of different crosslinking chemistries. This permits the HA to create a range of hydrogel systems that can be crafted as 2D films, 3D free-swelling hydrogels, nanofibers and as injectable materials.

When comparing cancerous and healthy tissues, changes in the mechanical properties between both tissues can be found. In the case of mammary tumors, differences in tissue stiffness are related to increased deposition and crosslinking of collagen type I, and the stiffness can increase from 100–400 Pa up to 1–5 kPa when comparing normal and cancerous mammary tissue [22]. Also, the ECM stiffness is a key in cancer behavior. Changes of the stiffness of the ECM have influence on cell proliferation, evasion of growth suppression, death resistance, replicative immortality, induced angiogenesis and initiation of invasion and metastasis, originally described as the hallmarks of cancer by Hanahan and Weinberg [23].

Due to the limitations of the three previous materials, the lack of a stiffness range for the collagen hydrogels and the difficulty of the cells to attach alginate hydrogels In this work we have aimed to create a

platform to study single cell-ECM interactions in a 3D microenvironment that mimic the mechanical properties of the physiological ECM. Methacrylate Hyaluronic Acid (MeHA) hydrogels have been chosen since HA is a natural ECM component and HA hydrogels have stiffness tunability, making them able to cover a high spectrum of physiological stiffnesses. Besides, they can be modified to present different functional groups to allow cell-ECM interactions.

6.2 HA HYDROGEL SYNTHESIS

For the HA hydrogel synthesis, the first step is to create methacrylate groups which are going to act as binding points for the crosslinker and the different types of cell-adhesion proteins that are going to be bonded to the hydrogel.

6.2.1 Hyaluronic Acid Methacrylate synthesis.

HA-metrhacrylate (MeHA) was first synthesized as described by . HA of a nominal molecular weight of 60 KDa (LIfecore Technologies) was dissolved at 1 wt% in deionized water, then and drop by drop, a relative to the HA disaccharide repeat unit six-fold molar excess of methacrylic anhydride (Sigma) was added to the solution. This was performed inside a 4°C refrigerator while keeping the solution continuously stirring. The pH of the two-phase reaction was maintained over 8 pH after every methacrylic anhydride drop was added by adding enough 5M NaOH volume to the solution. After adding all the methacrylic anhydride, the solution was kept overnight at least at 8 pH to let the reaction finish. The product was then isolated by adding the solution to a five-fold volumetric excess of cold acetone, then centrifugated and the precipitated part and

the liquid part were separated. After that, the precipitated part of the mixture was redissolved in deionized water, frozen and lyophilized. The powder obtained by the lyophilization was a 60% degree of methacrylated hyaluronic acid.

6.2.2 Hyaluronic Acid Methacrylate groups functionalization

Prior to the hydrogel synthesis, to avoid that the methacrylate groups could be saturated with the thiol groups from the DTT crosslinker, the cell adhesion protein was added to the MeHA. 1 mM RGD peptide was added by vortexing for 2 h at room temperature prior to DTT crosslinking and gelation in order to ensure that crosslinking did not compete with peptide conjugation.

6.2.3 Hyaluronic Acid Methacrylate hydrogel synthesis

To obtain crosslinked HA hydrogels, the MeHA polymers and the crosslinker DL-dithiothreitol (DTT) were dissolved in an aqueous solution, that was cell culture media. Then the mixture was incubated for between 1 to 4 hours depending on the crosslinker concentration. The MeHA and the crosslinker were mixed to create gels with varying thiol:HA repeating unit ratios, from 10 % to 90% thiol to HA ratio .

6.2.4 Measurement of the effective elastic moduli of the hydrogels by AFM .

The Nanowizard®3 Nanoscience (JPK) AFM and the JPKSPM Data processing software have been used to calculate the effective elastic

moduli of the hydrogels by measuring force spectroscopy curves. Spherical polystyrene beads of 5µm of diameter were attached to a MLCT-0 (BRUKER) cantilever whose elastic constant was calculated for each batch of measurements. As many as 20 force spectroscopy curves were obtained for each hydrogel over a 25µm^2 area. The effective elastic moduli of the hydrogels were calculated following the Hertz model for spherical tips, as previously described in chapter 4. Figure 6.1 shows two examples of force-displacement curves obtained on HA samples with 10% and 50% thiol. The effective elastic modulus is obtained from the approaching segment of the curve (extend on the figure).

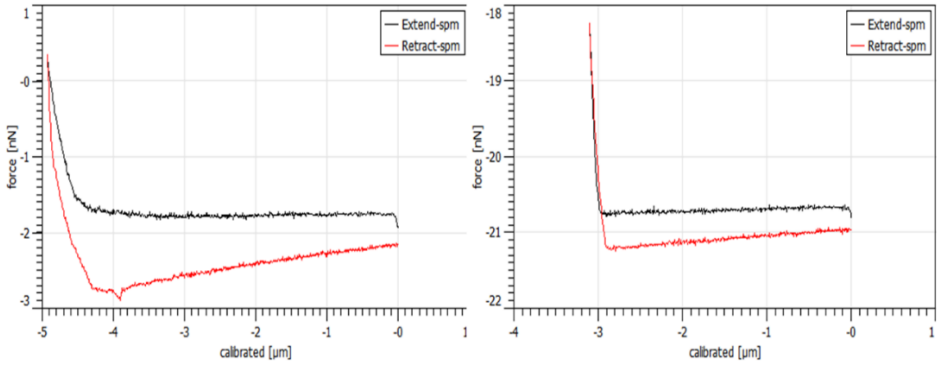

Figure 6.1 Example of the difference between an indentation in a 10% thiol to HA (left) and a 50% thiol to HA (right) MeHA hydrogel.

6.3 DESIGN OF A ROTATORY PLATFORM TO ENCAPSULATE THE CELLS IN A 3D ENVIRONMENT INSIDE THE MEHA HYDROGELS

Once the hydrogels were successfully synthesized the next goal to achieve was how to encapsulate the cells, individually, with enough space between them to avoid cell-cell interactions and spatially well distributed.

6.3.1 Cover glasses treatment

14mm glass bottom petri dishes (Mattek) were used to hold the hydrogel. The cover glasses were previously treated to improve the adherence of the hydrogels to the glass. A solution of 100μl of APTS, (440140 Aldrich) and 100 μl of acetic acid in 500 ml of deionized water was applied to the surface of the cover glasses for 30 minutes. Then, the cover glasses were rinsed 3 times during 5 minutes in deionized water to eliminate any leftover of the solution that could be potentially dangerous for the cell viability.

6.3.2 Single cell encapsulation in MeHA hydrogels

Since the hydrogel gelation took between 1 and 4 hours depending on the amount of crosslinker and the polymer solution, mixing a small number of cells with the solution prior to gelation and waiting until gelation only became in cell sedimentation at the bottom of the hydrogels. To avoid

that sedimentation a set-up was designed so the cells would be always surrounded by hydrogel and to avoid their contact to the glass bottom were the hydrogels were seeded.

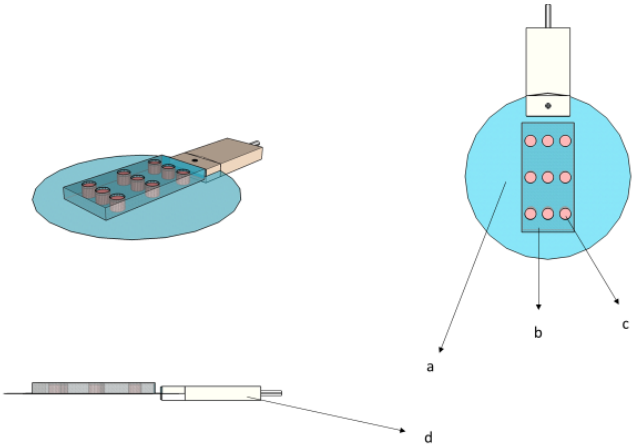

Figure 6.2 Set-up for the 3D encapsulation of the cells inside the MeHA hydrogels. a) Borosilicate glass-bottom petri. b) PDMS cast with wells to fill with the MeHA hydrogels+cells. c)MeHA hydrogels+cells. d) 3D printed clamp to attach the glass-bottom to a rotatory engine.

A 4-piece rotatory set-up was designed to avoid these sedimentation problems (Figure 6.2). In order to study the Cell-ECM interactions, cells were added in a concentration of 50 cells/µl to the hydrogel mixture prior to gelation, right after adding the crosslinker. The mixture of hydrogel+cells was then injected into a PDMS hollow cast as shown in Figure 6.2. The cast was placed on the surface of a previously plasma bonded 14mm glass bottom petri dish creating an irreversible bonding between them. The glass was then treated with the APTS solution to enhance the bonding between the hydrogel and the glass. The 2mm deep

holes of the PDMS cast were filled with 20ul of the pregelated hydrogel+cells mixture. The whole petri dish was then attached to a rotatory motor using a 3D printed plastic clamp. The whole device was then put inside an incubator at 37°C and 5% CO_2 until the gelation of the hydrogels occurred. To avoid the sedimentation of the cells at the bottom of the mold, since the purpose of this hydrogel platform is to study 3D cell behavior the motor rotated at 2 revolutions per minute during the gelation process. After gelation, the set-up (Glass bottom dish + cells) is submerged in fresh cell culture media for at least 24 hours before performing any assay.

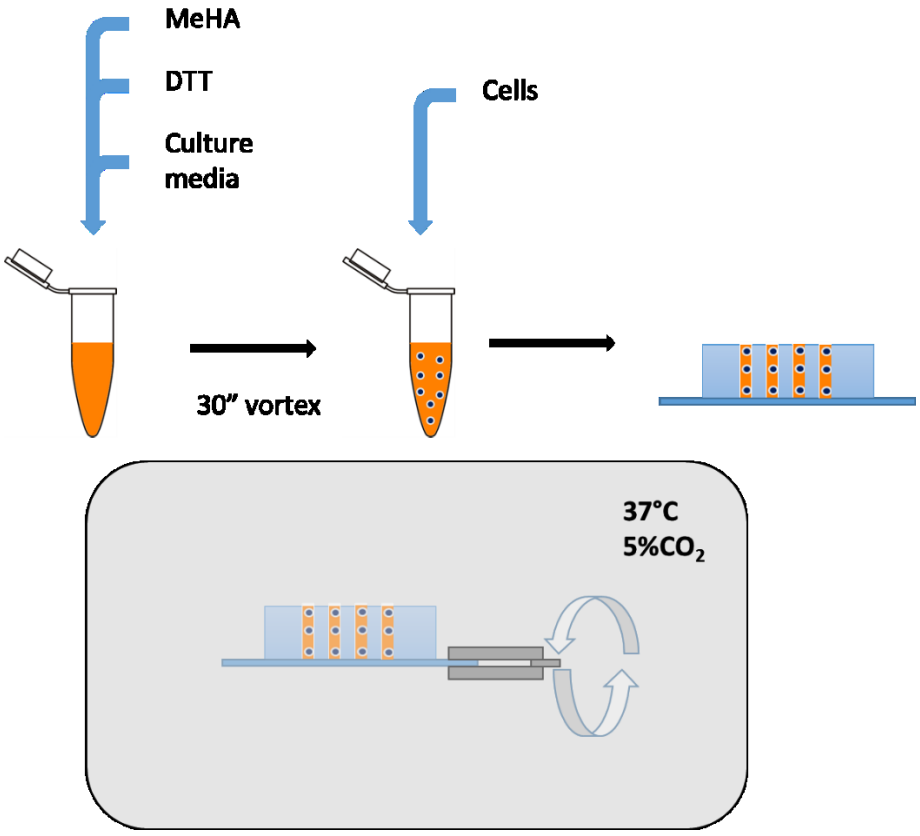

Figure 6.3 Scheme of the 3D cell encapsulation process: from the hydrogel synthesis to the final 3D cell encapsulation in biological conditions.

6.3.3 Cellular viability and medium diffusion in the hydrogels

To check the viability of the cells after their encapsulation non-fluorescent Calcein-AM (Sigma) was used. Calcein-AM is a non-fluorescent cell permeable derivative of calcein that becomes fluorescent upon hydrolysis within the cytosol. Calcein-AM is used as a cell viability stain and as a neutral substrate for multidrug (MDR) efflux

transporters. Diluted in culture media different ratios were tried (inside the working range of the manufacturer). The pictures were taken with a transmission Nikon Eclipse Ti microscope, with a high-resolution monochrome Hamamatsu camera and a specific stage which allowed the control of temperature and environmental conditions.

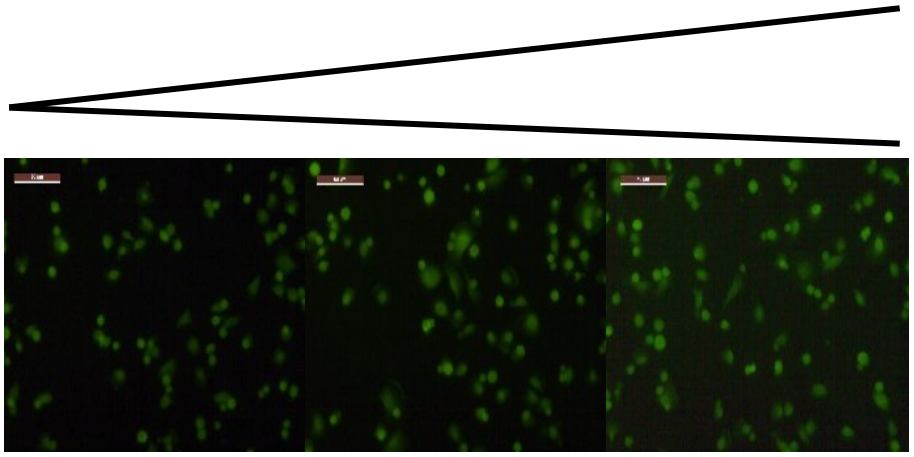

Figure 6.4 DMEM F12 + Calcein. Left 1 μM, Mid 5 μM, Right 10 μM.

A 1μM culture media with Calcein-AM was added 24 hours after the hydrogels had gelated and waited until the cells showed fluorescence. 1 μM was chosen since noise significantly increased when using higher concentrations.

6.3.4 Cell lines used during the assays.

The cells used for this research were A549, Adenocarcinomic human alveolar basal epithelial cells and H1299, human non-small cell lung carcinoma cell line derived from the lymph node. Cells were cultured in RPMI culture media (10% FBS and 1% Penicilin-Streptomicin) on 75 cm^2 flasks. Two cell passages at 80% confluence were made before the

assays were made. A cell concentration of 50 cells/µl in a 20µl hydrogel was used for the assays.

6.3.5 Single cell migration inside the MeHA hydrogels.

Migration assays were performed 24 hours after the hydrogels were soaked in culture media to avoid that any kind of swelling effect could affect the measurements. After 24 hours, images were taken at 10x for 41 hours every 15 minutes at the same focal plane.

6.3.1 Microscopy

The pictures were taken with a transmission Nikon Eclipse Ti microscope, with a high-resolution monochrome Hamamatsu camera and position locking automatic stage built into a chamber which allowed the control of temperature and environmental conditions.

6.4 RESULTS

6.4.1 Measured stiffness of the MeHA hydrogels based on their DTT content

Elastic moduli of the hydrogels were measured to ensure that the hydrogel platform can reach the stiffness range required to mimic the mechanical properties of the targeted ECM. Figure 6.5 shows the effective elastic moduli of the measured hydrogels with different DTT consumption. We observed that the elastic moduli ranged from 238 Pa for a 10% DTT consumption to 18,995 Pa in hydrogels with a 50% DTT consumption. These results cover the physiological range of tissues like brain (<1 kPa) to musculoskeletal tissue (~12 kPa). Higher stiffnessess

have been achieved before for higher MeHA concentrations in the hydrogels [25].

DTT%	Effective Elastic Modulus (Pa)	Standard Deviation
10	238.3	92.4
20	2070.5	152.02
30	6834.5	1989.1
40	7300.0	5232.6
50	19280.0	4115.3
60	7781.5	2571.7
70	8407.5	2549.1
80	5741.5	3670.2
90	4442.5	3708.8

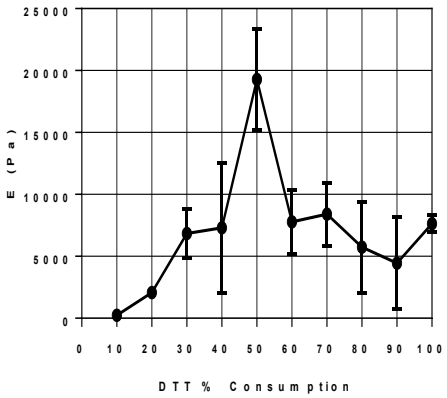

Figure 6.5 Effective Elastic Modulus (Pascals) of the Methacrilated Hyaluronic Acid Hydrogels

.

The effect that explains the increase in the stiffness of the hydrogels when approaching the 50% of DTT consumption is explained in Figure 6.6. After 50% of DTT consumption, all the methacrylate groups of the MeHA have been linked to a thiol molecule of the DTT, 1 DTT links 2 MeHA molecules so all the DTT's thiol groups have been linked. For higher DTT consumption, some of the thiol groups of the DTT will not be able to link due to saturation of the methacrylate groups, this can lead to free thiol groups of the DTT that are not crosslinking the MeHA and therefore lowering the elastic modulus of the gel. In brief, when the 50% of DTT consumption is achieved all the methacrylate groups of the system are saturated with the DTT in a 2 methacrylate groups to 1 DTT molecule ratio. When ratio is higher than 2:1 some of the ends of the DTT may not link the

methacrylate groups together, resulting in a weaker crosslinking and a lower stiffness of the hydrogel.

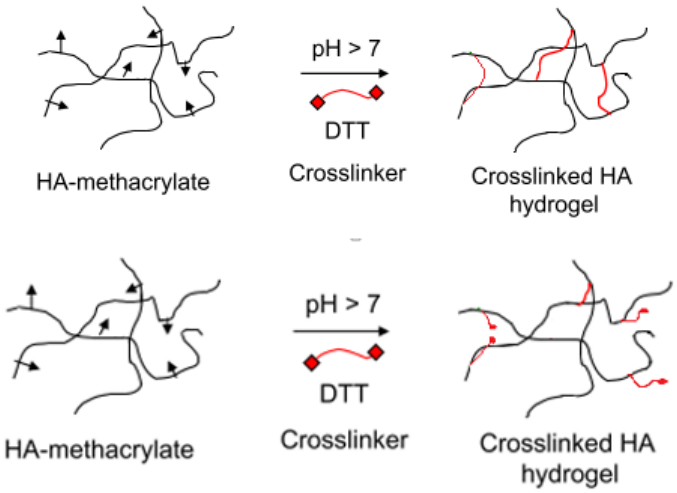

Figure 6.6 Scheme of the effect of the DTT saturation over the 50% consumption. Top image represents the 50% consumption where al the free methacrylate sites are crosslinked. Bottom shows an over 50% consumption of the DTT leaving non crosslinked methacrylate sites.

6.4.2 Single cell 3D encapsulation and viability assay

A density of 50 cells/µl was seeded to avoid cell-cell interaction. 3D cell distribution is the main goal of a hydrogel based platform for the study of the 3D cell-ECM interactions. To check that cells were all distributed in 3D, images at different focal planes were taken. Cells were found in

different focal planes at different heights. confirming the 3D distribution of the cells within the hydrogel.

Figure 6.7, shows bright field and fluorescence images of cells encapsulated in 600, 2000 and 6000 Pa MeHA. Some of the cells are focused while other remain out of focus, this is thanks to the capacity of the rotatory platform to maintain the cells distributed through the gel. Since the time until fully gelation of the cells can go from 1 to 4 hours, cells tend to sediment at the bottom of the gel. When this happens, cells form adhesions to the glass instead of migrating through the hydrogels which has to be avoided when studying 3D ECM-interactions since cells are not likely to migrate upwards after being seeded on glass due to durotactic effects. [26], [27].

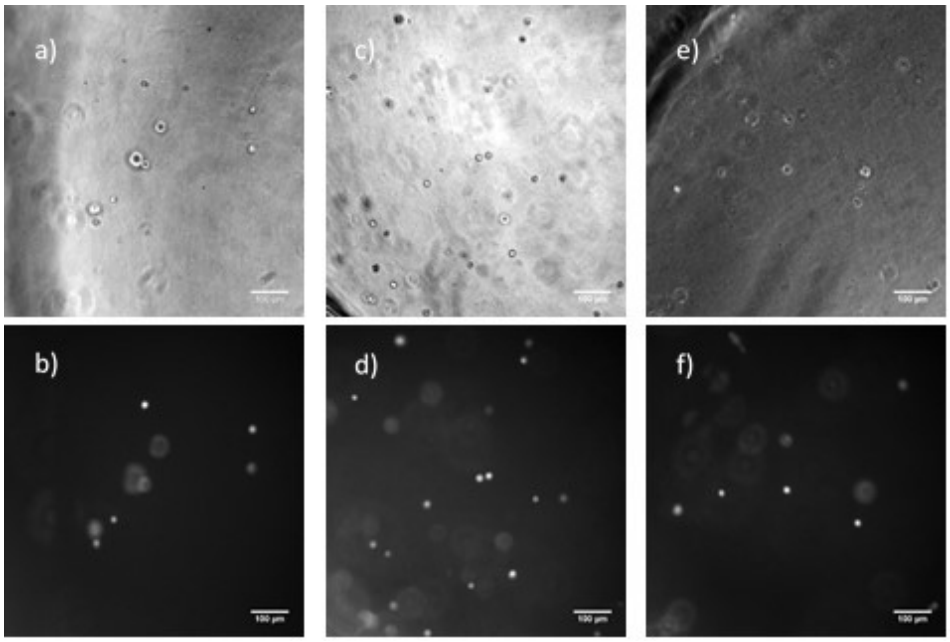

Figure 6.7 Cell viability assay using Calcein-AM. Cells encapsulated in 600 Pa MeHA hydrogels a) Bright Field b) Fluorescence. 2000 Pa MeHA hydrogels c) Bright Field d) Fluorescence and 6000 Pa MeHA hydrogels.

The viability of the cells after 24 hours of the encapsulation inside the gels was investigated by fluorescence microscopy using Calcein-AM. Culture media is changed to hydrogels that were submerged during 24 hours in fresh culture media after gelation for a 1μM Calcein-AM in fresh culture media solution. After 20 minutes observing the cells at 37°C and 5%CO_2. cells started to show green fluorescence. Since the fluorescence is a consequence of the intracellular sterases removing the acetomethoxy group from the Calcein and dead cells lack active esterases, only the live cells are labeled. An 83 ± 7% of the cells showed fluorescence 24 hours after gelation of the hydrogels when exposed to a Calcein-AM viability assay Figure 6.7,

6.4.3 Cell migration inside the 3D migration platform

6.4.3.1 *A549 cell migration*

The A549 cells were seeded into the hydrogels for 24 hours. Once that time was elapsed migration was observed for 41 more hours. Only 2D migration was characterized inside the lower stiffness hydrogels (10% DTT) but not in 20% DTT and 30% DTT hydrogels due to the higher stiffnesses of the hydrogels. 3D migration was observed but not quantified. Figure 6.8 shows a cell at T=16h that leaves the focal plane (red circled) and a cell that enters the focal plane at t=21h not any

tendency was observed to confirm that cells followed a mainly upward or downward direction, so we can assume that the cells were far enough from the glass bottom to be affected by the durotactic effects [26], [27].

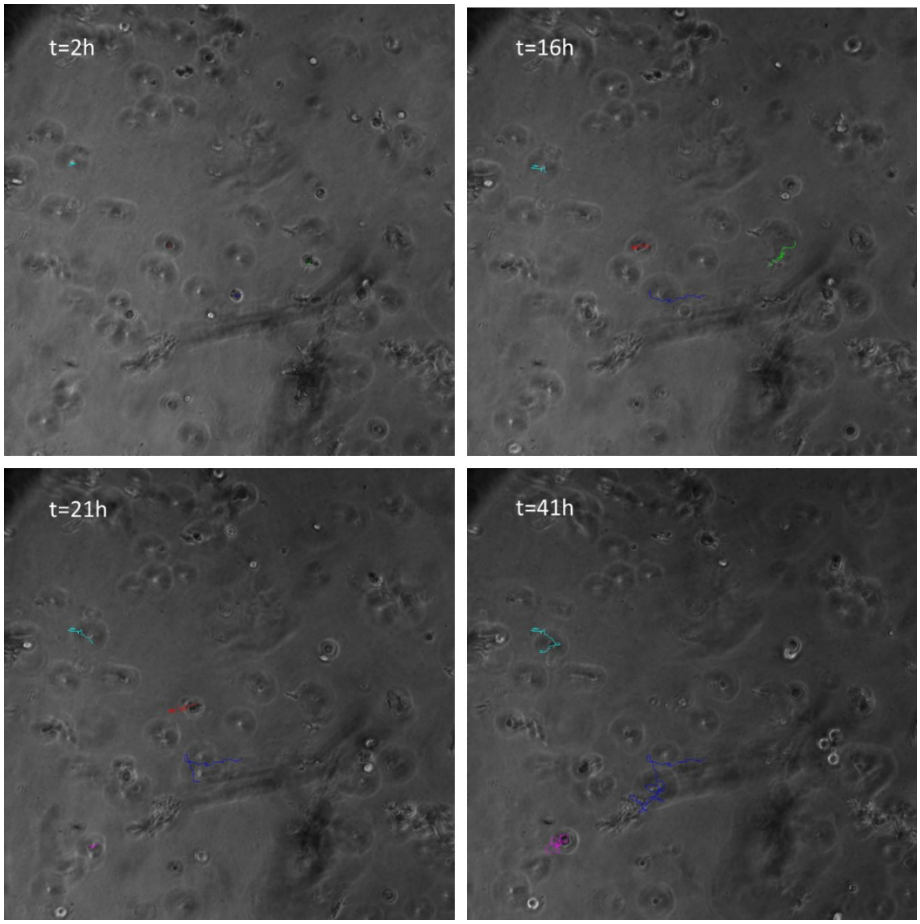

Figure 6.8 3D A549 cell migration assay at t=2h, 16h, 21h and 41h. The colored lines represent the path followed by the cells while they were focused on the focal plane.

Single plane cell-migration was quantified for 15 cells that entered the focal plane during the 41 hours of the assay. As mentioned before, some of the cells migrated out of the focal plane so just the migration during

the time they were on focus was quantified. As can be seen in Figure 6.9, the 2D migration of the cells that migrated on the focal plane shows no directionality. The A549 cells migrated a mean maximum distance from the start position of 90 ± 45.51 µm with a mean path of 370 ± 148.75 µm and a mean speed of 12.01 ± 2.51 µm/h. The maximum migration distance of a cell from the start position was 576 µm and the further a cell went from the start position was 149 µm.

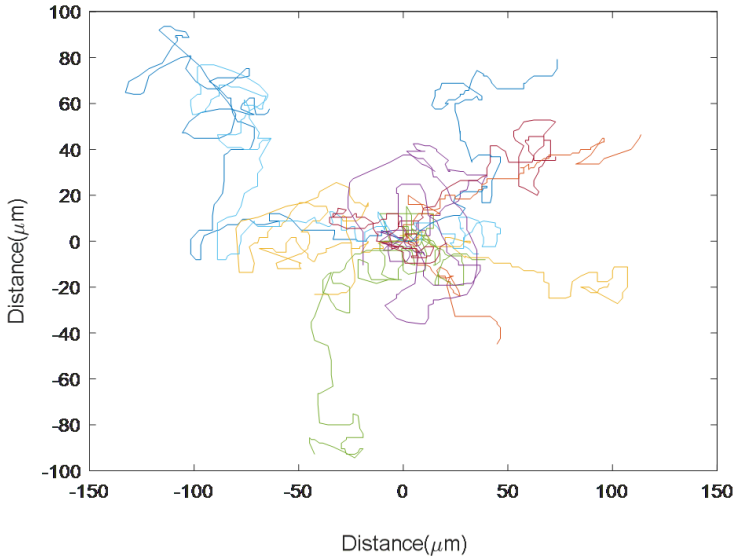

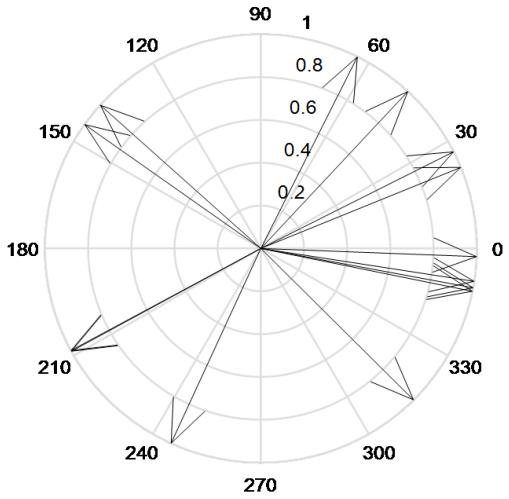

Figure 6.9 Top, path followed by each A549 cell that entered the focal plane. All of them starting in a common point. Bottom, direction of the paths of the cells, normalized.

As we can see on Figure 6.9, cells did not show any predominant migration direction during the 41 hours of the assay. This confirms that the cells were seeded far enough not to feel the glass at the bottom of

the gels and the PDMS walls that could have had created a durotactic effect leading to a predominant migration direction for the cells towards the stiffer parts of the platform.

6.4.3.2 *H1299 cell migration*

The assay was repeated with H1299 human non-small cell lung carcinoma derived from the lymph node. The assay was proposed to study the migration of H1299 cell line using the 3D single cell seeding MeHA hydrogel platform. Cell migration was observed during a 16 hour assay, 24 hours after the cells were seeded in the hydrogels. As in the A549 cell line, 3D migration was observed but not quantified, just the 2D migration of the cells in the focused plane was quantified. The cells were seeded in 10%DTT, 20%DTT and 30% DTT MeHA hydrogels. Migration was observed for the three hydrogels. As for the A549 cell line, a clear trend was not observed to confirm that cells followed a mainly upward or downward direction. So we can assume that the cells were far enough from the glass bottom to be affected by the durotactic effects [26], [27].

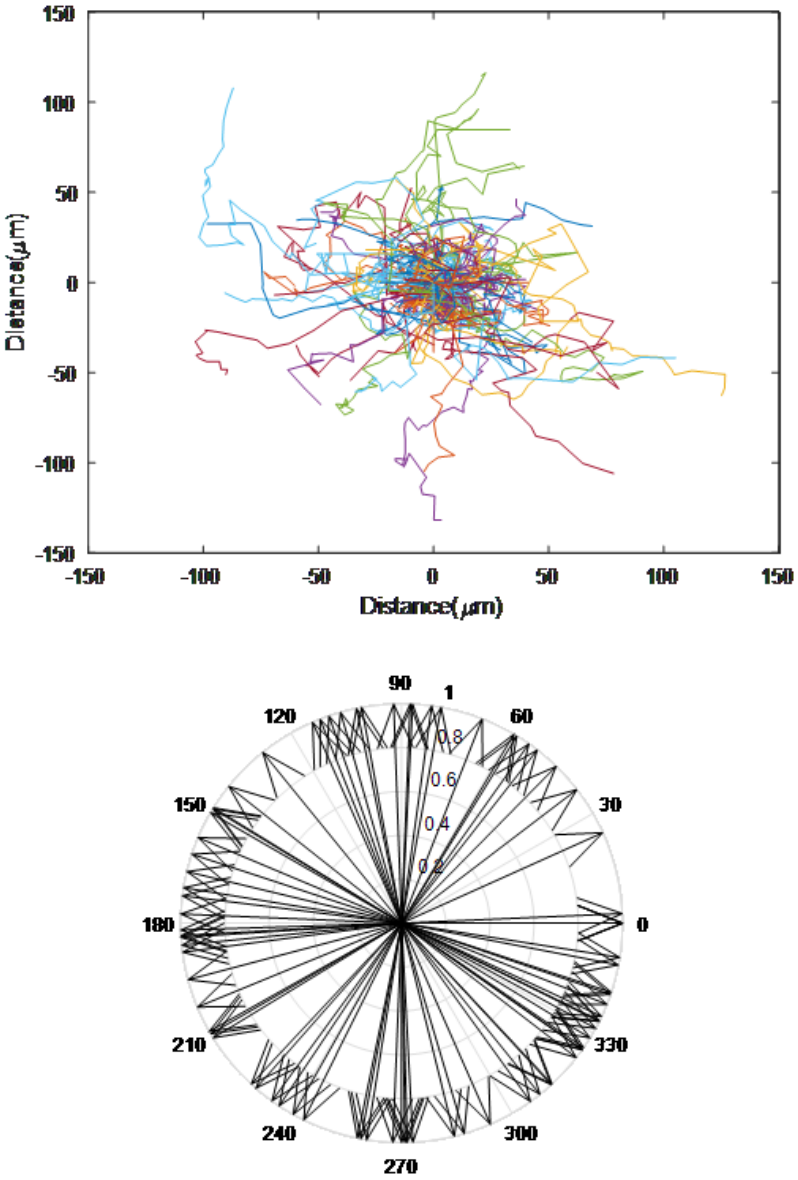

Figure 6.10 Top, path followed by each H1299 cell that entered the focal plane. All of them starting in a common point. Bottom, direction of the paths of the cells, normalized.

The assay was repeated three times in three different stiffness of 10%DTT (~240 Pa), 20%DTT(~2000 Pa) and 30%DTT(~7000 Pa) that are reported on Figure 6.5. Up to 80 cells were measured for each hydrogel. The goal of this assay was to quantify the migration speed and the total path traveled by each cell in the three different stiffnesses.

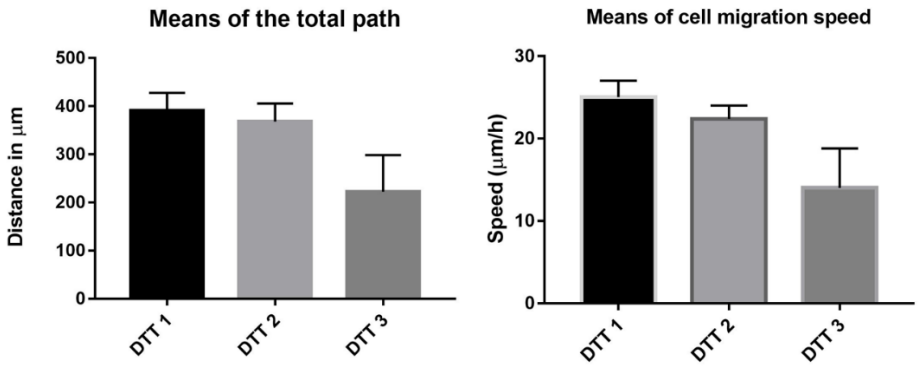

Figure 6.11 Left, Means of the total path traveled by the cells in each DTT consumption rate, DTT1=240 Pa , DTT2= 2000 Pa , DTT3= 7000 Pa. Right, Means of cell migration speed in the same conditions.

As can be seen in Figure 6.10, the 2D migration of the cells that migrated on the focal plane shows no directionality. The cells H1299 in 10%DTT hydrogels migrated a mean path of 391.1 ± 36.63 µm at a mean speed of 25.03 ± 2.03 µm/h. Moreover, the speed and mean of the total path of the cells seeded in 20% DTT hydrogels decreased to a mean path of 380 ± 37.46 µm and a mean speed of 22.38 ± 2.29 µm/h. The cells H1299 migration in 30%DTT hydrogels dropped with a migrated mean path of 222.4 ± 76.19 µm and a mean speed of 14.01 ± 4.36 µm/h. These results are plotted in Figure 6.11.

The H1299 cell line in 10% DTT hydrogels migrated faster and further than A549 cell line, which correlates with the data shown by [28]. Also, H1299 cell line was able to migrate towards all three hydrogel stiffness which

could be due to their higher migratory capabilities as can be observed in Figure 6.12.

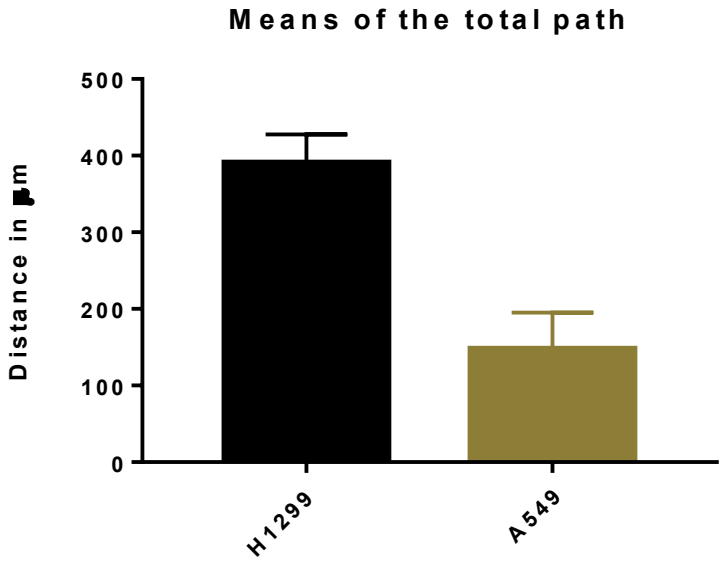

Figure 6.12 Comparison between the means of the total path migrated by A549 and H1299 cell lines in 200 Pa MeHA hydrogels.

6.5 CONCLUSIONS

A functional platform for the study of single cell-ECM interactions based on Methacrylate Hyaluronic acid hydrogels has been developed. The hyaluronic acid hydrogels seem to be a great option to mimic the physiological ECM due to their mechanical tunability. In this work, the elastic moduli of the hydrogels ranged from a hundred of Pa to 20 kPa, which comprehends the stiffness values of the target tissue ECM where A549 and H1299 cell lines can be found: lung tissue.

A spatial distribution of the cells was obtained thanks to the use of a rotatory platform during the gelation of the gels preventing the gels from

getting sedimented at the bottom of the gel prior to complete gelation. The proposed setup and protocol worked perfectly according to the obtained images of the different focal planes along the Z axis with cells on focus on different planes. An 83±7% of the cells showed fluorescence 24 hours after gelation of the hydrogels when exposed to a Calcein-AM viability assay, which proves that cells survive in this environment.

A preliminary assay of cell migration was carried out using A549 cell line. Random migration was observed in 2D which assures that the platform works, and the cells are not moving toward any preferential direction due to durotactic effects of the different parts of the platform such ash de PDMS walls or the glass at the bottom of the gels. Also, 3D migration was observed by watching cells coming in and out of focal plane during the 41 hours the assay lasted.

A second assay of cell migration was carried out using H1299 cell line. Random migration was also observed in 2D, which assures and complements the previous data obtained with A549 cell line. H1299 cell line did not show any preferential migratory direction due to durotactic effects of the surrounding PDMS and glass bottom of the platform. H1299 cell line showed also a higher motility inside the hydrogels being able to migrate at higher stiffness than A549 cell line. In fact, no migration is observed for A549 within a microenvironment with a stiffness higher than 2kPa.

Overall, a functional platform with tunable stiffness for the study of 3D single cell-ECM interactions based on Methacrylate Hyaluronic Acid hydrogels that permits 3D seeding avoiding problems caused by durotaxis has been created.

6.6 BIBLIOGRAPHY

[1] S. V. Plotnikov, A. M. Pasapera, B. Sabass, and C. M. Waterman, "Force fluctuations within focal adhesions mediate ECM-rigidity sensing to guide directed cell migration," *Cell*, vol. 151, no. 7, pp. 1513–1527, 2012.

[2] B. D. Hoffman, C. Grashoff, and M. A. Schwartz, "Dynamic molecular processes mediate cellular mechanotransduction," *Nature*, vol. 475, no. 7356, pp. 316–323, 2011.

[3] D. T. Tambe *et al.*, "Collective cell guidance by cooperative intercellular forces," *Nat. Mater.*, vol. 10, no. 6, pp. 469–475, 2011.

[4] a. Katsumi, "Integrins in Mechanotransduction," *J. Biol. Chem.*, vol. 279, no. 13, pp. 12001–12004, 2003.

[5] A. D. Bershadsky, N. Q. Balaban, and B. Geiger, "Adhesion-Dependent Cell Mechanosensitivity," *Annu. Rev. Cell Dev. Biol.*, vol. 19, no. 1, pp. 677–695, 2003.

[6] S. Linder and C. Wiesner, "Feel the force: Podosomes in mechanosensing," *Exp. Cell Res.*, vol. 343, no. 1, pp. 67–72, 2016.

[7] A. Athirasala, N. Hirsch, and A. Buxboim, "Nuclear mechanotransduction: sensing the force from within," *Curr. Opin. Cell Biol.*, vol. 46, pp. 119–127, 2017.

[8] G. Bao and S. Suresh, "Cell and molecular mechanics of biological materials," pp. 715–725, 2003.

[9] A. J. Engler, S. Sen, H. L. Sweeney, and D. E. Discher, "Matrix Elasticity Directs Stem Cell Lineage Specification," *Cell*, vol. 126,

no. 4, pp. 677–689, 2006.

[10] J. S. Park *et al.*, "The effect of matrix stiffness on the differentiation of mesenchymal stem cells in response to TGF-??," *Biomaterials*, vol. 32, no. 16, pp. 3921–3930, 2011.

[11] I. Levental, P. C. Georges, and P. A. Janmey, "Soft biological materials and their impact on cell function," *Soft Matter*, vol. 3, no. 3, pp. 299–306, 2007.

[12] H. Follet, G. Boivin, C. Rumelhart, and P. J. Meunier, "The degree of mineralization is a determinant of bone strength: A study on human calcanei," *Bone*, vol. 34, no. 5, pp. 783–789, 2004.

[13] Y.-R. Zhang, W. Du, X.-D. Zhou, and H.-Y. Yu, "Review of research on the mechanical properties of the human tooth," *Int. J. Oral Sci.*, vol. 6, no. 2, pp. 61–69, 2014.

[14] V. R. Sherman, W. Yang, and M. A. Meyers, "The materials science of collagen," *J. Mech. Behav. Biomed. Mater.*, vol. 52, pp. 22–50, 2015.

[15] B. D. Walters and J. P. Stegemann, "Strategies for directing the structure and function of three-dimensional collagen biomaterials across length scales," *Acta Biomater.*, vol. 10, no. 4, pp. 1488–1501, 2014.

[16] A. D. Doyle, N. Carvajal, A. Jin, K. Matsumoto, and K. M. Yamada, "Local 3D matrix microenvironment regulates cell migration through spatiotemporal dynamics of contractility-dependent adhesions," *Nat. Commun.*, vol. 6, p. 8720, 2015.

[17] C. Echalier *et al.*, "Sol–gel synthesis of collagen-inspired peptide

hydrogel," *Mater. Today*, vol. 20, no. 2, pp. 59–66, 2017.

[18] A. Ray, Z. M. Slama, R. K. Morford, S. A. Madden, and P. P. Provenzano, "Enhanced Directional Migration of Cancer Stem Cells in 3D Aligned Collagen Matrices," *Biophys. J.*, vol. 112, no. 5, pp. 1023–1036, 2017.

[19] A. D. Augst, H. J. Kong, and D. J. Mooney, "Alginate hydrogels as biomaterials," *Macromol. Biosci.*, vol. 6, no. 8, pp. 623–633, 2006.

[20] J. a. Rowley, G. Madlambayan, and D. J. Mooney, "Alginate hydrogels as synthetic extracellular matrix materials," *Biomaterials*, vol. 20, no. 1, pp. 45–53, 1999.

[21] J. R. Fraser, T. C. Laurent, and U. B. Laurent, "Hyaluronan: its nature, distribution, functions and turnover.," *J. Intern. Med.*, vol. 242, pp. 27–33, 1997.

[22] Y. Tan *et al.*, "Matrix softness regulates plasticity of tumour-repopulating cells via H3K9 demethylation and Sox2 expression," *Nat. Commun.*, vol. 5, pp. 1–12, 2014.

[23] D. Hanahan and R. A. Weinberg, "The hallmarks of cancer.," *Cell*, vol. 100, no. 1, pp. 57–70, 2000.

[24] B. Ananthanarayanan, Y. Kim, and S. Kumar, "Elucidating the mechanobiology of malignant brain tumors using a brain matrix-mimetic hyaluronic acid hydrogel platform," *Biomaterials*, vol. 32, no. 31, pp. 7913–7923, 2011.

[25] B. Ananthanarayanan, "Elucidating the mechanobiology of malignant brain tumors using a brain matrix-mimetic hyaluronic acid hydrogel platform," *Changes*, vol. 29, no. 6, pp. 997–1003, 2012.

[26] C. M. Lo, H. B. Wang, M. Dembo, and Y. L. Wang, "Cell movement is guided by the rigidity of the substrate," *Biophys. J.*, vol. 79, no. 1, pp. 144–152, 2000.

[27] P. Roca-Cusachs, R. Sunyer, and X. Trepat, "Mechanical guidance of cell migration: Lessons from chemotaxis," *Curr. Opin. Cell Biol.*, vol. 25, no. 5, pp. 543–549, 2013.

[28] Q. Cao *et al.*, "MicroRNA-7 inhibits cell proliferation, migration and invasion in human non-small cell lung cancer cells by targeting FAK through ERK/MAPK signaling pathway," *Oncotarget*, vol. 7, no. 47, pp. 77468–77481, 2016.

7 CONCLUSIONS

Cancerous and non-cancerous lung ECM samples from 7 patients were obtained, sliced in 7 µm thick slices, decellularized and their structural proteins stained following a primary/secondary immunofluorescence protocol. Then 400 AFM indentations of 500 nm were performed in a 100*100µm area while each protein map was imaged using the epifluorescence microscope. The mechanical properties of the cancer lung ECM showed a 2.5 fold increase of the effective Young's modulus compared to the healthy one. The effective Young's modulus of the non-cancerous ECM is of 6.33 ±1.13 kPa whereas the cancerous ECM showed a mean value of 15.65±4.04 kPa. When both samples from a same patient were merged together, they showed a bimodal distribution.

The composition-mechanical property correlation was studied. For that, the volume fraction of the samples was calculated using two different references, one relative to the maximum intensity of all the samples and the other one relative to the maximum intensity of each sample to minimize experimental variability of the staining procedure. Both methods showed an increment of the collagen I amount between the non-cancerous and cancerous samples with a mean increase of 1.7 folds and 1.5 folds respectively.

The comparison between the measured Young's modulus and the calculated volume fraction of the collagen I showed a positive correlation on each sample. The mean calculated volume fraction and the mean measured Young's modulus for each sample showed a correlation of R^2=

0.608 between all the measured samples. This suggests that an increase in the collagen I volume fraction is related to the ECM stiffening.

Then, the microstructure-mechanical property relationship was studied. A model based on Eshelby´s inclusion problem was used to predict the mechanical behavior of the lung cancerous and non-cancerous ECM. For a 3D distribution of the collagen I fibers the model estimated the E of the non-cancerous and cancerous lung ECM with a mean absolute error of 25.08% and 32.74% respectively, fitting a linear regression with R^2=0.6155. In this case, the Young's modulus of the collagen I fibers was estimated from the elastic modulus measured at the 10 locations with the highest volume fraction of collagen I in the samples using the model. The elastic modulus of collagen I was calculated separately for non-cancerous and cancerous samples, obtaining a value of 390 kPa and 1050 kPa for respectively. These values of elastic modulus for collagen I are much lower than the values reported in literature (100 MPa).

The prediction improved when the fibers were distributed in a 2D plane. The E of the collagen I fibers for the 2D fiber distribution was physiologically coherent, 100MPa, coherent with the range reported in literature. The elastic modulus of the matrix was tuned in order to minimize the absolute average error between the measured and predicted elastic modulus of the ECM. The effect of the crosslinking and other stiffening mechanisms which were not measured, are reflected in the E of the model matrix, being the matrix of the cancerous ECM (Ematrix = 0.12 kPa) higher than the non-cancerous ECM (Ematrix = 0.05 kPa). The prediction showed a mean absolute error of 14.48% for the non-cancerous lung ECM and of 11.15% for the cancerous ECM, with a correlation of R^2=0.944 when a linear regression is fitted for the

predicted versus measured stiffness. The volume fraction of the collagen I was calculated with the maximum intensity value of each sample as reference. The measured aspect ratio, and direction of the bundles of fibers also increased the correlation obtained by the model estimation.

To study the implications of the stiffness in 3D, a functional platform for the study of single cell-ECM interactions based on Methacrylate Hyaluronic acid hydrogels was developed. The hyaluronic acid hydrogels seem to be a great option to mimic the physiological ECM due to their mechanical tunability. In this work the elastic moduli of the hydrogels ranged from 238 Pa to 20 kPa, which comprehends the stiffness values of the target tissue ECM. Proof of concept experiments were made with A549 and H1299 cell lines. The hydrogels showed suitable conditions for the study of cell viability and motility. Overall, a functional platform with tunable stiffness for the study of 3D single cell-ECM interactions was developed based on Methacrylate Hyaluronic Acid hydrogels. ,

GLOSSARY OF TERMS

a=contact radius

AFM: Atomic Force Microscopy

AI= Strain concentration tensor for dilute systems.

ANOVA= one-way analysis of variance

APC: Antigen Presenting Cells

ATP: Adenosine Tri phosphate

Aα= concentration tensors

BSA; Bovine Serum Albumin

Cc= effective stiffness of the composite

CI= stiffnes of the inclusion

CM= stiffness of the matrix

COL: Collagen

COPD: Chronic obstructive pulmonary disease

DTT=DL-dithiothreitiol

E= elastic modulus, Young's modulus

ECM: Extracellular Matrix

EColl= Collagen I stiffness

EECM= predicted ECM stifness

EF: Elastic Fiber

Ematrix= matrix stiffness

F= Force

fA=volume fraction of phases of inclusions

FACIT: Fibril associated collagens

FBS: Fetal Bovine Serum

fM=volume fraction of matrix

GAG; Glycosaminoglycan

GPP: Glycine-Proline-Hydroxyproline

HA: Hyaluronic Acid

HA= Hyaluronic Acid

I= unit tensor of fourth order

IColl= intensity of a pixel of collagen I

ImaxColl= Maximum intensity measured for collagen I

ImaxrColl= maximum measured intensity on each sample

IPF: Idiopathic pulmonary fibrosis

k=spring constant

LOX= Lysil Oxidase

MeHA= Methacrylate Hyaluronic Acid

MMP: Matrix metalloproteinase

NC: Non Collagen

NpECM= Number of pixels with any of the three proteins

PBS: Phosphate Buffer Saline

PDMS=Poli Dimethyl Sulfate

R= radius of the tipo

RGD: Arginine-Glycine-Aspartic Acid sequence

RHAMM: Receptor for Hyaluronan-mediated motility

S= Eshelby's S tensor

SLRP: Small Leucine Rich Proteoglycan

TGF-β; Transforming growth factor beta

v= Poisson's coefficient

Vf= Volume fraction

x= cantilever deflection

z= height of the head of the AFM

δ= indented distance

ε^*= transformation strain

εc= constrained strain

σ= effective stiffness